Title

Improving the Toughness of Ultrahigh Strength Steel

Author

Sato, Koji

Publication Date

2002-08-01

LBNL-51353

ERNEST ORLANDO LAWRENCE
BERKELEY NATIONAL LABORATORY

Improving the Toughness of Ultrahigh Strength Steel

Koji Sato

Materials Sciences Division
Center for Advanced Materials

August 2002

Ph.D. Thesis

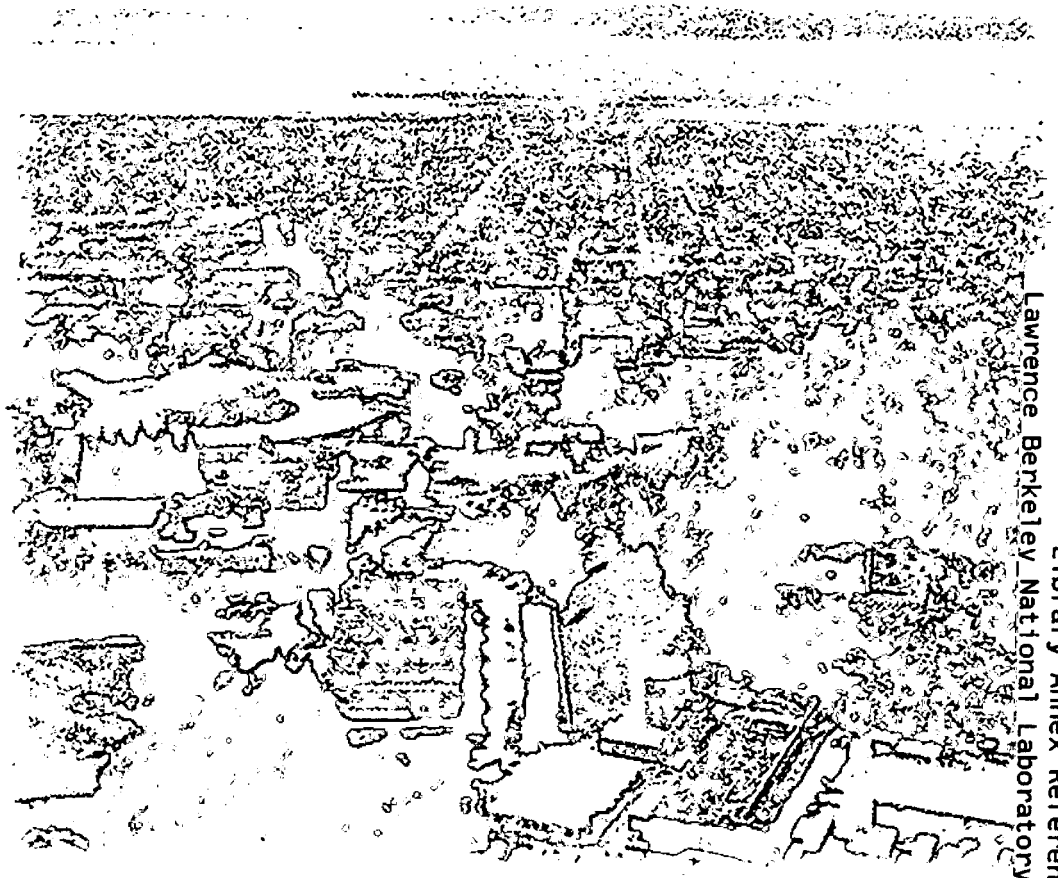

DISCLAIMER

LBNL-51353

Improving the Toughness of Ultrahigh Strength Steel

Koji Sato
Ph.D. Thesis

Department of Engineering
University of California, Berkeley

and

Materials Sciences Division
Ernest Orlando Lawrence Berkeley National Laboratory
University of California
Berkeley, CA 94720

August 2002

This work was supported by the Director, Office of Science, Office of Basic Energy Sciences, Materials Sciences Division, of the U.S. Department of Energy under Contract No. DE-AC03-76SF00098, and also funded by a grant from the Naval Air Warfare Center.

Improving the Toughness of Ultrahigh Strength Steel

by

Koji Sato

B.E. (Kyoto University) 1984
M.ENG. (Kyoto University) 1986

A dissertation submitted in partial satisfaction of the

requirements for the degree of

Doctor of Philosophy

in

Engineering-Materials Science and Mineral Engineering

in the

GRADUATE DIVISION

of the

UNIVERSITY OF CALIFORNIA, BERKELEY

Committee in charge:

Professor John W. Morris, Jr., Chair
Professor Gareth Thomas
Professor David Dornfeld

Fall 2002

Improving the Toughness of Ultrahigh Strength Steel

by

Koji Sato

ABSTRACT

Improving the Toughness of Ultrahigh Strength Steel

by

Koji Sato

Doctor of Philosophy in Materials Science and Mineral Engineering

University of California, Berkeley

Professor John W Morris, Jr., Chair

The ideal structural steel combines high strength with high fracture toughness. This dissertation discusses the toughening mechanism of the Fe/Co/Ni/Cr/Mo/C steel, AerMet 100, which has the highest toughness/strength combination among all commercial ultrahigh strength steels. The possibility of improving the toughness of this steel was examined by considering several relevant factors.

Chapter 1 reviews the mechanical properties of ultrahigh strength steels and the physical metallurgy of AerMet 100. It also describes the fracture mechanisms of steel, i.e. ductile microvoid coalescence, brittle transgranular cleavage, and intergranular separation.

Chapter 2 examines the strength-toughness relationship for three heats of AerMet 100. A wide variation of toughness is obtained at the same strength level. The toughness varies despite the fact that all heat fracture in the ductile fracture mode. The difference originates from the inclusion content. Lower inclusion volume fraction and larger inclusion spacing gives rise to a greater void growth factor and subsequently a

higher fracture toughness. The fracture toughness value, J_{Ic}, is proportional to the particle spacing of the large non-metallic inclusions.

Chapter 3 examines the ductile-brittle transition of AerMet 100 and the effect of a higher austenitization temperature, using the Charpy V-notch test. The standard heat treatment condition of AerMet 100 shows a gradual ductile-brittle transition due to its fine effective grain size. Austenitization at higher temperature increases the prior austenite grain size and packet size, leading to a steeper transition at a higher temperature. Both transgranular cleavage and intergranular separation are observed in the brittle fracture mode.

Chapter 4 examines the effect of inclusion content, prior austenite grain size, and the amount of austenite on the strength-toughness relationship. The highest toughness is achieved by low inclusion content, small prior austenite grain size, and a small content of stable austenite. The low inclusion content increases the strain at the fracture. The reduction in prior austenite grain size prevents the fast unstable crack propagation by cleavage. And the stable austenite decreases the strength of the intergranular separation at the prior austenite grain boundary, which provides the stress relief at the crack tip.

To my wife, Kako,

my children, Hayami, Mona and Oji,

and my parents.

TABLE OF CONTENTS

LIST OF FIGURES

LIST OF TABLES

ACKNOWLEDGEMENTS

I am indebted to many people for their support in making this work possible.

I would first like to thank my research advisor, Professor J. W. Morris, Jr. for his patience and guidance throughout the years in Berkeley and Japan. I am also grateful to Prof. G. Thomas and Prof. D. Dornfeld along with Prof. Morris for serving on my thesis committee.

I am grateful for the support provided by the people outside and within our group. I was supported by the scholarship from Hitachi Metals all through my PhD program. I would have not fulfilled my degree without the support from my seniors and colleagues of Hitachi Metals in Japan. Especially, I would like to thank to H. Nakamura, R. Watanabe, T. Okuno, M. Tanii, T. Uehara, T. Ohno, and K. Kirihara. E. Lee of Naval Air Warfare Center provided precious AerMet 100 bars.

Special thanks to Chris Krenn and Peter Skarpelos, from whom I have learned not only scientific knowledge but also about life in the United Sates. They reviewed the draft of this dissertation and gave me questions and suggestions as well as lots of corrections of my English errors. Dr. S. K. Hwang also gave me useful suggestions. I wish to thank Dr. Jin Chan for his guidance with the lab equipment and many discussions about steel. Chip Flor and James Wu helped me for the sample preparation.

It was a great pleasure to work with and learn from Seung Hyuk Kang, Carlos Gonzalez, Dave Mitlin, Ho Geon Song, Choongun Kim, Pamela Kramer, Heidi Reynolds, Carol Tseng, Andy Minor, and Monica Barney.

Most importantly, my warmest gratitude is for my wife, Kako, for her unending support, patience, and encouragement through all the ups and downs of my research and

studies. Cheers from my three children, Hayami, Mona, and Oji, also encouraged me an enormous amount. At last, I also thank my parents for their love throughout my life.

This research was funded by the Director, Office of Science, Office of Basic Energy Science, Materials Science Division of the U.S. Department of Energy, under contract No. DE-AC03-76SF00098, and also funded by the grant from Naval Air Warfare Center.

1. General Introduction

1.1 Motivation

Understanding the mechanical properties–microstructure relationship of ultrahigh strength steel remains a key problem in metallurgy and is the subject of this thesis.

Among several ultrahigh strength steels, the secondary hardening Fe/Ni/Co/Cr/Mo/C alloy, AerMet 100, developed by Carpenter Technology Corporation in the early '90s, has the best combination of toughness and strength. Early experimental measurements in this laboratory revealed a puzzling variation in fracture toughness values among three heats produced by Carpenter. Their tensile strengths were almost the same, but their toughnesses were very different. One was at the bottom of the specification range, another at the level of nominal value, and the last was at an extremely high level. We assumed the difference must be microstructural, and understanding the details could reveal a way to improve the toughness of this ultrahigh strength steel, or even to develop a new steel.

The explanation for the wide range of toughness values, which we discovered during the course of our research, was related to the influence of the inclusion content on the ductile fracture behavior. The extremely high toughness value seen in one heat, maybe the best combination of toughness and strength among all commercially available ultrahigh strength steels, was obtained in the heat with the lowest inclusion content. Although this phenomenon is well known in many high strength steels, no one had

explored it at such high levels of strength and toughness before.

However, controlling inclusion content is not sufficient. Such a good combination of strength and toughness at ambient temperature is only possible with a specific set of heat treatments. These heat treatments should produce well-tailored microstructures that inhibit fracture propagation. Therefore the second task of this thesis was to determine the optimal microstructure and heat treatment required to produce high toughness material.

This thesis aims to develop the understanding of the extraordinary mechanical behavior, especially the toughening mechanism, of this steel and to find the best way of improving its toughness. For clarity it is divided into the following topics:

1) A comparison of the strengthening mechanisms of other ultrahigh strength steels: By understanding the physical and mechanical metallurgy of several ultrahigh strength steels, we can identify some of the ways in which AerMet 100 was tailored to achieve its high performance properties. This will be discussed in next section.

2) A review of the physical metallurgy of AerMet 100 (section 1.3): Much previous microstructural characterization and mechanical property measurement of AerMet 100 has been conducted. This is reviewed and summarized in a schematic TTT diagram.

3) A general review of the ductile and brittle fracture mechanisms in steel: Ferritic steels have a BCC structure and are inherently more brittle than FCC materials,

such as Cu and Al, because they can cleave. Understanding how to suppress the cleavage is vital to developing better properties. If one can suppress the brittle fracture and lower the ductile-brittle transition temperature, one creates room for further strengthening, and may be able to strengthen the steel by adding more or different hardening elements into the steel. This will be reviewed in section 1.4.1, and experimental data on the ductile-brittle transition of AerMet 100 will be shown and discussed in chapter 3.

4) Understanding the microstructural features which relate to each step of ductile fracture process: Since the high impact toughness of AerMet 100 at ambient temperature is achieved by its ductile fracture mode, close analysis of ductile fracture is the key to understanding why such a wide variation of toughness was obtained. What we show is that the inclusion content among these heats was significantly different. This will be reviewed in section 1.4.2 and the experimental results on AerMet 100 will be discussed in chapter 2.

5) Optimizing the heat treatment of AerMet 100: The mechanical behavior of AerMet 100 will be explored by varying the heat treatment conditions, such as austenitizing temperature, skipping the "deep-freeze" step, and adding pre-aging (intercritical tempering). These changes affect microstructural characteristics (such as grain size and amount of austenite), work-hardening behavior, tensile strength and fracture toughness. These experimental results will be shown and discussed in chapter 4.

Finally, chapter 5 shows ideas on how to maximize the combination of strength and

toughness of AerMet 100 and discusses future directions for the design of stronger and tougher ultrahigh strength steels.

1.2 Overview of ultrahigh strength steels[1] *

Since ultrahigh strength steels are relatively expensive, their uses are ordinarily restricted to such applications as aircraft parts and some very heavy duty parts where their relatively high cost can be justified. Landing gears, arresting hooks, fasteners, jet engine shafts, and ballistic-tolerant components are representative uses for aircraft, and high-strength bolts, automotive drive shafts and bicycle frames are some typical uses for non-aircraft heavy duty parts.

Ultrahigh strength steels basically have a dislocated martensitic structure with fine precipitates. The class can be subdivided into low-alloy steels, precipitation hardened stainless steels, maraging steels, and alloyed secondary hardening steels.

The alloy steels are heat-treated by austenitizing, a subsequent cooling to room temperature or even –70°C or below during which most of the austenite is transformed to martensite, and finally a tempering or aging treatment during which carbides and/or other hardening particles are precipitated. There are numerous differences between these steels, including the size and shape of martensite, the amount of carbon in solid solution, the amount of retained austenite, and the nature of the particles precipitated on aging. These steels are normally produced by vacuum induction melting or argon–oxygen decarburization melting. For high end use such as aerospace parts, these ingots

* Unless otherwise noted, the information in this section is largely extracted and summarized from Metals' Handbook.[1]

xygen decarburization melting. For high end use such as aerospace parts, these ingots are refined by vacuum arc remelting or electroslag remelting. After the melting process, these ingots are tailored into final shape by hot-working process, such as pressing, forging, and rolling, followed by cold-working processes, such as cold-rolling, drawing, and machining.

Representative alloys of each category and their compositions are shown in Table 1.1 with their Aerospace Materials Specification numbers. Their strengths and toughness levels are shown in Table 1.2, and 0.2% yield strength (YS) - fracture toughness (K_{Ic}) relationship is shown in Figure 1.1[1,2,3]. Below is a brief description of the physical metallurgy of these alloys.

Table 1.1 Chemical compositions of the ultrahigh strength steels used in aerospace industries (weight %).

		C	Ni	Co	Cr	Mo	Mn	Cu	V	Si	Al	Ti	Fe
#4340	AMS6414	0.4	1.8	-	0.85	0.25	0.7	-	-	0.2	-	-	Balance
300M	AMS6419	0.4	1.8	-	0.85	0.4	0.7	-	0.1	1.6	-	-	Balance
HP9-4-20	AMS6523	0.2	9	4	0.8	1	0.1-0.3	-	0.08	0.2max	-	-	Balance
HP9-4-30		0.3	9	4	1	1	0.15-0.3	-	0.08	0.1max	-	-	Balance
HY180		0.1	10	8	2	1	0.15	-	-	-	-	-	Balance
AF1410	AMS6527	0.16	10	14	2	1	-	-	-	-	-	-	Balance
15-5PH	AMS5659	0.04	4.6	-	15	-	0.25	3.3	-	0.4	-	-	Balance
PH13-8	AMS5629	0.04	8	-	13	2.2	-	-	-	-	1.1	-	Balance
C-250		0.005	18	8	-	4.8	-	-	-	-	0.1	0.4	Balance
AerMet100	AMS6532	0.23	11.1	13.4	3.1	1.2	-	-	-	-	-	-	Balance

Table 1.2 Mechanical properties of ultrahigh strength steels

Alloy	0.2%YS (MPa)	UTS (MPa)	K_{IC} (MPa$\sqrt{m}$)
#4340	1482	1965	71
300M	1689	1965	71
HP9-4-20	1276	1344	192
HP9-4-30	1413	1586	121
HY180	1276	1344	203
AF1410	1551	1689	187
15-5PH	1089	1124	132
PH13-8	1434	1551	81
C-250	1689	1724	110
AerMet100	1724	1965	126

Low-alloy steels: 4340, 300M

Alloy 4340 is typical of the low-alloy steels used in aerospace applications. This steel is normally tempered at or close to 200°C. After the tempering treatment (a first-stage temper) about 50% of the carbon has precipitated as carbides; these carbides are not cementite. Alloy 300M is essentially alloy 4340 modified by the addition of 1.6 mass% silicon; the silicon addition increases the yield strength and allows the steel to be tempered at higher temperatures than 200°C without the decreases in yield strength and toughness observed for 4340 steel tempered in the range of 250-300°C .

Precipitation hardened stainless steels (15-5PH, PH13-8) and Maraging steels (C250)

The martensitic precipitation hardened stainless steels (15-5PH, PH13-8) and the

maraging steel (C250) contain low carbon and are strengthened by the precipitation of particles during aging. These particles are copper (15-5PH), β-NiAl (PH13-8) and Ni_3Mo and Ni_3Ti(maraging steels). The maraging grades were first introduced in 1960, and PH13-8 and 15-5PH were being refined by Armco in the mid-1960s.

Alloyed secondary hardening steels: HP9-4-20, HP9-4-30, HY180, AF1410, AerMet 100

The alloyed secondary hardening steels HY180, AF1410, HP9-4-20, and HP9-4-3 are very similar. These alloys are normally aged at high temperatures – 510°C for HY180 and AF1410 and 565°C for HP9-4-20 and HP9-4-30. After aging, most of the carbon has precipitated as fine-alloy carbides, which have mostly M_2C structure, and provide the high strength. The cobalt addition is said to increase the driving force for carbide precipitation and delay dislocation recovery, thereby increasing the number density of the carbides and enhancing strengthening by the alloy carbides[4]. Alloys HP9-4-20 and HP9-4-30 were introduced by Republic Steel in 1962 and 1966, respectively, and HY180 was introduced by U.S. Steel in 1965. Alloy AF1410, developed in the mid-1970s by General Dynamics and later Cytemp, is HY180 modified by carbon and cobalt additions in order to achieve higher strength. Because of its well-balanced strength-toughness combination of AF1410, application of this steel has been wide-spread..

Further demand of better strength-toughness combination lead to the most recently developed alloy AerMet100, developed by Carpenter Technology Corporation, whose

nominal composition is 0.23C-13.4Co-11.1Ni-3.1Cr-1.2Mo-balance Fe in weight%[5,6,7]. This steel can achieve the strength level of C250 and 300M while maintaining the toughness level slightly below AF1410 (Figure 1.1).

Table 1.3 shows the conversion of the chemical compositions of HY180, AF1410, and AerMet 100 from weight percent to atomic percent. Comparing the amount of M_2C carbide by simply assuming all carbon content form M_2C carbide, it is clearly seen that the increase of strength and decrease of toughness among these three alloys are attributed to the precipitation hardening phase. On the other hand, according to the U.S. Patent of AerMet 100, this steel's high toughness is also obtained from controlled inclusion content by improved refinement technique and fine tuning of oxygen and sulfur getters, such as cerium and lanthanum[7].

From the specification for aerospace material of AerMet 100 (AMS 6532[8]) shown in Table 1.4, the levels of impurity such as Al, Ti, O, and N are severely restricted to very small values. This also controls the inclusion. The mechanical specifications of AMS 6532 are also shown in Table 1.5 for reference.

Table 1.3 Chemical compositions of the secondary hardening ultrahigh strength steels.

		C	Ni	Co	Cr	Mo	Fe	M_2C*
Weight	HY180	0.10	10.0	8.0	2.0	1.0	78.9	
percent	AF1410	0.16	10.0	14.0	2.0	1.0	72.8	
	AerMet 100	0.23	11.1	13.4	3.1	1.2	71.0	
Atomic	HY180	0.47	9.59	7.64	2.17	0.59	79.5	1.41
percent	AF1410	0.75	9.60	13.39	2.17	0.59	73.5	2.25
	AerMet 100	1.08	10.63	12.78	3.35	0.70	71.5	3.24

*Atomic fraction of M_2C is calculated by the multiplication of [C] by 3.

Table1.4 Compositional specification for the aerospace material of AerMet 100

	Nominal	AMS6532
C	0.23	0.21 / 0.25
Ni	11.1	11.00 / 12.00
Co	13.4	13.00 / 14.00
Cr	3.1	2.90 / 3.30
Mo	1.2	1.10 / 1.30
Fe	Bal.	Bal.
Si		≤0.10
Mn		≤0.10
P		≤0.008
S		≤0.005
Al		≤0.015
Ti		≤0.015
O		≤0.0020
N		≤0.0015

Table 1.5 Mechanical specification for the aerospace material of AerMet 100

	Longitudinal mechanical properties	
Tensile properties	Ultimate tensile strength	≥ 1931 MPa
	0.2% offset yield strength	≥ 1620 MPa
	Elongation in 4D	≥ 10%
	Reduction of area	≥ 55%
Fracture toughness	K_{IC}	≥ 110MPa$\sqrt{m}$
Hardness	HRC	≥ 53

1.3 Physical metallurgy of AerMet 100

Intensive research on the optimization of alloy composition[9], the optimization of aging [10], and the mechanical property-microstructure relationship[11,12,13,14,15] has been conducted, and this research will be reviewed in this section.

After a hot-working process to produce a near-net shape of AerMet 100, the recommended heat treatment is as follows [4].

- Intercritical annealing: 677°C /16hrs (also accomplishes stress relief)

- Solution treatment: 885°C /1hr

- Quenching: Water quenching is not recommended, but the parts should be cooled to 66°C in 1 to 2 hours.

- Deep Freeze: -73°C or below/1hr/Air Warmed

- Aging: 482°C /5hrs

Treated as above, a high strength/toughness combination is believed to result from the following microstructural features and mechanisms. A schematic TTT diagram of AerMet 100 is drawn in Figure 1.2.

1) Fine prior austenite grain size during the hot-working process gives high resistance to cleavage fracture[13,14]. Even many high angle boundaries among adjacent laths are observed,[11,13,14] and this also attributes to the increase of toughness.

2) Very little retained austenite remains in the deep frozen condition from X-ray diffraction analysis.[13] After aging at 482°C, a very small amount of austenite is seen at the lath boundaries, but some amount of austenite at prior austenite grain boundaries is seen. There is no clear distinction between retained austenite or reverted austenite. If the aging temperature is raised up to 510°C, reverted austenite can be seen not only at the prior austenite grain boundaries but also at lath boundaries.

3) The precipitation hardening phase has a needle shape. These precipitates are believe to be largely M_2C carbides if aged at 510°C, but if aged at 454°C they basically have coherency along $<100>_\alpha$, and form G.P. zone type phases. At the optimum 482°C aging condition, some lose their coherency and have M_2C crystalline structure, but most of them are still coherent and seem to be acting as precursors for M_2C precipitation from TEM bright field image[11]. If the aging temperature is high, this phase loses the coherency and both toughness and strength decrease, and if it is low (underaging), cementite instead of M_2C forms at lath/plate boundaries, which deteriorates the toughness a lot.

4) High temperature aging above 510°C causes coarsening of M_2C, increasing reverted austenite, and recovery of martensite, and all of these decrease the strength and toughness. [11]

5) Undissolved carbides such as MC, M_2C, and M_7C_3 are reported,[11] but their effect on mechanical properties is not known.

These papers give us suggestions for improving the toughness. To implement these, we have to understand the effect of inclusions, the work-hardening behavior, the ductile-brittle transition, and how to control the microstructure in detail. Studying the overaging condition may show interesting results since overaging introduces reverted austenite and decohesion of M_2C carbides. Skipping the deep freeze treatment is also of interest since this gives us information on the role of retained austenite. Although the effect of prior austenite grain size and packet size is well studied by many steel metallurgists,[16,17,18,19,20,21,22,23,24] this is still worth examining in detail for this specific alloy. These heat treatment conditions were studied and the details are shown in chapter 4.

1.4 Mechanisms of fracture in steel

1.4.1 Fracture mechanisms and ductile-brittle transition

While the sources of strength and toughness in ferritic steels are not fully understood, the simple relations that are diagrammed in Figure 1.3 suffice for most alloy design purposes[25]. The basic relation between the fracture toughness and the temperature is shown Figure 1.3a. The fracture toughness drops dramatically over a relatively narrow temperature range that defines the ductile-brittle transition in temperature (T_B). The ductile-brittle transition is caused by a change in the fracture mode from ductile rupture to transgranular cleavage or intergranular separation. If the steel is to have high toughness at its intended service temperature, T_B must be decreased to below the service temperature and the fracture toughness in the ductile mode must be raised to an acceptable value.

The fracture toughness of a typical ductile alloy is related to its yield strength by a relation like that shown in Figure 1.3b. The strength-toughness characteristic is controlled by the flow properties of the matrix and by the density and efficacy of the ductile void count, which reflect the chemical purity of the alloy. One can increase the toughness above T_B by processing the alloy to lower its strength or decrease its inclusion content, but the former is not the good solution for ultrahigh strength steels since designers of the aircraft parts always put the strength first in their design. Hence controlling the inclusion content seems to be the most important task for improving the toughness in the upper shelf regime. Since the high impact toughness of AerMet 100 at ambient temperature is achieved by its ductile fracture mode, close analysis of its ductile fracture is key to understanding why such a wide variation of toughness was obtained.

The ductile-brittle transition can be usefully described in terms of the "Yoffee diagram" at Figure 1.3c. The Yoffee model is oversimplified, but nonetheless contains the most important alloy design criteria in a compact form. It attributes the ductile-brittle transition to a competition between plastic deformation and brittle fracture. At a critical value of the yield stress (σ_c), the material ahead of an embedded flaw fractures in a brittle manner before blunting. As the temperature is lowered, the yield strength of the alloy rises until it exceeds σ_c. The crossover point determines T_B. Since there are at least two independent brittle fracture modes, transgranular cleavage and intergranular separation, there are at least two critical stresses. The transition temperature and the brittle fracture mode are determined by the least value of σ_c.

The Yoffee diagram suggests that T_B can be decreased by lowering the alloy strength or by raising its resistance to fracture in the dominant brittle mode. While both approaches have been used successfully, the preferred tactic is to raise the resistance to brittle fracture, again since high strength is a desirable characteristic of structural steel. This is done by identifying the brittle fracture mode and its relation to the microstructure.

It should be noted that T_B varies dramatically with the testing method due to different geometry, constrains, strain rate and so on. For example, uniaxial tensile tests will have higher T_B than notch bar tests, such as Charpy and K_{Ic} tests.

If the fracture is intergranular, its source is mostly a grain boundary contaminant, such as the metalloid impurities S and P in steel[26,27,28] or an inherent weakness of the grain boundary.[29,30] In the case of chemical embrittlement, the alloy may be purified of deleterious surfactants, alloyed to getter these into relatively innocuous precipitates, or heat treated to avoid the intermediate temperature regime at which these impurities segregate most strongly to the grain boundaries. When the grain boundaries are inherently weak, the metallurgical solution is the addition of beneficial grain boundary surfactants that serve to glue them together. The most prominent of the beneficial surfactants is boron, (first discovered and applied in this laboratory[31,32]) which is extremely effective in suppressing intergranular fracture in Fe-Mn steels and in Ni_3Al intermetallics.

When the brittle fracture mode is transgranular, as it is in typical ferritic steels, the

ductile-brittle transition can be suppressed by decreasing the effective grain size of the alloy, which is the mean free path for cleavage fracture. In many lath martensitic steels, the effective grain size is the packet size in which laths have a close crystallographic alignment. Two methods have been successfully used to refine the grain size by breaking up these packets, i.e. intercritical anneal and intercritical temper.

In the case of AerMet 100, a fine effective grain size seems to be achieved by the annealing treatment prior to the solution treatment, which is essentially an intercritical annealing in γ and α two phase region near the A_1 temperature. It creates a fine-scale lamellar "dual-phase" structure with two different compositions.[14] In the subsequent austenitization treatment, these two phases transform into martensite at different temperatures, and give rise to disoriented lath boundaries and form sub-micron effective grain size.

The other heat treatment, "intercritical temper," had not, to our knowledge, been tried earlier for AerMet 100. The intent of this temper is to introduce thermally stable austenite of spheroidal shape[33] or continuous narrow band[34,35] at the lath and prior austenite grain boundaries. Hence the packets are disrupted, and the effective grain size is reduced. As explained in section 1.3, overaging around 510°C for AerMet 100 creates a continuous narrow band of austenite at lath and prior-austenite grain boundaries. If we can create a small amount of austenite for the grain refinement without losing the coherency of the precipitation hardening phase (the precursor of M_2C), this may further improve the toughness of this steel. Therefore, short time temper treat-

ments (15min. and 30 min.) at 510°C were chosen prior to the aging treatment (the results will be discussed in Chapter 4).

1.4.2 Mechanism of ductile fracture

1) Ductile fracture sequence

Since the fracture mode of properly treated AerMet 100 is known to be ductile[10,11], understanding the ductile fracture process in detail is important. A schematic diagram of the ductile fracture sequence[36] is shown in Figure 1.4.

Consider a body with a sharp crack and two different kinds of particles. One type of particle is bigger than the other, and it is weakly bonded to the matrix. These primary particles are usually inclusions, such as oxides, sulfides, phosphates and others, and can be regarded as pre-existing voids in the material.[37] The other type of particle is relatively small and more strongly bonded to the matrix. Undissolved carbide from the austenitizing heat treatment is an example of this kind of particle.

When an external stress is applied to the pre-cracked structure (Figure 1.4a), plastic deformation at the crack tip takes place with the high stress intensity near the crack tip (Figure 1.4b). This step is called blunting. This blunting process is governed by the material's inherent ductile strength. Here, the inherent strength is defined as a strength that is controlled by its fine microstructure such as dislocation density, precipitation carbides, lath and packet sizes of martensite, retained or reverted austenite, etc.

At the same time or slightly later in this blunting stage, void nucleation from the large

primary particles happens due to the decohesion of the interface boundary or the shattering of these particles under the high triaxial stress state. (Blunting is actually helpful to reduce the stress intensity, but any further increase of the stress is accompanied by the decrease of the effective area by void growth, which increases the local stress near the crack tip.) Finally the local stress goes up to the level where the decohesion of the interface boundary at secondary particles takes place and this decohesion and shear localization results in void sheet coalescence. Then the body fractures. Here the void sheet formation is explained with the aid of secondary particles, but these particles are not always necessary. Since the ligament between the voids doesn't have a triaxial state of stress any more, it will behave like a tensile test specimen, and the work hardening character of the material will decide the final morphology of the fracture. The nature of the final fracture should resemble that of a tensile specimen.

The metallurgical determinants of each of these three steps (that is, blunting, void nucleation, and void coalescence) in AerMet 100 must be characterized and how each of these steps affects the fracture toughness values must be fully understood.

2) Models of ductile fracture

While there are a number of distinct theories of the microvoid coalescence mechanism of ductile fracture[38,39,40], they have common features and lead to similar qualitative results. However, there still are many uncertainties regarding the prediction of the nucleation of secondary voids and regarding a failure criterion that governs void coalescence. The failure criterion must somehow account for work hardening during

initial void growth and unstable void growth due to fracture or unstable plastic deformation of the matrix material between them. The usual approach is to assume a regular distribution of voids and predict failure when the stress in the intervening material reaches the critical value for necking or fracture.

For a given inclusion distribution the ductile fracture theories all lead to models of the general form[41,42,43,44,45]

$$K_{IC} \propto \sqrt{\varepsilon_f E \sigma_0}\,, \qquad (1.1)$$

where ε_f is the strain to failure, E is Young's modulus, and σ_0 is the flow stress, whose precise definition varies slightly from one model to another. σ_0 is taken to be yield strength, ultimate tensile strength, or fracture strength in tensile test. In any case, the explicit dependence of the fracture toughness on the flow stress suggests that the two should vary together, in contrast to isothermal toughness data that invariably shows a decrease in toughness with the strength. The resolution of this discrepancy lies in the dependence of the failure strain on the flow stress; ε_f generally decreases strongly and monotonically with σ_0 at constant temperature. But if there is a way to increase the ε_f in more efficient way than the decrease of σ_0, K_{Ic} could be improved. ε_f is usually taken to be strain at fracture. But we can also assume that the failure strain in eq. (1.1) might scale roughly with the uniform elongation (more precisely, with the true strain at the ultimate tensile strength (UTS)), which is given by the necking criterion,

$$\frac{d\sigma}{d\varepsilon} = \sigma\,, \qquad (1.2)$$

where $d\sigma/d\varepsilon$ is the true work hardening rate and σ is the true stress. Since the austenite phase has different work hardening behavior than the alpha phase (martensite), monitoring work hardening is meaningful. The comparison of the substitution of the strain at UTS and 0.2% yield strength with the strain and strength at fracture will be examined at the end of Chapter 4.

Since J_{Ic} and K_{Ic} are related by the following equation,[46]

$$K_{Ic} = \sqrt{J_{Ic}\frac{E}{(1-\nu^2)}}, \qquad (1.3)$$

equation 1.1 implies that J_{Ic} follows the proportionality rule

$$J_{Ic} \propto \varepsilon_f \sigma_0 . \qquad (1.4)$$

According to Ritchie *et al.*[45], equation 1.4 is nearly equalized by using characteristic length, l_0*,

$$J_{Ic} \approx \varepsilon_f \sigma_0 l_o^* . \qquad (1.5)$$

In case of microvoid coalescence mechanism, l_0* typically scales as a multiple of the mean distance between microvoid-producing particles, and this is a measure of the blunting size at the crack tip.[45]

The final parameter that may significantly influence the toughness of ductile materials is the inclusion density, which determines the density of nucleated microvoids that lead to failure. The ductile fracture theories suggest that

$$J_{Ic} \propto \frac{\sigma_0}{\sqrt{N_V}}, \qquad (1.6)$$

where N_V is the volume density of active inclusions.[47] Equation 1.5 has essentially the same form if the characteristic length scales as inclusion spacing. Interestingly, the models predict that the inclusion count has a much stronger influence on the fracture toughness as the yield stress rises, which suggests that the effect should be most apparent in the highest strength ductile steels, such as AerMet 100. This prediction is in qualitative agreement with a number of recent observations on the behavior of ductile cryogenic steels.[47]

Models using the information of fractographs are also proposed. One of the models which seems to work well for ultrahigh strength steels is the Garrison's model. Garrison and his coworker studied the K_{Ic} dependence on inclusions in AF1410.[48,49,50,51] They modified the Rice and Johnson model[52] by taking into the account of the result of McMeeking's numerical calculations of void growth.[53,54]

According to their model, the crack tip opening displacement at fracture initiation, δ_{IC}, scales as

$$\delta_{Ic} \propto X_0(\overline{R_V / R_i}), \qquad (1.7)$$

at least for some high strength steels, where Xo is the average three-dimensional nearest neighbor distance between inclusions, and $(\overline{R_V / R_i})$ is the average of primary void radius (Rv) divided by the radius of the inclusion nucleating the void (Ri), here we

call (*Rv/Ri*) as void growth factor. *Xo* is calculated by the relationship,[55]

$$X_0 = 0.89R_0 / f^{1/3}, \qquad (1.8)$$

where *Ro* is the average inclusion radius and *f* is the volume fraction of the inclusion, which was assumed equal to the areal fraction.[56]

The crack tip opening displacement, δ_{Ic}, is evaluated by the following relationships.[57]

$$\delta_{Ic} = d_n(J_{Ic} / \sigma_y) \qquad (1.9)$$

This value d_n is a function of work hardening coefficient, n, yield stress, σ_y, and Young's modulus, E, based on calculations by Shih.[57] The higher n and E, and the lower σ_y are, the smaller d_n becomes. According to this model, fracture toughness, J_{Ic} increases with crack tip opening displacement, δ_{Ic}, and yield strength, σ_y, and decreases with d_n. For higher δ_{Ic}, and therefore J_{Ic} at constant σ_y and d_n, a lower volume fraction of primary particles or higher void growth factor or both is required. The primary voids will tend to grow until the intervoid region coalesces via secondary void sheet formation or until the primary voids impinge upon each other. Thus a larger void growth ratio and lower primary particle volume fraction would be beneficial for fracture toughness.

Equations 1.1 through 1.9 were examined for three heats of AerMet 100 to determine if these models were applicable to AerMet 100.

2. EFFECT OF INCLUSIONS ON TOUGHNESS

2.1 Introduction

Experiments in this chapter were conducted to examine the following features of AerMet 100 by using three different heats of AerMet 100:

1) The general properties of AerMet 100, i.e. microstructures and mechanical properties.

2) The wide variation of toughnesses unveiled in the step 1) and quantitative analysis of this toughness variation from each step of the ductile fracture.

2.2 Experimental Procedure

2.2.1 Materials and heat treatment

Bars of three randomly selected heats of AerMet 100 produced by Carpenter Technology were used in this study. Chemical analysis of these three heats was conducted at Hitachi Metals, Ltd. at one time to increase the accuracy of the analysis of trace elements. The bars had the dimensions of approximately $100mm^{W}$ x $32mm^{T}$ x $2.7m^{L}$, and they all came in as-annealed condition. All the experiments for Heat #1 and #2 were conducted at the Lawrence Berkeley National Laboratory. The tensile test and the fracture toughness test of Heat #3 were conducted by the Naval Air Warfare Center. Mechanical test specimen blanks were cut from the material, and then austenitized at 885°C for 1 hour, quenched in oil to room temperature, transferred to a liquid nitrogen

bath (-197°C) and kept for 1 hour, then warmed to room temperature in air. Finally, they were aged at 482°C for 5 hours. Tensile and compact tension (CT) specimens were then machined in the L-orientation and L-T orientation, respectively, from the heat-treated blanks.

2.2.2 Microstructural analysis

1) Optical microscopy

Specimens for optical microscopy were cut from the heat-treated blanks. The plane perpendicular to the longitudinal direction was polished and etched by an acidified $FeCl_3$ solution, 200ml HCl + 200ml H_2O + 20g $FeCl_3$, to reveal the microstructure.

2) Transmission electron microscopy

Thin specimens for TEM were cut from the heat-treated blanks, then ground to about 75μm, and electropolished in a perchloric acid-methanol solution at –40°C. Carbon extraction replicas were used to observe the prior austenite grain size and analyze fine precipitates by energy dispersion spectroscopy (EDS).

2.2.3 Mechanical properties

1) Heats #1 and #2

Tensile properties were determined using 3.2 mm x 3.2 mm square cross section area and 25.4 mm gage length flat tensile specimens. The tests were conducted at an initial strain rate of 5.0×10^{-4} per second at room temperature.

Fracture initiation toughness level was determined by the J-integral fracture toughness test method according to ASTM E-813-89, using the single specimen unloading compliance method. Compact tension specimens without side grooves were used. K_{Ic} was evaluated by equation 1.3, where values of Young's modulus, E = 194.6GPa, and Poisson's ratio, ν = 0.28, were taken from Carpenter Alloy Data.[4]

Critical crack tip opening displacement, δ_{IC}, was evaluated from equation (1.9). dn in equation (1.9) was obtained from Shih's plot in plane strain condition[57]. The average work hardening coefficient, n, was calculated from the slope between 0.2% yield strength and ultimate tensile strength in log ε – log σ plot of Heat #1 and #2, and average of all tensile data, 0.114 was used for the n value. The calculated number, d_n = 0.57, was used for the evaluation of δ_{IC} for all heats. This value is close to the number of Garrison's analysis for AF1410[49], i.e. d_n =0.6. All these values were also used for the evaluation of Heat #3 since the tensile properties obtained from the Naval Air Warfare Center were not complete.

2) Heat #3

Mechanical tests on Heat #3 were conducted by the Naval Air Warfare Center. The tensile tests were performed using round cross section specimens, and K_{Ic} tests were conducted by ASTM E399-90 using compact tension specimens. J_{Ic} and δ_{Ic} values were calculated by using equations (1.3) and (1.9), respectively.

2.2.4 Inclusion characterization and fractography

Specimens for optical microscopy were re-polished carefully so that no harmful scratches appeared on the surface used for the particle counting. The overall particle density for large inclusion sizes was determined at low magnification to estimate the two-dimensional mean particle spacing, $1/\sqrt{N}$, using equation 1.6. Optical microscopy images of polished cross sections were taken at 50x magnification, over a total area of 36 mm^2. The number of particles whose diameters were larger than approximately 2 μm was counted.

Detailed particle measurements were obtained from optical microscope images of the same sample taken at 400x using a digital analysis system. A total area of 0.35mm^2 was used to determine the particle volume fraction, f, the average particle radius, R_0, and the average three dimensional particle spacing, X_0, as noted in section 1.4.2-2. The minimum resolvable particle area was 0.07 μm^2 (equivalent to a 0.3 μm diameter) based on the estimated resolution of the imaging system.

Fractographs of the fracture surfaces were used to determine the extent of void growth. The fractographs were taken just ahead of the stretch zone at a magnification of 1500x. From these fractographs, voids containing particles were identified and the area of the void and the nucleating particle were measured. The void and particle radii were calculated from the measured area using the assumption of spherical voids and particles. In cases where the particles had fractured, an average radius was calculated from the combined calculated volumes of the fragments. Void growth factor was calculated

using the void radius, R_v, divided by the radius, R_i, of the particle nucleating the void.

The same fractographs as for the primary void growth were also used for both the evaluation of secondary void coalescence, and the measurement of dimple size in the coalescence sheet area. The number of secondary voids was counted in the area of about 0.25 mm^2, then the mean secondary void spacing was calculated by taking the inverse of square root of the secondary void density. Then this process was repeated 3 times to get the mean value for the secondary void spacing.

2.3 Experimental Results

2.3.1 Chemical composition

The results of the chemical analysis for all three heats are shown in Table 2.1. The main alloying elements of Heat #1 to #3 are almost the same except for a small change in the Co content in Heat #3. On the other hand, the amount of oxygen, and rare earth metals in Heat #1 is much less than that in Heat #2, and the amount in Heat #3 is located in the middle. These three heats all meet the specifications of AMS 6532 in Table 1.4.

Table 2.1 Chemical compositions (weight %)

	Heat	1	2	3
Main elements (weight%)	C	0.22	0.22	0.23
	Mo	1.22	1.18	1.19
	Cr	3.00	2.93	3.07
	Ni	11.31	11.08	11.14
	Co	13.58	13.48	13.16
	Fe	Bal.	Bal.	Bal.
Trace elements (ppm)	Al	20	30	40
	Ti	120	100	140
	P	30	30	30
	S	5	4	8
	O	3	12	6
	N	7	5	5
	Ce	8	72	20
	La	4	22	4
	Nd	8	20	3
	Pr	<10	<10	<10

2.3.2 Microstructure

Optical micrographs in Figure 2.1 show relatively messy martensitic microstructures, but all three heats seem to have a similar prior austenite grain size of about 10 μm. The TEM bright field image of Heat #1 in Figure 2.2 also shows about a 10 μm prior austenite grain structure, and a lath microstructure that is not well oriented. Figure 2.3 shows the orientation relationship between adjacent laths, and it illustrates that there are two variants within a packet and the laths are decomposed into crystallographically

distinct subvolumes that are smaller than 0.5 μm. Previous papers also report these fine microstructures and correlates Aermet 100's high toughness with this fine effective grain size.[11, 12, 13, 14] A TEM image of the extraction replica of Heat #1 is shown in Figure 2.4. The prior austenite grain size is clearly shown in Figure 2.4-ato be about 5 to 15 μm. Higher magnification in Figure 2.4-b) reveals that there are two types of precipitates, one about 50 to 300 nm in diameter and the other about 5 to 30 nm. Small size precipitates were too small to obtain enough EDS counts for analysis, but the EDS analysis for the large size precipitate shown in Figure 2.4-c was obtained, and it showed very high Cr counts with a small amount of Fe. From Ayer and Machmeier's work[11], it is reasonable to assume the large precipitates to be $M_{23}C_6$, and the small precipitates to be MC carbides. TEM analysis on Heat #2 showed almost the same result as Heat #1, but TEM analysis was not done for Heat #3 due to the limited number of available blanks. The carbide spacings are roughly examined from approximately 350 μm^2 of the extraction replica image. The results for Heats #1 and #2 are 1.94 μm and 1.74 μm, respectively.

2.3.3 Mechanical properties

The results of the mechanical tests on AerMet 100 are shown in Table 2.2 and in Figures 2.5 and 2.6. The relationships between K_{Ic} vs. 0.2% offset yield strength, and K_{Ic} vs. ultimate tensile strength are plotted in Figure 2.7. The published data of AerMet 100 by Novotny[10] is also shown in Figures 2.5 through 2.8 for comparison.

Table 2.2 Mechanical properties of AerMet 100 among three heats

		Tensile properties			Fracture properties		
Heat	specimen	0.2% Y.S. (MPa)	U.T.S. (MPa)	total elon. (%)	J_{IC} (kJ/m^2)	K_{IC} (MPa$\sqrt{m}$)	δ (μm)
1	1	1775	1946	9.4	173.1	191.2	55.7
	2	1769	1935	9.6	157.6	182.4	50.7
2	1	1682	2043	10.7	64.8	117.0	21.8
	2	1705	1992		59.4	112.0	20.0
	3				51.3	104.1	17.3
3	1	1731	1917		100.9	146.0	33.2

The 0.2% offset yield strengths (YS) and ultimate tensile strengths (UTS) of the three heats are almost the same and they are comparable to Novotny's (Figure 2.5). However, we see higher fracture toughness values for Heat #1, and lower values for Heat #2 than Novotny's. Only Heat #3 shows almost the same level as Novotny's. Errors coming from the test conditions are obviously much smaller than the difference between the heats. The effect of heat treatment on the toughness-strength relationship as examined by Novotny is shown in Figure 2.7. These data fit a single trend line with slight deviations, which is a typical result for high strength steels. If we try to increase the toughness, the strength goes down, and if we try to increase the strength, the toughness decreases. The data for the optimum heat treatment condition obtained by Novotny are located near the results for Heat #3. Therefore the location of Heat #1 is understood as the extremely high toughness-strength combination. Heat #2, on the other hand, has the lowest toughness-strength combination.

Fractographs of a typical CT specimen are shown in Figure 2.8. It clearly shows that the fracture occurred by ductile rupture. Furthermore, the fracture surfaces consist of essentially two different types of dimples. One set consists of the primary voids, which often contains particles and are relatively large. The other set consists of secondary voids which are relatively small and only some of which contain small particles on the order of several tens of nanometers. In primary voids, large particles above 1 μm were able to be identified, and they were determined to be mainly oxysulfides or oxyphosphates of rare earth metals by the EDS analysis. However, smaller particles less than 0.5 μm in size were difficult to analyze because of their small size relative to the probe. Extraction replicas of fracture surfaces were also attempted, but only large oxysulfide or oxyphosphate particles could be extracted, and smaller particles were not able to be identified.

2.3.4 Inclusion characterization

Low magnification (50x) optical micrographs of polished specimens of three heats of AerMet 100 are shown in Figure 2.9. These micrographs clearly reveal the difference of particle counts in the matrix. Pictures are shown as the order of toughness values (high to low from left to right) so that the tendency can be easily seen. These micrographs show the typical number of particles in the cross section. The high toughness heat contains the smallest number of particles and the low toughness heat contains the largest number of particles. From analysis of the polished surfaces, large particles were again identified as oxysulfides or oxyphosphates using EDS analysis, but smaller

particles were difficult to identify since they were too small relative to the probe size of EDS. They could be non-metallic inclusions or large $M_{23}C_6$ particles.

The areal particle spacing for large particles is tabulated in Table 2.3 and is plotted against fracture toughness in Figure 2.10. It is apparent that better fracture toughness is obtained by wider particle spacing. Since the minimum resolvable particle diameter is around 2 μm, it is assumed they are almost all non-metallic inclusions. This plot basically follows the model in equation 1.6 because the yield strengths of all three heats have almost equal values.

The parameters related to the inclusion particle count obtained from a high magnification (400x) analysis of cross sections and fracture surfaces are tabulated in Table 2.3. There, the higher toughness heats tend to have smaller inclusion volume fractions, wider 3-D particle spacings, and greater void growth factors, but the average particle radius doesn't vary substantially. Since the inclusion volume fraction of AF1410 was reported as 0.00036[49], these numbers seem to be reliable.

Figure 2.11 shows the size distributions of the particles observed on the fracture surfaces of compact tension specimens. The median value is about 0.5 μm for all heats. But the heats are different in their distribution of large particles. The distribution tends to be more skewed for low toughness heats, and they have larger maximum sized particles. Figure 2.12 shows the relationship between void radius, R_v, and particle radius, R_i, sitting in the void. Void radius is proportional to particle radius up to around R_i = 1.0 μm. Thereafter, the relationship becomes non-linear, but still monotonic

Table 2.3 Microstructual properties of AerMet 100 among three heats.

				Heat #1 (High K_{IC})	Heat #3 (Medium K_{IC})	Heat #2 (Low K_{IC})
Polished cross section	Low magnification analysis (50x) - 36 mm^2	inclusion spacing	$1/\sqrt{N}$ (mm)	0.79	0.39	0.29
	High magnification analysis (400x) - 0.35mm^2	volume fraction	f (-)	0.00028	0.00046	0.00067
		harmonic mean inclusion diameter	H(d) (μm)	0.630	0.666	0.668
		average inclusion radius	Ro (μm)	0.495	0.523	0.525
		3-D inclusion spacing	Xo (μm)	6.7	6.0	5.3
Fracture surface	SEM analysis (1500x)	Average void growth factor	$(\overline{Rv/Ri})$ (-)	6.8	5.4	4.7
(Inclusion spacing)*(Void growth factor)			Xo $(\overline{Rv/Ri})$	45.6	32.5	24.7

growth is seen. The effect of initial particle size on void growth can be seen more clearly by plotting the void growth factor, R_v/R_i, against particle radius, R_i (Figure 2.13). Voids initiating from smaller particles tend to show more growth relative to their initial sizes those initiating from large particles. This deviation from linearity could be caused by the impingement of the neighboring voids because the apparent void diameters in this region are bigger than 3-D average inclusion spacing.

Critical crack tip opening displacements, δ_{IC}, of AerMet 100 are plotted against the parameter, $X_0(\overline{R_V / R_i})$, where X_0, is the average 3-D particle spacing, and $(\overline{R_V / R_i})$ is the average void growth factor. We also show the data of other high strength steels examined by Garrison *et al.*[49](Figure 2.14). The δ_{IC} values for AerMet 100 show a linear relationship to $X_0(\overline{R_V / R_i})$, and those values matches Garrison's model very well, though the slope of the trend line is slightly steeper than one. They also lie in the range of the data obtained by Garrison *et al.*[49]

Figure 2.15 shows an example of a secondary void analysis of Heat #1. Secondary void spacings were calculated from the black and white image of the secondary void sheet coalescence area. Secondary void spacings of three heats are shown in Table 2.4 and Figure 2.16 with their standard deviations. They have similar values irrespective of their different toughness levels, and show that Garrison's model only holds for the primary void distribution. Interestingly, these spacings are comparable with the carbide spacings examined from the extraction replica.

Table 2.4 Secondary void spacing (μm)

	Heat #1 (High K_{IC})	Heat #3 (Medium K_{IC})	Heat#2 (Low K_{IC})
Mean	1.261	1.270	1.330
Standard deviation	0.123	0.094	0.068

2.4 Discussion

The fracture of all three heats of AerMet 100 occurred in a fully ductile manner, though their toughness levels were quite different. As noted in section 1.4.2, ductile fracture occurs in three steps, i.e. blunting, void nucleation and growth, and void sheet coalescence. Our data suggests that the void nucleation and growth process seem to be dominating the fracture toughness, but still microstructural features in each step should be examined carefully.

2.4.1 Inherent strength effects on blunting

Microstructural features such as prior austenite grain size, lath structure, and undissolved carbide distribution, do not differ greatly between high toughness and low toughness bars in the above section. In addition, the 0.2% yield strength and ultimate tensile strength levels are almost equivalent (Table 2.2). Hence the inherent strengths of the three heats, at least in the early stage of deformation, appear to be the same. However, a close analysis of the work hardening behavior, the reduction of area, the strength of grain boundaries, the cleavage fracture strength, and so on should be performed to discuss the inherent strength for blunting since fracture toughness meas-

ures the strength and deformability under highly hydrostatic tensile stress and the ductile brittle transition temperature, T_B, might be very close to the testing temperature under this kind of geometry. Furthermore, inclusion content acts on inherent strength due to the shear localization, and eventual blunting process.

2.4.2 Secondary voids effects on microvoid coalescence

The final microvoid coalescence process is discussed before void nucleation and growth process since the experimental results obtained for microvoid coalescence didn't show any effect on the toughness or the strength of Aermet 100. As shown in Table 2.4 and Figure 2.16, microvoid coalescence processes in the three heats all end with a secondary void spacing of around 1.3 μm. The secondary voids could be formed by void nucleation from the secondary particles, or by simple micro-tears. If void nucleation dominates, the secondary particles nucleating voids appear to be carbides, such as $M_{23}C_6$ and MC since these spacings (about 1.8 μm) are in the same order as secondary void spacings.

2.4.3 Inclusion content effects on void nucleation and growth

As discussed above, it appears that all other microstructural parameters except inclusion distribution are nearly the same for the three heats. Given this information and that shown in Figure 2.10, it is simple to state that the inclusion content is dominating the fracture toughness of AerMet 100This provides a great tool for the evaluation and control of fracture toughness. From an engineering point of view, two dimensional analysis is relatively easy to do, and specifying the distribution of inclusion greater

than approximately 2 μm diameter would be an effective quality control tool for the fracture toughness for this alloy. Eliminating the large inclusions and expanding the inclusion spacing leads to toughness improvement.

For the use of Garrison model, the inclusions which nucleate the primary voids should be estimated first. The large particles sitting in voids on the fracture surface were identified as oxysulfide or oxyphosphate, but smaller particles could not be identified. A comparison can be made of the inclusion volume fractions as measured by polished cross section and that obtained by analysis of impurity chemical composition. This provides an independent verification of the applicability of the Garrison model shown in Figure 2.14 The amount of non-metallic inclusion can be calculated from the chemical composition assuming that 1) S, P, Ce, La, Nd, and Pr creates inclusion which has a form of $(REM)_2(O,S)_3$ and has the density of 6 g/cm^3, and 2) excess O forms Al_2O_3, and excess S forms TiS. The calculated values from the chemical compositions are compared with the measured values from the polished cross sections in Table 2.5.

Table 2.5 Comparison of particle volume fraction between the measured values and the calculated values from chemical compositions

	Heat #1 (High K_{IC})	Heat #3 (Med. K_{IC})	Heat #2 (Low K_{IC})
From polished cross section	280	460	670
Rough estimation from chemical composition	38	55	178
Excess amount of particle	242	405	492

(unit: x10^{-6})

Values obtained from the polished cross sections show higher inclusion volume fraction than the estimation from chemical composition. Taking into account the fact that that most of the void nucleating particles have the radii around 0.5 μm, and $M_{23}C_6$ carbide have radii around 0.05 to 0.3 μm, the primary void nucleating particles might have two different chemistries, one being a rare earth metal oxide and the other being a carbide. If we assume large undissolved carbides are associated with the primary void nucleation process, the large difference of volume fraction in Table 2.5 can be understood. Another source of error might come from the digital analysis system. Since particles on polished cross sections typically have a hillock shape, they might create shadows. Black and white images used in the areal fraction may be adversely affected by these shadows. Since this is especially true for large inclusions, samples with more large inclusions, will have larger error in comparison with one which has fewer large inclusions in it.

Even considering these possible errors, the result in Figure 2.14 is intuitively correct. Fracture toughness values can be improved by increasing either the inclusion spacing or void growth factor. In case that inclusion volume fraction is difficult to reduce, making larger inclusions will increase the inclusion spacing (in this case, however, one must watch to see if the void growth factor decreases at the same time). Increasing the void growth factor is not obvious but a close analysis of the work-hardening behavior of AerMet 100 may give some indication of how it may be accomplished.

2.4.4 Improving the toughness

From the result and discussion in this chapter, increasing the particle spacing seems to be the only way to improve the toughness without sacrificing the strength. If the inclusion content is maintained at the level of Heat #1, the fracture toughness (180MPa$\sqrt{m}$) will be well above the specification ($\geq$ 110MPa$\sqrt{m}$) in Table 1.5, and the product will achieve the best combination of strength and toughness of any ultrahigh strength. But maintaining this low level of inclusion content seems to be difficult judging from the results from the other two heats.

Further improvement of fracture toughness from the level of Heat #1 is even more difficult. K_{Ic} is proportional to square root of J_{Ic} or δ_{Ic} , hence the linearity between inclusion spacing and J_{Ic} or δ_{Ic} obtained in this study only bears the square root relationship with K_{Ic}. That means if we try to increase the K_{Ic} for 10%, we need to increase the inclusion spacing 20%; a 30% increase requires 70% increase of inclusion spacing. However, if smaller primary voids played an important role in determining fracture toughness and if they were created by undissolved carbides, then by finding the optimum austenitization temperature or modifying the alloy composition(such that the prior austenite grain size is very small and large carbides are dissolved) we may be able to obtain a large inclusion spacing. On the other hand, if the fracture toughness is controlled by large inclusions as is indicated in Figure 2.10, achieving further reduction of inclusion volume fraction is going to be tough. Still, reduction of non-metallic inclusion volume fraction is really attractive, at least at the experimental level.

2.5 Summary

From the comparison of three heats of AerMet 100 all with the standard heat treatment, the results can be summarized as follows:

1) Fracture toughness showed a wide variation among three heats though their tensile strength levels were similar.

2) This wide variation of toughness values is mainly due to inclusion content. The wider inclusion spacing due to the lower inclusion volume fraction, and the subsequent increase in void growth factor contributed significantly to the fracture toughness.

3) One kind of particle that nucleates primary voids is oxysulfide or oxyphosphate of rare earth metals. Undissolved carbide might also be a nucleation site of primary void.

4) Microstructural features such as prior austenite grain size, lath structure, undissolved carbide were similar between Heats #1 and #2.

5) Secondary void spacings on microvoid coalescence sheet were similar among three heats.

6) Maintaining the inclusion content in the level of Heat #1 can improve the toughness of AerMet 100 on a large scale.

3. DUCTILE-BRITTLE TRANSITION OF AERMET 100

3.1 Introduction

Not only understanding the ductile fracture behavior, but also understanding the ductile-brittle transition and brittle fracture mode is important for improving the toughness of ultrahigh strength steel. Since fracture toughness tests, such as K_{Ic} or J_{Ic} tests, involve very high hydrostatic tensile stresses ahead of the crack tip, this might introduce a ductile-brittle transition near ambient temperature at the crack front. One good way for the evaluation of this ductile-brittle transition is the classical Charpy V-notch test. By conducting a low temperature CVN test, it might be possible to demonstrate the fracture behavior in a wide area of the CVN fracture surface similar to the crack tip of compact tension specimen at ambient temperature.

The high toughness and low toughness heats (Heats #1 and #2) were chosen for this test. In addition to the standard heat treatment condition, higher temperature austenitization conditions were used to study the effect of prior austenite grain size and effective grain size.

3.2 Experimental Procedure

3.2.1 Materials and heat treatment

Heat #1 (the high toughness bar) and Heat #2 (the low toghness bar) were used for this test. Three different austenitization temperatures, 1100°C, 1000°C, and 885°C (standard) were used to see the effect of prior austenite grain size and effective grain size.

After the austenitization, blanks were quenched in oil to room temperature, transferred to a liquid nitrogen bath (-197°C) and kept for 1 hour, then warmed to room temperature. Finally, they were aged at 482°C for 5 hours. Charpy V-notch specimens were then machined with L-orientation from the heat-treated blanks. Specimens for optical microscopy were prepared in the same method described in section 2.1.2.

3.2.2 X-ray analysis

Since the austenitization temperature may affect the behavior of retained and/or reverted austenite volume fraction, X-ray diffraction analysis was used to determine the volume fraction of austenite after various heat treatments. Specimens were taken in each step of heat treatment and prepared by conventional polishing. The calculation of the volume fraction of austenite was determined by the standard "direct comparison method."[58] In this study, the integrated intensities of the (200) and the (220) austenite peaks were compared with the (200) and the (211) martensite peaks. A Rigaku 300 difractometer was operated at 40kV and 200mA with Co Kα target. Since the X-ray results from the first several runs of Heat #2 didn't show any difference from those of Heat #1, only Heat #1 was examined under all heat treatment conditions.

3.2.3 Charpy impact test

The Charpy V-notch impact test was conducted in accordance with ASTM E23-96. Specimens were machined to ASTM standard single-beam type-A dimensions with L-orientation. Impact values were determined at test temperatures of 25°C, -54°C, and -

197°C. Specimens for -54°C were immersed in a controlled temperature dry ice – ethanol mixture bath, and specimens for -197°C were immersed in a liquid nitrogen bath. At least three specimens were tested at each temperature and the average of the three was used for each result. After the test, specimens were dried quickly, and fractographs just ahead of the V-notch were taken in SEM.

3.3 Experimental Results

3.3.1 Microstructure and volume fraction of austenite

The effect of austenitizing temperature on the optical microstructure is shown in Figure 3.1. Here, the microstructure of Heat #1 is shown as an example since there was no clear difference between two heats. When austenitizing temperature increases, the prior austenite grains grow, and prior austenite grain boundaries become clear and rectilinear. The prior austenite grain size after 1100°C austenitization was about 50 to 200 μm, and after 1000°C austenitization it was about 30 to 50 μm. Prior austenite grain boundary for standard 885°C austenitization is hard to measure in the optical micrograph, but with the aid of TEM micrographs, it is found to be on the order of several microns. According to Guo[14], martensite laths austenitized at 1150°C are well aligned in the packet, as opposed to the misaligned laths at the standard austenitizing treatment. Hence these higher austenitization treatments seem to be deleterious to AerMet 100's small effective grain size.

The volume fractions of austenite under several heat treatment conditions are shown in

Table 3.1 and Figure 3.2 for Heat #1. The volume fraction of austenite is around 5 to 6% in the as-quenched condition. The deep freeze treatment reduces the amount of austenite down to less than 1 %, but the volume fraction increases slightly during the aging treatment to above 1 %. The effect of the austenitization temperature was not that significant, but austenitization at 1000°C and 1100°C appears to produce slightly higher amounts of austenite than the standard heat treatment condition.

Table 3.1 Effect of austenitizing temperature on the austenite volume fraction (%)
Sample: Heat #1

	(A)1100°C	(A)1000°C	(A)885°C, Standard
Quenched	*	5.86	5.58
Deep Frozen	0.81	0.69	0.93
Aged	1.56	1.62	1.25

*: Data is not taken

3.3.2 Charpy impact energy and fractographs

The results of Charpy V-notch impact test are shown in Table 3.2 and Figure 3.3, and compared to the published data by Novotny[10]. As shown in the figure, the impact energy of Heat #1 with standard austenitization (885°C) tested at 25°C is about 40% higher than Novotny's value. On the other hand, the impact energy of Heat #2 in the same condition shows the same level as Novotny's.

Ductile-brittle transition for Heats #1 and #2 in the standard condition seems not to be finished even at -197°C. Specimens for both Heats #1 and #2 austenitized at 1000°C appear to have upper shelf energy values at 25°C, and lower shelf values at -197°C.

Table 3.2 Effect of austenitizing temperature on the temperature dependence of the Charpy V-notch impact energy

		Temp (°C)		
		-197	-54	25
Heat #1	(A)1100°C	11.9	33.8	38.6
	(A)1000°C	16.1	51.5	71.7
	(A)885°C(Std)	41.0	59.1	77.5
Heat #2	(A)1100°C	9.9	19.6	31.3
	(A)1000°C	12.9	41.0	54.4
	(A)885°C(Std)	26.8	49.4	54.2
Novotny		–	40.7	54.9

However, specimens for both Heats #1 and #2 austenitized at 1100°C appear to have lower shelf energy values at -197°C, but they don't appear to reach the upper shelf values at 25°C.

SEM fractographs of samples tested at 25°C and -197°C are shown in Figures 3.4 through 3.7. Under standard austenitization treatment condition, both Heats #1 and #2 have deep stretch zones at the crack front (Figures 3.4-a and 3.5-a, bottom of the pictures). After the stretch zone, they both fracture in the ductile fracture mode. As seen in Figures 3.4-b and 3.5-b, Heat #2 has bigger voids and larger inclusions than Heat #1. These features basically show the same tendency as shown in compact tension specimens in Chapter 1. When the austenitization temperature is increased, the fracture surface becomes bumpier, and other fracture modes are introduced. One is the cleavage fracture, and the other is intergranular separation. They are both clearly seen in Figures 3.4-e and 3.5-e. In this case, faceted cavities with cleavage fracture evidence on the bottom surface plane are surrounded by steep bevels with intergranular separation.

Elevated plateaus, each of which should be paired with a cavity, can be seen many places (an example is indicated by the arrow in Figure 3.6-c).

Fractographs obtained from specimens tested at -197°C show increased bumpy and blocky fracture surfaces (Figures 3.6 and 3.7), and they all have exhibit intergranular separation along inclined surfaces. Higher magnification shows plateau or cavity images in which both cleavage and intergranular separation are seen (except Figure 3.6-in which the inclined surface image has tiny cleavage surfaces about 5 to 10 μm imbedded in a ductile fracture surface). Figure 3.7-f shows that intergranular separation occurs by ductile fracture with dimples.

Figure 3.8 is a stereo pair of SEM fractograph prepared to show the height and depth of plateaus and cavities respectively. The images were prepared with one picture was taken with a10° tilt with respect to the other. We can see large cavities with some small plateaus in the pair, even a tiny plateaus sitting in the middle of a big cavity.

3.4 Discussion

As shown in the results, the superior toughness of Heat #1 was exhibited again in the impact energy of the standard austenitization samples, and it is confirmed that this toughness is repeatable due to the lower inclusion fraction and wider inclusion spacing. The decrease of impact energy toward lower temperature is gradual for both Heats #1 and #2, and this is attributed to their fine effective grain size. The low impact energy of the standard austenitization specimens at -197°C seems to be caused by both inter-

granular separation and cleavage fracture. Grain boundary sliding of standard austenitization specimens appears to occur in the 50 ~ 100 μm range. Since this is much larger than the prior austenite grain size, many grains must collaborate for this grain boundary sliding.

The effect of prior austenite grain size cannot be seen in tests done at the upper shelf (this is the case for austenitization at 885°C and 1000°C of Heat #2 tested at 25°C, and nearly equal in case for Heat #1 in the same condition, too). However, as temperature is decreased, the impact energies of the 1000°C austenitization samples of both Heats #1 and #2 drop more sharply and reach the lower shelf at -197°C. These sharper transitions are caused by larger effective grain sizes. The effective grain size for intergranular separation seems to be about 20 to 50 μm for 1000°C austenitization, and about 50 to 300 μm for 1100°C for both Heats #1 and #2. They both matches well with the result for prior austenite grain size obtained by optical microscopy.

Some of the cleavage facet sizes appear to be much smaller than the prior austenite grain size, but in case of large cavity or plateau, the horizontal facets seem to be just one cleavage plane, or at most two to three. This suggests Guo's work that high temperature austenitization aligns the lath and remove the disalignment of adjacent laths of AerMet 100[14].

Interestingly, cleavage fracture does not ordinarily penetrate prior austenite grain boundaries. As shown clearly in Figure 3.7-f, intergranular separation is accomplished by ductile dimple fracture. Given that the austenite volume fraction is about 1% and it

tends to sit at grain boundaries,[11] the grain boundaries may be covered by thin films of austenite, which stop the penetration of fast cleavage fracture from one grain to the other. Since the yield strength of the austenite phase is relatively weaker than that of the martensite phase they would be deformed easily if geometry allows. Therefore a fracture sequence like the following can be proposed:

1) cleavage fracture equal to the size of prior austenite grain pops first,

2) if it is surrounded by relatively high Schmidt factor bevels, transgranular shear deformation in the austenite occurs,

3) then, the blocky grain pulls out.

Hence changing the amount of retained/reverted austenite by controlling the heat treatment may change the low-temperature fracture profile and the pre-cracked compact tension specimen profile.

3.5 Summary

A comparison of the Charpy V-notch impact test with high toughness and low toughness heats of AerMet 100 with raised austenitization temperature treatments gives the results summarized as follows:

1) A very high impact energy was obtained from Heat #1 under the standard heat treatment condition. The high toughness obtained in the J-integral test in chapter 1 was repeated using a different testing method. This high toughness was also related

to the low inclusion volume fraction and wide inclusion spacing and a ductile fracture mode.

2) The ductile-brittle transition temperature, T_B, increases if the prior austenite grain size is increased by raising the austenitizing temperature.

3) Brittle fracture occurs in two modes, transgranular cleavage and intergranular separation.

4) Intergranular separation may involve the deformation of grain boundary austenite.

4. MECHANICAL PROPERTIES UNDER VARIOUS HEAT TREATMENT CONDITIONS

4.1 Introduction

The results in the previous chapter show that samples treated at a higher austenitization temperature exhibited poorer low temperature toughness, but their tensile properties have not yet been measured. Also, the standard austenitization temperature at 885°C may not be optimized; an even lower austenitization temperature might exhibit an even better combination of strength and toughness properties. To find out the optimum austenitization temperature, 1100°C and 843°C were chosen in addition to the standard austenitization temperature. Also, there was a more complete evaluation of the results of the tensile test and the J integral test for the standard heat treatment condition.

In the previous chapter, we realized that the deep freeze treatment can eliminate about 5% of retained austenite. If this austenite phase is stable and locates at the prior austenite grain boundaries, it may change the nature of grain boundary sliding and intergranular separation. Hence skipping the deep freeze treatment was also included as one of the heat treatment options.

As discussed in the section 1.4.3, the intercritical temper, which could introduce reverted austenite at the prior austenite grain boundary and lath boundary, has not been evaluated yet. This also may change the nature of grain boundary sliding and intergranular separation. But introducing reverted austenite is difficult since a slightly

higher aging temperature also results in M_2C precipitation (Figure 1.2) and could possibly lead to a strength drop. Under the assumption that a slightly higher aging temperature than the standard 482°C with a short aging time might give the best combination of toughness and strength, pre-aging treatments at 510°C for 15 minutes and 30 minutes were chosen for two of the heat treatment conditions in this chapter.

4.2 Experimental Procedure

4.2.1 Materials and heat treatment

The high toughness bar (Heat #1) and the low toughness bar (Heat #2) were chosen for this study. Six different heat treatment conditions were applied to the samples from these bars. They are tabulated in Table 4.1. Mechanical test specimen blanks were cut from the material, and then heat treated in six conditions. Tensile and compact tension (CT) specimens were then machined in the L-orientation and L-T orientation, respectively, from the heat-treated blanks.

Table 4.1 Heat treatment conditions.

Condition	Austenitization	Deep Freeze	Pre-Aging	Aging
Hich T Aust (A)	1100°C/1hr/ OQ	-197°C/1hr	None	482°C/5hr/AC
Standard (C)	885°C/1hr/ OQ	-197°C/1hr	None	482°C/5hr/AC
Low T Aust. (D)	843°C/1hr/ OQ	-197°C/1hr	None	482°C/5hr/AC
DF skipped (E)	885°C/1hr/ OQ	skipped	None	482°C/5hr/AC
Pre Age 15' (H)	885°C/1hr/ OQ	-197°C/1hr	510°C/15min/OQ+2 nd Deep Freeze	482°C/5hr/AC
Pre Age 30' (G)	885°C/1hr/ OQ	-197°C/1hr	510°C/30min/OQ+2 nd Deep Freeze	482°C/5hr/AC

*OQ: Oil Quench, AC: Air Cool

4.2.2 X-ray analysis

The amount of austenite was measured by the testing method described in section 3.2.3. Since first several runs of Heat #2 didn't show any difference from Heat #1, only Heat #1 was examined under all heat treatment conditions. The data in Chapter 3 was used for High T Aust. (A) and Std.(C) condition.

4.2.3 Mechanical properties

Tensile properties were determined using 6.35mm diameter cross section, 25.4 mm gage length round tensile specimen. The test was conducted at an initial strain rate of 5.0×10^{-4} per second at room temperature. Tensile elongation measured by a clip-on gage was digitized and stored for the entire test. The load vs. displacement data was spline-fitted to 1×10^{-8}. The data was translated into engineering strain- engineering stress curves and true strain-true stress curves. The 0.2% offset yield strength (0.2%YS), ultimate tensile strength (UTS), yield ratio, uniform elongation, total elongation, and reduction of area (RA) were measured. The true strain at UTS, the true strain at fracture,* and the true strength at fracture** were calculated from the data. The instantaneous work hardening rate (WHR) the necking criterion in equation (1.2) is reached was also calculated, and plotted against true strain on a semilogarithmic graph.

The fracture initiation toughness level was determined by the J-integral fracture toughness test method according to ASTM E-813-89, using the single specimen

* strain at fracture =ln(1/(1-RA/100)), and

** true strength at fracture = engineering strength at fracture·(1/(1-RA/100)).

unloading compliance method. Compact tension specimens without side grooves were used. K_{Ic} was evaluated by equation (1.3) by using the same values of Young's modulus and Poisson's ratio used in section 2.2. After the test, specimens were pulled apart, and their fracture surfaces near the crack front were used for SEM fractographs.

4.3 Experimental Results

4.3.1 Volume fraction of austenite

The effect of austenitizing temperature and of skipping the deep freeze on the fraction of austenite is shown in Table 4.2 and Figure 4.1. In the as-quenched condition, the low T austenitization (843°C) has a smaller amount of retained austenite. After the deep freeze, the low T austenitization has a higher volume of retained austenite. After aging, the standard condition has the lowest amount, high T and low T have slightly more, and the "DF skipped" has the highest volume, almost the same as in the as-quenched condition.

Table 4.3 and Figure 4.2 show the effect of pre-aging on the volume fraction of austenite. Until the 2nd deep freeze, the volume of austenite doesn't seem to be affected by pre-aging. But after the final aging condition, pre-aged samples appear to have slightly higher volume of austenite than standard heat treatment condition.

Table 4.2 Effect of austenitizing temperature and the deep freeze on the fraction of austenite (%)

	(A)1100°C	(A)885°C, Standard	(A)843°C	(A)885°C, DF skipped
Quenched	*	5.58	3.86	5.58
Deep Frozen	0.81	0.93	1.34	**
Aged	1.56	1.25	1.71	5.66

*: Data is not taken
**: Data is not available

Table 4.3 Effect of pre-aging condition on the fraction of austenite (%)

	Standard	Pre Aging: 15'	Pre Aging: 30'
Quenched	5.58	<-	<-
Deep frozen	0.93	<-	<-
Pre-aged	**	*	1.00
Deep frozen	**	0.96	1.14
Aged	1.25	1.79	1.84

*: Data is not taken
**: Data is not available

4.3.2 Tensile properties

The results of the tensile property measurements are shown in Table 4.4 and Figures 4.3 through 4.10. Table 4.4 also shows the specification for aerospace use of AerMet 100 (AMS 6532) for comparison. All values satisfy the minimum values of the specification except for the 0.2%YS of the DF skipped samples from both heats. Also, in general the total elongation and RA of Heat #1 always surpasses those of Heat #2 if same heat treatment condition is compared, although the uniform elongation is not affected (Figure 4.4). Furthermore, the work hardening characteristics of both heats up to necking are almost identical. These last two facts suggest us that higher inclusion

Table 4.4 Effect of heat treatment conditions on the mechanical properties.

Heat	Heat Treatment	Tensile Properties								Fracture Toughness	
		Engineering stress-strain relationship					True stress-strain relationship				
		0.2%YS (MPa)	UTS (MPa)	Uniform Elon.(%)	Total Elon.(%)	R.A. (%)	True strain at UTS (-)	Strain at Fracture (-)	True strength at fracture (MPa)	J_{IC} (kJ/m^2)	K_{IC} (MPa$\sqrt{m}$)
#1	High T Aust (A)	1798	2036	2.78	15.0	64.6	0.0300	1.038	3401	100.7	145.8
	Standard (C)	1852	2024	1.66	13.5	67.4	0.0252	1.121	3399	150.5	178.2
	Low T Aust. (D)	1712	1960	1.85	12.6	59.6	0.0268	0.906	2980	81.7	131.3
	DF skipped (E)	1583*	2040	3.09	14.7	66.5	0.0396	1.094	3388	119.0	158.5
	Pre Age 15' (H)	1867	1978	1.46	13.3	66.5	0.0227	1.094	3257	161.7	184.8
	Pre Age 30' (G)	1807	1951	1.68	14.0	68.3	0.0252	1.149	3278	180.0	194.9
#2	High T Aust (A)	1813	2025	2.01	11.7	50.9	0.0295	0.711	2916	71.4	122.8
	Standard (C)	1855	2036	1.47	12.7	62.6	0.0235	0.983	3243	97.2	143.3
	Low T Aust. (D)	1855	1980	1.33	11.5	57.0	0.0222	0.844	2965	55.7	108.4*
	DF skipped(E)	1615*	2039	2.70	14.1	62.3	0.0358	0.976	3241	65.5	117.6
	Pre Age 15' (H)	1842	2000	1.60	13.1	62.6	0.0247	0.983	3222	104.3	148.4
	Pre Age 30' (G)	1826	1971	1.43	12.9	63.5	0.0247	1.008	3085	89.0	137.1
AMS 6532		≥1620	≥1931		≥10	≥55					≥110

Marked "*" does not satisfy AMS 6532 specification.

volume fraction deteriorates the ductility of the local deformation occuring from necking to final fracture, but it doesn't play any role in the early stage of the tensile properties.

From Figure 4.11, the values of the true strain at fracture of Heat #1 in conditions C, E, H, and G are about 10% higher than those of Heat #2, but not the high and low temperature austenitization conditions (A, D). The true fracture strengths of Heat#1 in each of these conditions are also higher than the corresponding conditions of Heat #2. The low T austenitization (D) decreases the strain and strength of both heats at the same time. The effect of the high T austenitization, condition (A), specimens is different for each heat. That condition for Heat #1 has high strain and high strength close to the standard condition. On the other hand, that condition for Heat #2 has the lowest strain and stress combination.

The following effects are compared with the standard heat treatment condition.

1) Effect of austenitization temperature: Figures 4.3 through 4.7

High T austenitization decreases the 0.2%YS and the yield ratio, but doesn't seem to affect the UTS. On the other hand, low T austenitization decreases the UTS, but has no clear effect on the 0.2%YS. High T austenitization doesn't affect on the total elongation and the RA of Heat #1 very much, but it deteriorates the total elongation and the RA of Heat #2. The WHR of high T austenitization samples has clearly higher value near the necking region, and higher uniform elongation, but the WHR and the uniform elongation of low T austenitization doesn't change much.

2) Effect of skipping the "deep freeze" treatment: Figures 4.3, 4.4, 4.6, and 4.8

Skipping the deep freeze reduces the 0.2%YS and yield ratio drastically, but it doesn't decrease the UTS at all. It also increases the uniform elongation and the total elongation while leaving the RA the same. Better elongation comes with the unique behavior of WHR. Skipping the deep freeze reduces the negative slope of WHR against true strain, and as a result, it increases the uniform elongation more than 1%. This corresponds to about 85% increase of uniform elongation.

3) Effect of pre-aging: Figures 4.3, 4.4, 4.6, 4.9, and 4.10

Pre-aging appears to decrease both the 0.2%YS and the UTS, and the longer holding time decreases it more. 15 minutes of pre-aging doesn't seem to change the elongation and RA, but 30 minutes of pre-aging clearly increases the RA. Pre-aging doesn't appear to affect the plot of WHR against strain. We can assume from these facts (lower tensile strengths and same WHR against strain plot) that pre-aging only shifts the microyielding point without changing any WHR characteristics. By comparing the WHR against true stress, this is confirmed (see appendix Figures A8 and A12).

4.3.3 Fracture toughness

The load-unload process of the J-integral test was manually controlled. To satisfy ASTM E813-89 by a single-specimen technique, compliances for early stage blunting should be measured evenly with enough data points to get an accurate power law fitting curve and get the J_Q to be a valid J_{Ic}. If the crack in the specimen propagates in a

slow stable manner, as in the example in Figure 4.12-a, this will lead to the J-da curve with evenly spaced data points. But if the specimen cannot hold the high elastic energy in the body, and releases it in a fast unstable crack propagation, a big jump will appear in the load –vertical displacement curve (marked by the arrow in Figure 4.12-b). This then leads to a J-da curve with unevenly spaced data points and with a gap. J-da curves can be analyzed this way if the test material exhibits an unstable fast fracture mode. Also, wider spacing between adjacent points in the J-da curve suggests that more elastic energy is released at a time with larger crack extension.

All the J_Q values in this study were valid, and are expressed as J_{Ic}. The measured J_{Ic} values and calculated K_{Ic} values (by equation 1.3) are tabulated in Table 4.4 along with the tensile data and AMS 6532. The calculated K_{Ic} values are graphed in Figure 4.13. J-da curves are given in Figures 4.14 to 4.16. Along with the J-da curve, the blunting line, 0.15mm exclusion line, 0.2 mm offset line (J_Q is the junction between this line and the J-da curve), and 1.50 mm exclusion line are also drawn. SEM fractographs at the crack front are shown in Figures 16 and 17. The direction of crack propagation is from the bottom to the top of the picture, and roughly the first 0.5 to 0.6 mm of crack extension at the center of the CT specimen can be seen from the low magnification fractographs.

1) Re-evaluation of the standard heat treatment condition: Figures 4.13, 4.14, 4.17-c, d, and 4.18-c, d

The standard heat treatment condition of Heat #1 showed very high toughness values

again, though the standard condition of Heat #2 showed higher values than the study in Chapter 1. The J-da curve of Heat #1 is different from that of Heat #2 because its crack propagates in fast unstable manner though its elastic energy level is very high. On the other hand, the J-da curve of Heat #2 blunts at a much lower energy level though it shows slow stable crack propagation. From the fractographs, Heat #1 clearly exhibits deeper voids than Heat #2 near the crack front with smaller primary void nucleating particles. Not only this is distinguishable, but also Heat #1 shows features such as plateaus and cavities, suggesting a more brittle fracture mode at the very crack front and a relatively shallow microvoid coalescence region after the deep microvoid region. Even in the flat region one could describe the fracture surface as having micro tears. To the contrary, the fracture surface of Heat #2 has a uniform fracture mode, microvoid coalescence.

The following effects are always compared with the standard heat treatment condition.

2) Effect of austenitization temperature: Figures 4.13, 4.14, 4.17-a~f, and 4.18-a~f

Changing the austenitization temperature in either direction from the standard results in a drop in fracture toughness. Hence, the optimum austenitization temperature is 885°C. From Figure 4.14, the crack propagation of high T austenitization of Heats #1 and #2 both becomes more unstable and greater crack extension occurs during fast fracture. Heat #1 exhibits a brittle cleavage surface with large plateaus, but the fractograph of Heat #2 shows both ductile and brittle fracture modes. There is also evidence of grain boundary sliding in Figure 4.18-a (marked by the arrow).

The behavior of low T austenitization for Heat #1 and #2 also differ. Crack extension of Heat #1 is propagated in a fast unstable manner, but that of Heat #2 is not. By comparing the fractographs in Figures 4.17-c and 16-e, both the sizes of plateaus at the crack front and microvoids in the low T aust. of Heat#1 shrinks. Meanwhile, the low T austenitization specimen of Heat #2 shows ductile mode microvoid coalescence over the entire surface similar to the standard condition of Heat#2.

3) Effect of skipping the deep freeze treatment: Figure 4.13, 4.15, c, d, g, and h of 4.17 and 4.18

Skipping the deep freeze decreases the toughness, and doesn't seem to change the tendency toward fast unstable crack propagation, in fact it makes it worse. The "DF skipped" specimen of Heat #1 has more plateaus and cavities than the specimen in the standard condition. The "DF skipped" condition of Heat #2 exhibits some plateaus and cavities but not too many. Both heats exhibit evidence of both brittle and ductile fracture modes.

4) Effect of pre-aging: Figure 4.13, 4.16, c, d, and i ~ m of 4.17 and 4.18

The fracture behavior of pre-aged samples of Heats #1 and #2 shows a different trend. In the case of Heat #1, the fracture toughness monotonically increases with the pre-aging time, reaching 200 MPa$\sqrt{m}$. But in case of Heat #2, the toughness only slightly increases for the 15 minute pre-aged specimen, then drops if it is pre-aged for 30 minutes. Although the J-da curves change little among all conditions of Heat #2, the change in those of Heat #1 is drastic. Pre-aging raises up the J-da curve in more stable

manner for Heat #1. From the fractographs of Heat #2, all samples have similar fracture modes, and again they all have microvoid coalescence over most of the fracture surface. However, in the case of Heat #1, the number of plateaus and cavities increases with pre-aging time. The deep microvoid region which precedes the crack front plateaus in the standard heat treatment condition (Figure 4.17-c) disappears, and is replaced by a mixture of plateaus and cavities and deep microvoids throughout. In both pre-aged and standard treatment samples, the plateaus have a monoclinic shape with its top plane parallel to the pre-crack plane and its longest length perpendicular to the direction of crack propagation. Also the sides of the plateaus are inclined toward the crack front.

4.4 Discussion

4.4.1 Effect of inclusion content under the standard heat treatment condition

As shown in Chapter 2, basically, lower inclusion volume and wider inclusion spacing can explain the difference in the toughness values between the two heats. But further differences can be seen. The fracture surface of the high inclusion volume bar (Heat #2) is covered by ductile microvoid coalescence. But, once the inclusion volume decreases to the level of Heat #1, it not only forms deeper voids as shown in Chapter 2, but it also forms a mixture of transgranular cleavage and intergranular separation at the initial propagation of the crack front even in the ambient temperature J-integral test. That means that severe constraint at the crack front raises the yield stress up to the level of cleavage fracture strength. This is exactly the ductile-brittle transition point. So

the study in Chapter 3 can now be applied to this heat treatment study.

Intergranular separation is usually classified as an undesirable, brittle fracture mode, but in this case it might be helpful for improving the toughness. If a stable austenite phase (which is ductile and has good workability) covers the prior austenite grain boundaries in the form of a thin film, then this can act to increase the toughness by allowing plastic deformation during grain sliding. As shown in the Figure 4.17-c, standard condition of Heat #1 has plateaus at the crack front. Since this is the grain boundary sliding, this does not build up the stress in the grain very much, is helpful for blunting, and could decrease the stress intensity near the crack tip. However, if strain energy goes up further, then there will no longer be grain boundary sliding at the crack front and the subsequent deep microvoids region cannot hold such a large strain energy, so fast unstable fracture occurs. To the contrary, standard Heat #2 doesn't have clear plateaus at the crack front, indicating that there is little or no sliding along the grain boundaries. Assuming all other microstructural parameters are the same except for the inclusion volume fraction, this higher inclusion volume fraction causes shear localization and subsequent microvoid nucleation and growth at a lower strain energy level. This is the reason why plateaus cannot be seen clearly in Heat #2.

4.4.2 Effect of austenitization temperature

1) Effect of high temperature austenitization:

The effect of high temperature austenitization on the toughness-strength relationship is shown in Figure 4.19. High austenitization temperature slightly decreases the 0.2%YS

but doesn't change the UTS very much. However, it decreases the toughness significantly, especially for low inclusion fraction and subsequent high toughness bar (Heat #1). As shown in the Figures 4.17-a and 4.18-a, high T austenitized Heat #1 shows transgranular cleavage more than that of Heat #2. Hence toughness drop for Heat #1 is larger than that for Heat #2.

2) Effect of low temperature austenitization:

Low T austenitization decreases the UTS for both heats (Figure 4.20). Low T austenitized Heat #1 appears to have relatively flat unstable fast fracture surface, and doesn't have deeper voids nor larger plateaus at the crack front unlike those in the standard Heat #1. Since the fracture pattern still has the feature of microvoids, this is classified as microvoid coalescence though the microvoids tend to be shallow. On the other hand, low T austenitized Heat #2 shows a similar fractograph to the standard Heat #2.

From these results, low temperature austenitization may increase the number of undissolved carbides, decrease the inherent strength, and have more void nucleation sites. The low strain and low strength at the tensile fracture in Figure 4.11 also support this idea, since increased volume of undissolved carbides not only creates void nucleation sites but also reduces the amount of age-hardenable precipitation phases.

4.4.3 Effect of skipping the deep freeze

The effect of skipping the deep freeze on the toughness-strength relationship is shown in Figure 4.21. Even though they have lower yield strength, higher work hardening

rate, and higher ultimate strength, their fracture toughness values are much lower than the standard condition.

If WHR is plotted not against strain but against stress, the early stage of work hardening behavior is understood more easily. As shown in Figure 4.22, the standard heat treatment condition shows linear elastic behavior until about 1100MPa for both Heats #1 and #2. Then both heats yield and the elastic-plastic transition occurs rapidly. On the other hand, if the deep freeze skipped, both heats yield on a micro-scale around 300 MPa, then a relatively mild negative slope goes up to about 1100MPa, which is the same deflection point in stress as in the standard condition. After this second deflection point, skipping DF condition makes its negative slope slightly steeper, but still mild in comparison to that of standard condition, then finally they cross over above 2000MPa. This early yielding should be caused by the retained austenite.

Considering the result that the DF-skipped treatment has a high volume of retained austenite, these phenomena could be explained as follows. Retained austenite sits mainly at the prior austenite grain boundary, and is at least stable during the early stage of deformation in the tensile test. But a high hydrostatic tensile stress state triggers the stress induced martensitic transformation. Since fresh martensite is very brittle, it shows poor fracture behavior in fracture toughness test although plateaus and cavities are seen on their fracture surfaces. The stability and location of the retained austenite must be examined carefully to support this hypothesis.

4.4.4 Effect of pre-aging

The effect of pre-aging conditions on the toughness-strength relationship is shown in Figure 4.23. The behavior of the two heats is completely different. Pre-aging increases the toughness of high toughness bar (Heat #1) though there is a slight decrease in tensile strength. On the contrary, the toughness of Heat #2 slightly increases for the 15-minute holding time, then toughness decreases for 30-minute holding time, while strength simply decreases with holding time.

The tendency of toughness to increase in Heat #1 could be explained by the relative ease of grain boundary sliding. As intended in this experiment, the austenite volume fraction appears to be increased by pre-aged condition (Figure 4.2). If this excess austenite is stable, forms on the prior austenite grain boundary and thickens the austenite film, this makes the grain boundary sliding easier. The effect of pre-aging on bulk strength is not clear at this moment, but this grain boundary austenite will blunt cracks with less damage to the inside of grains. Hence a rising J-da curve with stable slow crack extension is obtained with both plateaus/cavities and ductile microvoids. On the other hand, Heat #2 cannot use this blunting technique. If the body has a large amount of inclusions, shear localization and early microvoid nucleation and growth always comes first, and never reach the stress level to create plateaus/cavities, i.e. transgranular cleavage and prior austenite grain boundary sliding.

4.4.5 Shape of plateaus in compact tension specimen fracture surfaces

As seen in low magnification image in Figure 4.17, most of the time plateaus have a

monoclinic shape with its top plane parallel to the pre-crack plane and its longest length perpendicular to the direction of crack propagation. Also the sides of the plateaus are inclined toward the crack front. Since the maximum plastic strain occurs at 45° from the crack plane at the blunted crack tip in mode I loading[59], once cleavage occurs ahead of the crack tip on the order of prior austenite grain size, grain boundary austenite at far side and near side from the crack tip will be sheared along maximum plastic strain direction. Since there is no strain acting on the plane perpendicular to the crack front, if adjacent grains along crack front have similar grain orientation, they can all cleave at one time, and be pulled together.

4.4.6 Fracture patterns

Assuming the existence of grain boundary austenite, all fracture patterns are summarized below and a cartoon depiction of each is given in Figure 4.24.

Case 1: The fracture mechanism of Heat #2 is basically just microvoid coalescence. If a body has high volume and narrowly spaced inclusion in it, relatively low hydrostatic tensile stress nucleates voids from large inclusions (σ_{void}), the subsequent void growth causes the shear localization, and microvoid coalescence occurs in a stable manner (all conditions except skipping DF and high T aust. in Heat #2, but only for low T aust. in Heat #1).

Case 2: If a body containing a sharp crack contains a significantly lower inclusion count than the above case, the critical hydrostatic tensile stress to nucleate a void from the particle will go up. If the body was kept strained by remote stress, it will nucleate

the void with a higher hydrostatic tensile stress ahead of the crack tip, and work harden the bulk material (the tensile stress will be highest at a distance from the crack tip about twice as large as crack tip opening displacement[59]). Eventually it will attain the critical stress which initiates the cleavage fracture ($\sigma_{cleavage}$). However, if there is enough work-hardenable, stable austenite with low yield strength (σ_{GB}) at the prior austenite grain boundaries, and if geometry allows this austenite to be sheared, cleavage fracture cannot penetrate to the next grain, and the shear stress pull the grain out. Then plateau and corresponding cavity is formed with microvoids ahead of this grain boundary sliding area (standard, and pre-aged 15min. and 30min. in Heat #1).

Case 3: If the effective prior austenite grain size becomes larger, and $\sigma_{cleavage}$ becomes smaller than σ_{void}, then only a mixture of transgranular cleavage and intergranular separation is seen (high T aust. in Heats #1 and #2)

Case 4: If the grain boundary austenite is unstable, the crack propagation will form a plateau and cavity combination, but at the same time it creates brittle fresh martensite. This fresh martensite does not blunt the sharp crack, but instead initiates brittle fracture, hence the toughness will not be high (skipping DF in Heats #1 and #2)

4.4.7 Validity of the ductile fracture model

As discussed in section 1.4.2, ductile fracture models generally have the form of equation 1.4. Hence all experimental data obtained in this chapter were examined by

J_{Ic} vs. $\varepsilon_f \sigma_0$ plot.

First, the values of the strain at UTS and the 0.2%YS were substituted for ε_f and σ_0, respectively in equation 1.4. Figure 4.25 shows that using these values does not result in a single proportionality constant applicable to all samples in all of the above cases. Each case needs to be considered separately.

As categorized in the above section, the pure ductile fracture condition (case 1) forms a group. If it is taken as nominally following equation 1.4 using the values of the strain at UTS and the 0.2%YS for ε_f and σ_0, then one can compare the other cases to see how the different fracture modes affect the model. In case 2, since they involve blunting by grain boundary sliding, the samples reach higher fracture toughness values than would be predicted by equation 1.4. In case 3, they deviate to the right of case 1. Since the fracture surfaces in case 3 contain more areas of brittle fracture, the high elongation and high strength until necking cannot contribute to the J_{Ic}. In the case 4 conditions, the yield strength of the retained austenite might be overestimated as shown in Figure 4.24. The strain at UTS also overestimates the critical strain at the crack tip due to the high hydrostatic tensile stress state. Hence these values also deviate to the right from case 1.

Since there is a highly triaxial stress state at fracture, a more appropriate choice for the flow stress and failure strain would be the strain and stress at fracture in the tensile test. To test this idea, J_{Ic} vs. $\varepsilon_f \sigma_0$ was re-plotted by using strain and strength at the tensile fracture for ε_f and σ_0, respectively (Figure 4.26). In this plot, all categories except for

those samples in case 2 show rough proportionality. However, case 2 obviously has higher J_{Ic} values from other three categories. As discussed in sections 4.4.5 and 4.4.7, the higher J_{Ic} values are attributed to the blunting mechanism by grain boundary sliding. Deviation from the other three categories becomes larger when more plateaus and cavities are formed on surface at the crack front by grain boundary sliding (Figure 4.18-c, i, k). This grain boundary sliding is only available at the highest combination of ε_f and σ_f so that the σ_{void} surpasses the $\sigma_{cleavage}$.

By comparing Figures 4.25 and 4.26, it is evident that the fracture toughness J_{Ic} is estimated more accurately from the tensile fracture condition than the necking condition. That means the final fracture process in the neck in tensile test simulates the plastic deformation behavior near the crack front in CT specimen to certain degree. But the tensile fracture cannot predict the blunting by prior austenite grain boundary sliding, which is what increases the J_{Ic} values significantly for the samples in case 2. In the case of the CT specimen geometry, blunting by grain boundary sliding reduces the stress intensity at the crack front and allows sampling of a larger volume of material, whereas in the tensile test geometry, grain boundary sliding will not have that effect. Rather it decreases the fracture strength.

Here I propose the direction of improving the toughness of AerMet 100.

i) reduction of non-metallic inclusion volume

ii) reduction of prior austenite grain size

iii) inclusion of adequate amount of stable austenite at the prior austenite grain boundary

iv) control the amount of undissolved carbide

v) further addition of precipitation hardening elements

All of those are the traditional ways of obtaining optimum toughness/strength relationship. But this is the way this ultrahigh strength steel can be improved. Approach i) needs state of the art level melting skills and equipment, but approach ii) is very popular in Korea and Japan these days. At least if approach ii) is achieved to some degree, optimization of approach iii) and iv) may help the further improvement of toughness. If there is still a room for the increase of strength, approach v) should be explored to invent a new ultrahigh strength steel.

4.5 Summary

The effects of austenitization temperature, skipping the deep freeze, and pre-aging were examined by using high toughness bar (Heat #1) and low toughness bar (Heat #2). The results are summarized as follows:

1) Inclusion volume doesn't affect the early stage of tensile properties in the level of this study.

2) Any heat treatment conditions tested in this study could not improve the toughness of the low toughness bar (Heat #2). The critical void nucleating stress with high

inclusion volume under high hydrostatic tensile stress state in CT specimen was always lower or equal to the other brittle fracture modes.

3) Once the inclusion volume decreases to the level of Heat #1and the elastic energy near the crack front goes up further, it not only forms deeper voids, as shown in Chapter 2, but also forms mixture of transgranular cleavage and intergranular separation in the ambient temperature J-integral test. Thus the mixture of ductile and brittle fracture modes comes up at the same time by the geometrical constraint.

4) Grain boundary sliding is associated with stable austenite along the grain boundaries. This is helpful for blunting at the crack tip and increases the J_{Ic} value, though this may reduce the tensile strength. Holding at slightly higher temperature (510°C) than standard aging temperature (482°C) in a short time is useful for improving this blunting mechanism.

5) Retained austenite obtained by skipping the deep freeze not only decreases the yield strength, but also decreases the toughness.

6) The optimum austenitization temperature appears to be near the standard austenitization temperature (885°C).

7) Further improving the toughness requires the combination of: i) reduction of inclusion volume fraction, ii) reduction of prior austenite grain size, iii) inclusion of adequate amount of stable austenite at prior austenite grain boundary, iv) control of the amount of undissolved carbides, and v) further addition of precipitation

hardening elements.

5. CONCLUSIONS

This dissertation presented an examination of a Fe/Co/Ni/Cr/Mo/C alloy steel, AerMet 100, focusing on its toughening mechanisms. The possibility of further improving the strength/toughness combination of this already remarkable steel was explored. The results enumerated in the previous chapters lead to the following conclusions:

1) The fracture toughness at ambient temperature of AerMet 100 is very sensitive to the inclusion volume fraction and the subsequent inclusion spacing. Smaller inclusion volume fraction and wider inclusion spacing create deeper voids, hold higher elastic energy, and improve the toughness.

2) Fracture toughness, J_{Ic}, is linearly related to the inclusion spacing. Further improvement of toughness in K_{Ic} only by the increase of the inclusion spacing is difficult since K_{Ic} is proportional to square root of J_{Ic}.

3) The particles nucleating the primary voids are mainly oxysulfides or oxyphosphates of rare earth metals. Undissolved carbides might also nucleate primary voids.

4) The high fracture toughness is based on not only low inclusion content but also on fine prior austenite grain size. The fine prior austenite grain size decreases the ductile-brittle transition temperature in the Charpy V-notch test, and suppresses the fast unstable crack propagation by cleavage in the J-integral test.

5) When inclusion volume decreases to a very low level, all three fracture modes (ductile microvoid coalescence, brittle transgranular cleavage, and intergranular

separation) can be seen at the crack front of a compact tension specimen in an ambient temperature J-integral test due to the high triaxial tensile stress state at the crack front.

6) Grain boundary sliding is helpful for improving toughness by its contribution to crack tip blunting. This is associated with the stable austenite forming at the primary austenite grain boundary. Intercritical temper prior to the final aging treatment increases the amount of stable austenite.

7) The standard model relating J_{Ic} and tensile test results is significantly improved by using the strain and strength at tensile fracture for failure strain and flow stress respectively instead of the strain at UTS and the 0.2%YS.

Finally, this dissertation proposes the following directions to be used in combination towards improving the toughness of AerMet 100:

i) reduction of non-metallic inclusion volume

ii) reduction of prior austenite grain size

iii) inclusion of an adequate amount of stable austenite at the prior austenite grain boundaries

iv) control of the amount of undissolved carbide

v) further addition of precipitation hardening elements

All of these are traditional ways of improving the toughness/strength relationship. This

dissertation has shown the fundamental underlying mechanisms by which this combination of methods will succeed. Each of these objectives is achievable. Approach i) needs state of the art level melting skills and equipment, but approach ii) is already very popular in Korea and Japan these days. At least if approach ii) is achieved to some degree, optimization of approach iii) and iv) may help the further improvement of toughness. If there is still a room for the increase of strength, approach v) should be explored to invent a new ultrahigh strength steel. Hopefully this fundamental understanding of the strengthening and toughening mechanisms will be applied to make the next generation ultrahigh strength steels.

REFERENCES

1. Metals Handbook 10th ed., 1990, pp. 430 to 447

2. W.M. Garrison, Jr., Journal of Metals, May, 1990, pp. 20 to 26

3. G.B. Olson, "Overview: Science of Steel," Innovations in Ultrahigh-strength steel Technology, ed. by G.B. Olson, M. Azrin, and E.S. Wright, Proceedings of the 34th Sagamore Army Materials Research Conference, 1987, p.3-66

4. G.R. Speich: " Innovations in Ultrahigh-strength steel Technology, ed. by G.B. Olson, M. Azrin, and E.S. Wright, Proceedings of the 34th Sagamore Army Materials Research Conference, 1987, p.89-111

5. Alloy Data of AerMet 100, Alloy Steels 6, Carpenter Technology Corporation, 1992

6. R.M Hemphill and D.E. Wert, "High Strength, High Fracture Toughness Structural Alloy", United States Patent No. 5,087,415, Feb. 11, 1992, 6pp

7. R.M Hemphill, D.E. Wert, P.M Novotny, and M.L. Schmidt, "High Strength, High Fracture Toughness Structural Alloy", United States Patent No. 5,268,044, Dec. 7, 1993, 6pp

8. Aerospace Materials Specification 6532

9. M. Schmidt and R. Hemphill: Scripta Metall. Mater., 1991, vol. 25, pp.239-60

10. P.M. Novotny, G.R. Speich Symposium Proc., Fundamentals of Aging and Tempering in Bainitic and Martensitic Steel Products, 34th Mechanical Working and Steel processing Conference, Iron and Steel Society, 1992, pp. 215 to 236

11. R. Ayer and P. Machmeier: Metall. Trans. A, 1993, vol. 24A, pp.1943-55

12. R. Ayer and P. Machmeier: Metall. Trans. A, 1996, vol. 27A, pp.2510-17

13. Z.Guo, K. Sato, T.K.Lee, and J.W. Morris, Jr., Ultrafine Grain 2000, Proceedings of TMS Conference on Ultrafine Grain Size, 2000, pp.51 to 62

14. Z. Guo, Ph.D. Dissertation, University of California, Berkeley, 2001

15. C.H. Yoo, H.M. Lee, J.W. Chan, and J.W. Morris, Jr., Metallurgical and Materials Transactions, vol.27A, 1996, p.3466

16. M. F. Carlson, B.V. Narasimha Rao and G. Thomas: Metallurgical Transactions, vol. 10A, 1979, p.1273

17. M. Sarikaya: Ph. D. Thesis, University of California, Berkeley, 1982

18. N.S. Stolofff, in Fracture, H. Liebowits, ed., Avademic Press, N.Y., 1969, vol. 6, p.7

19. R.A. Grange, Trans. ASM, vol.59, 1966, p.26

20. J.D. Bolton, E.R. Petty and G.B. Allen, Metallurgical Transactions, vol.2A, 1971, p.2915

21. M. Ogasawara, M. Iino and H. Mimura, Trans. JIM, vol. 13, 1972, p.6

22. J.I. Kim, C.K. Syn and J.W. Morris, Jr.: Metallurgical Transactions, vol 14A, 1983, p.93

23. J.W. Morris, Jr., J.I. Kim and C.K. Syn, in Advances in Metal Processing, J. Burke, R. Mehrabian and V. Weiss, eds., Plenum Press, New York, 1981, p.173

24. H.J. Kim, Y.H Ki, and J.W. Morris, Jr.: ISIJ International, vol. 38, 1998, p.1277

25. J.W. Morris, Jr., Adv. Cryogenic Eng., 32, 1 (1985)

26. B.C. Woodfine, Journal of the Steel Institute, vol. 173, 1953, p. 229

27. L.L. Eyre, B.C. Edwards, and J.M. Titchmarsh: Advances in the Physical Metallurgy and Applications of Steels, Metals Society, University of Liverpool, London, September, 1981, p.246

28. J. Yu and C.J. McMahon, Jr., Metallurgical Transactions, vol. 11A, 1980, p.277

29. S. K. Hwang: Ph. D. Thesis, University of California, Berkeley, 1977

30. S. K. Hwang and J. W. Morris, Jr.: Metallurgical Transactions, vol. 10A, p.545

31. S. K. Hwang and J.W. Morris, Jr.: Metallurgical Transactions, vol. 11A, 1980, p.1197

32. H. J. Lee: Ph. D. Thesis, University of California, Berkeley, 1982

33. C.K. Syn, B. Fults and J.W. Morris, Jr., Metallurgical Transactions, vol. 12A, 1978, p.1635

34. G. Thomas, Metallurgical Transactions, vol. 9A, 1978, .439

35. R. Ramesh, N.J. Kim, and G. Thomas: Metallurgical Transactions, vol. 21A, 1990, p. 683

36. T.B. Cox and J.R. Low, Met. Trans. vol. 5A, 1974, pp1457-

37. J.F. Knott, "Ductility, Toughness and Formability," Paper No.8 in Proceedings of Conference on Inclusions and their Effects on Steel Properties, Univ. of Leeds, 1974. Published by British Steel Corporation.

38. G.T. Hahn and A.R. Rosenfeld, ASTM STP 432, American Society for Testing and Materials, Philadelphia, 1968, p.5

39. P.F. Thomason, Int. J. Fracture Mech., vol. 7, 1971, p.409

40. G.G. Garrett and J.F. Knott, Met. Trans., vol. 9A, 1978, p.1187

41. J.W. Morris, Jr., J. Glazer, and J.W. Chan, Proc. of International Cryogenic Materials Conference, 1989

42. G.T. Hahn and A.R. Rosenfield, ASTM STP 432, American Society for Testing and Materials, Philadelphia, 1968, p.5

43. P.F. Thomason, International Journal of Fracture Mechanics, vol.7, 1971, p.409

44. G.G. Garrett and J.F. Knott: Metallurgical Transactions, vol.9A, 1978, p.1187

45. R.O. Ritchie and A.W. Thompson: Metallurgical Transactions, vol. 16A, 1985, p.233

46. J.R. Rice: "Fracture: An Advanced Treatise," H. Liebowitz, ed., Academic Press, New York, 1968, pp191-311

47. H.Nakajima, et al., Adv. Cryo. Eng., vol.32, p.347, 1986

48. W.M. Garrison, Jr. and N.R. Moody: Metallurgical Transactions A, vol. 18A, 1987, pp1257-1263

49. K.J. Handerhan, W.M. Garrison, Jr. ad N.R. Moody: Metallurgical Transactions A, vol. 20A, 1989, pp105 -123

50. W.M. Garrison, Jr. and K.J. Handerhan: Innovation in Ultrahigh-strength steel technology, ed. by G.B. Olsen et al., 34th Sagamore Conference, 1987, p443-466

51. J.W. Bray, K.J. Handerhan, W.M. Garrison, Jr., and A.W. Thompson: Metallurgical Transactions A, vol.23A, 1992, pp485-496

52. J.R. Rice and M.A. Johnson: Inelastic behavior of solids, M.F. Kanninen, W.G. Adler, A.R. Rosenfield, and R.I. Jaffee, eds., McGraw-Hill, New York, 1970, 641-72

53. R.M. McMeeking: Journal of Mechanical Physics of Solids, 1977, vol.25, pp357-81

54. R.M. McMeeking: Journal of Engineering Materials and Technology, Transactions of AIME, Series H, 1977, vol.99, 290-297

55. M.F. Ashby and R. Ebeling: Transactions of MIME, 1966, vol.236, p1396-1404

56. E.E. Underwood: "Stereology and Quantitative Metallography, ASTM STP 504, 1972, pp3-38

57. C.F. Shih: Journal of Mechanical Physics of Solids, 1981, vol.29, p305-30

58. B.D. Cullity: Elements of X-ray Diffraction, Addison-Wesley Publishing Company, Reading, MA, 1978, pp.411-415

59. T.L. Anderson: Fracture mechanics (2nd ed.), CRC Press, 1995, pp.265-305

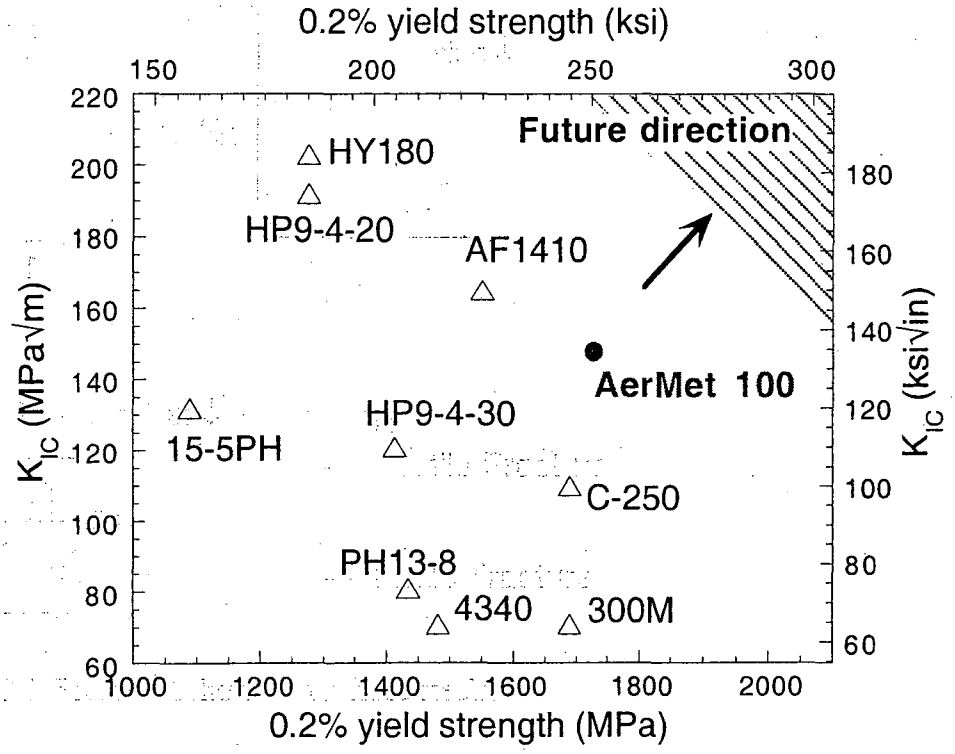

Figure 1.1 Relationship between fracture toughness, K_{Ic}, and 0.2% yield strength among several ultrahigh strength steels.

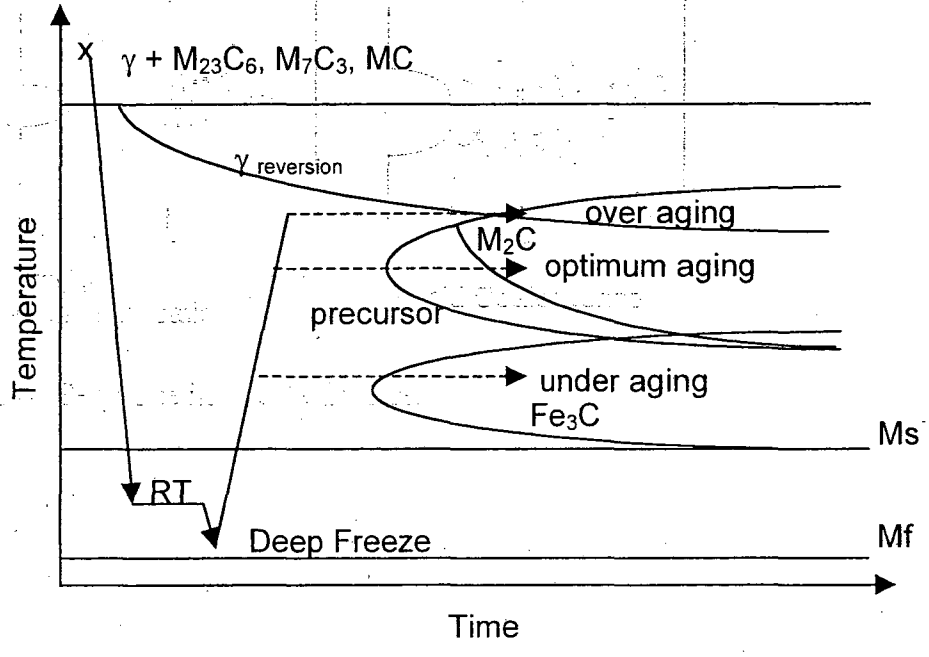

Figure 1.2 Schematic TTT diagram of AerMet 100.

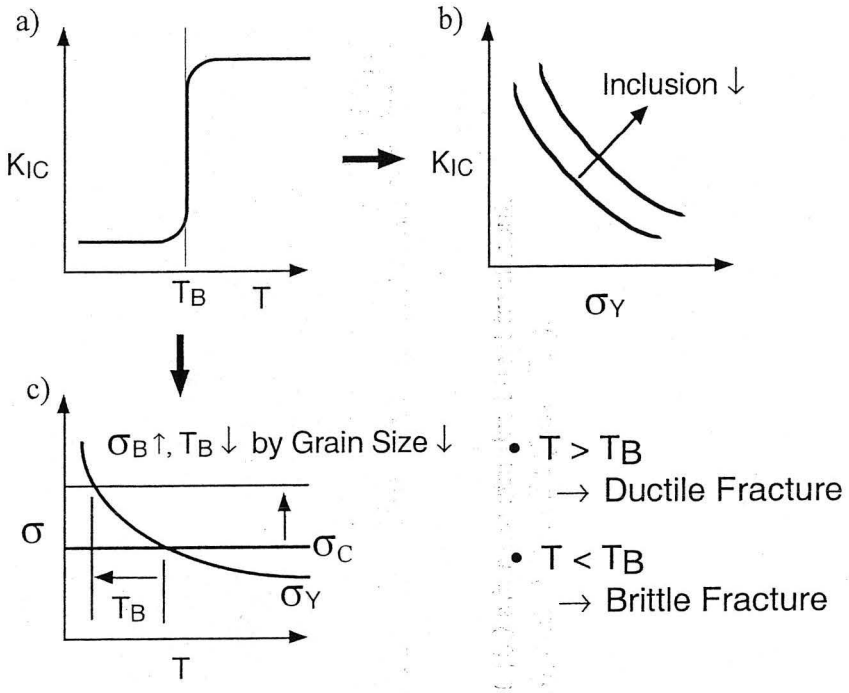

Figure 1.3 Fracture behavior of ferritic steels.

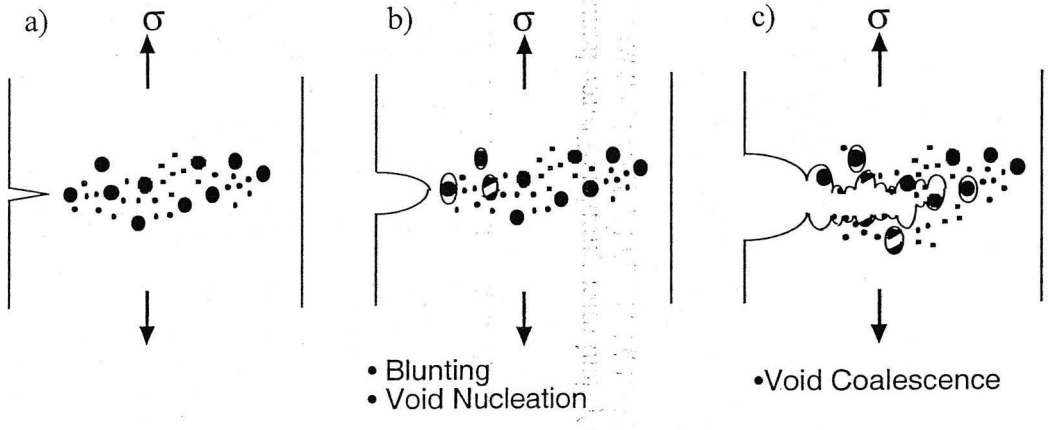

Figure 1.4 Sequence in ductile fracture.

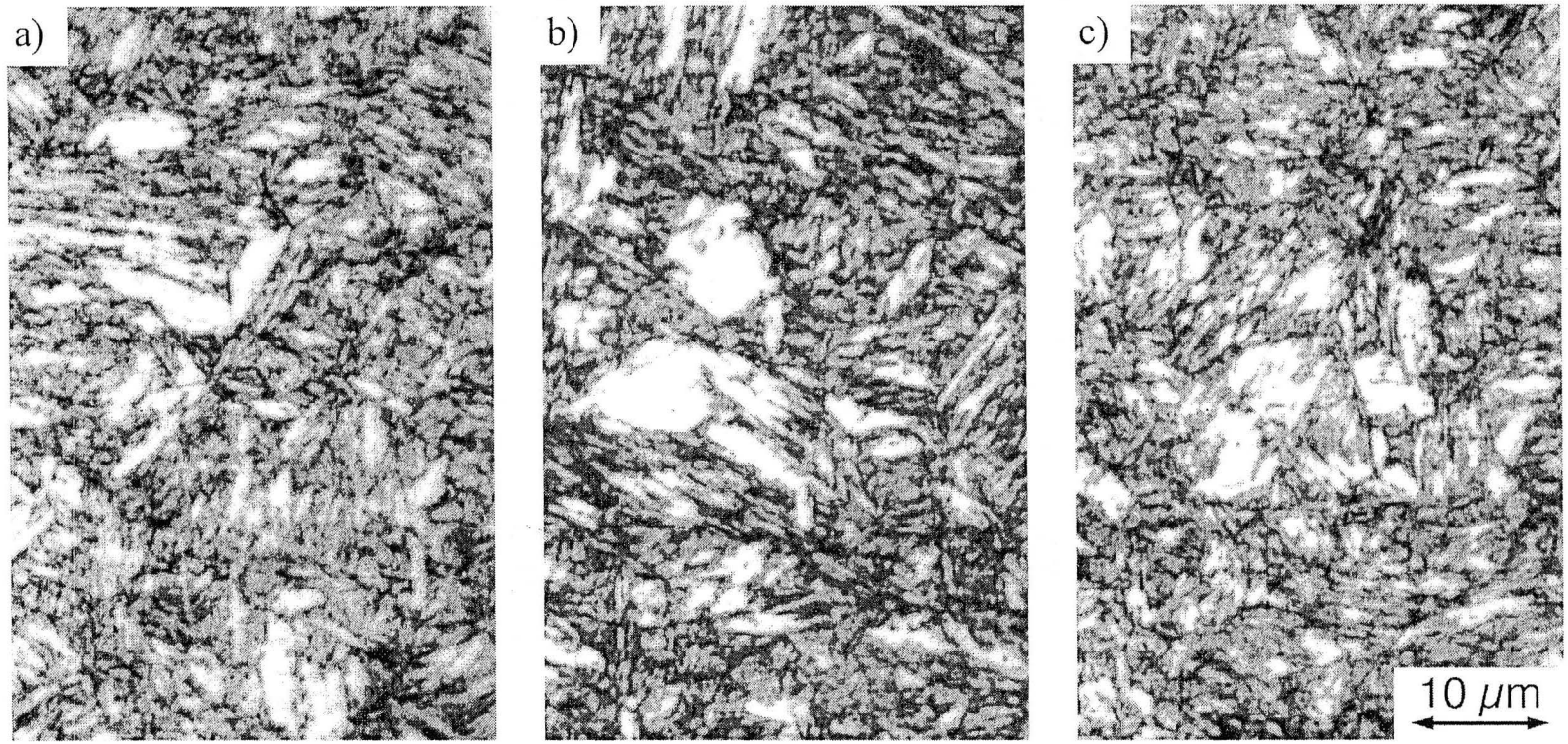

Figure 2.1 Optical micrographs of three heats of AerMet 100 after the standard heat treatment. a) Heat #1 (High K_{IC}), b) Heat #3 (Medium K_{IC}), and c) Heat #2 (Low K_{IC}).

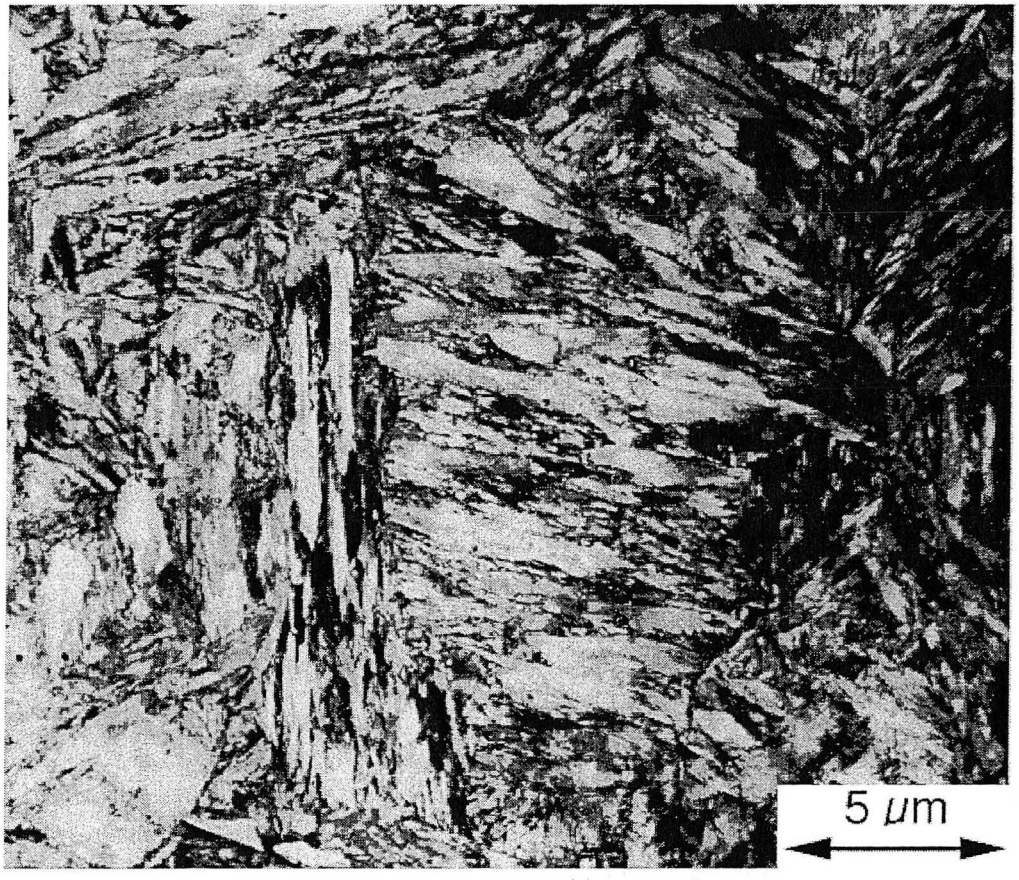

Figure 2.2 TEM bright field image of AerMet 100.
Heat #1, standard heat treatment condition.

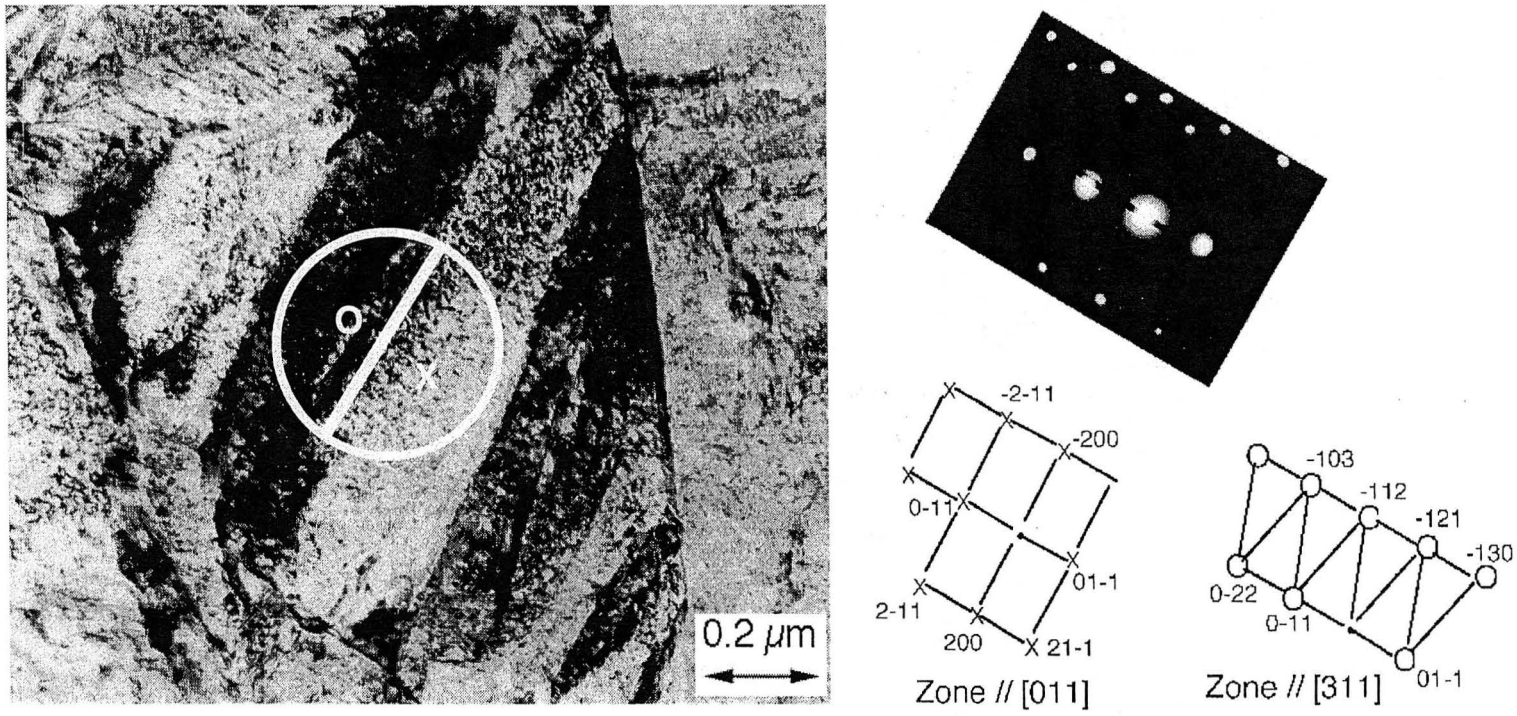

Figure 2.3 TEM bright field image and the SAD pattern of AerMet 100.
Region marked "**O**" in the selected area in the TEM image has zone parallel to [311], and "X" has [011]

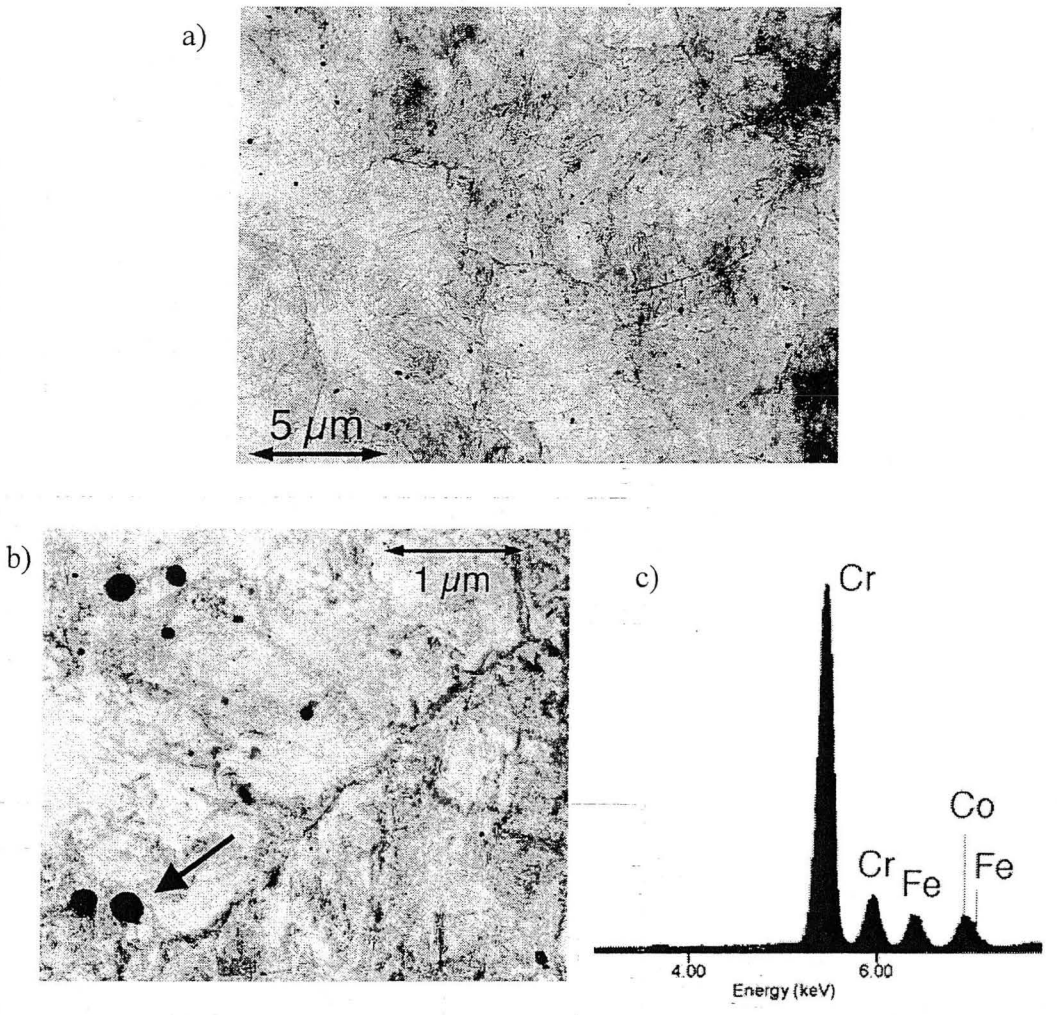

Figure 2.4 TEM micrographs of extraction replica and the EDS analysis of the precipitate.
Sample: Heat #1. Standard heat treatment condition.

- Lower magnification shows the prior austenite grain boundaries.
- Higher magnification shows the spherical precipitates.
- EDS analysis of the precipitate marked by the arrow in b).

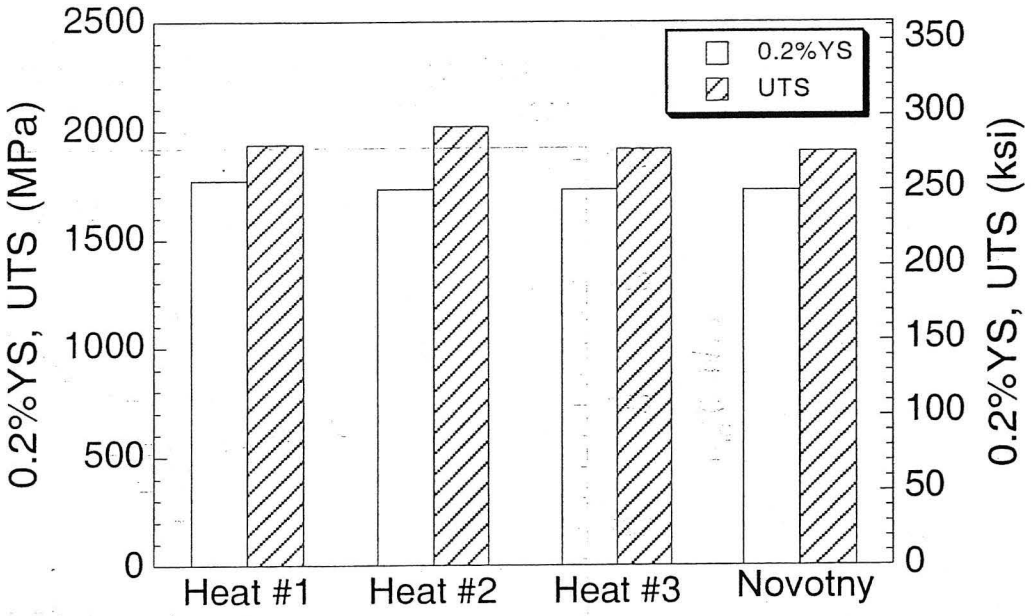

Figure 2.5 0.2% yield strength and ultimate tensile strength of AerMet 100 among 3 heats

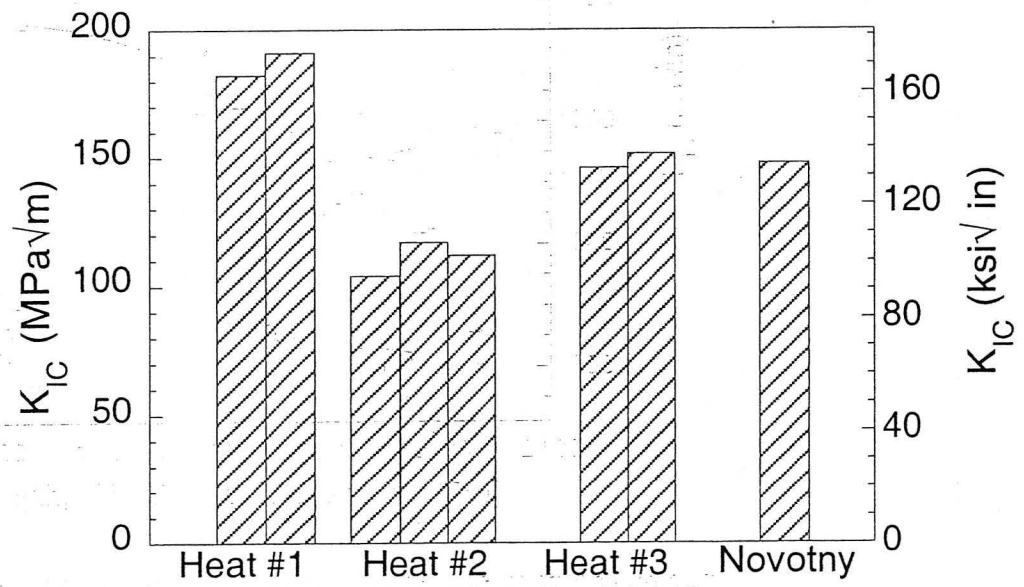

Figure 2.6 Fracture toughness, K_{IC}, of AerMet 100 among 3 heats

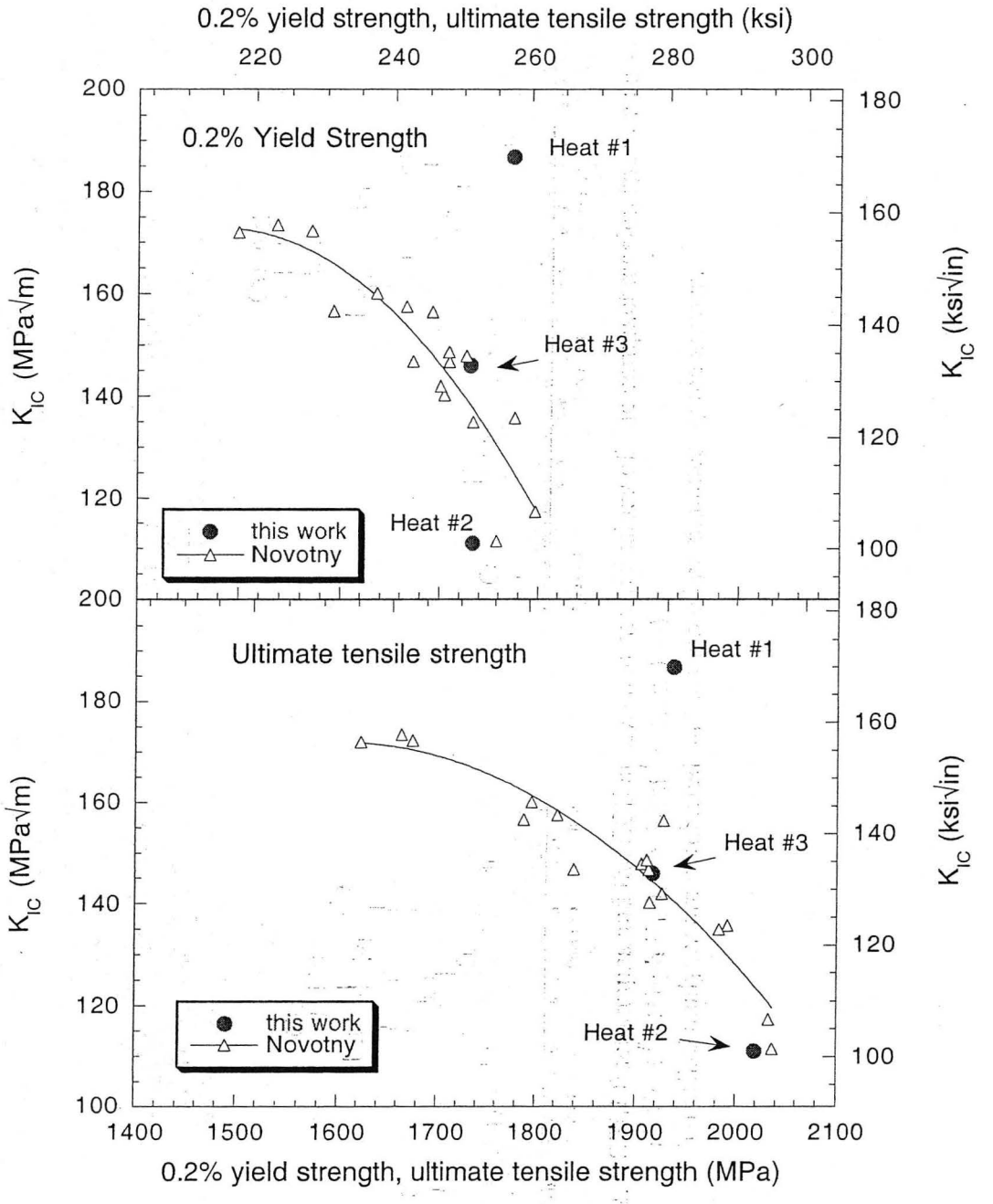

Figure 2.7 Relationship between fracture toughness and tensile strengths among three heats

- All three heats of this study are treated in the standard heat treatment condition.
- Novotny's data is obtained from a series of heat treatments of one heat.

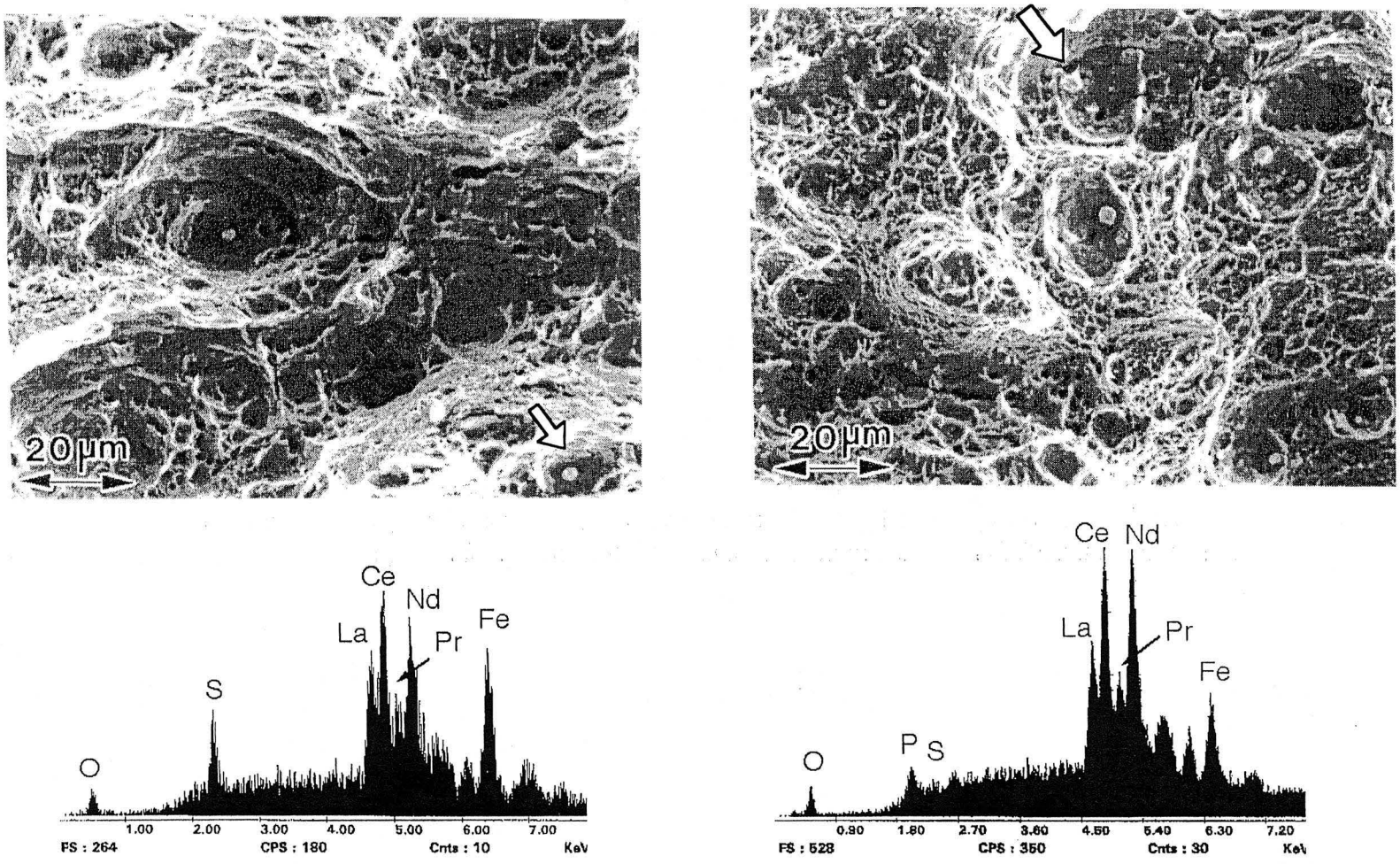

Figure 2.8 SEM fractographs and the EDS analyses of the inclusions of the compact tension specimens a) Heat #1 (High K_{IC}), b) Heat #2 (Low K_{IC})
The EDS analyses are conducted on the marked precipitates by the arrows.

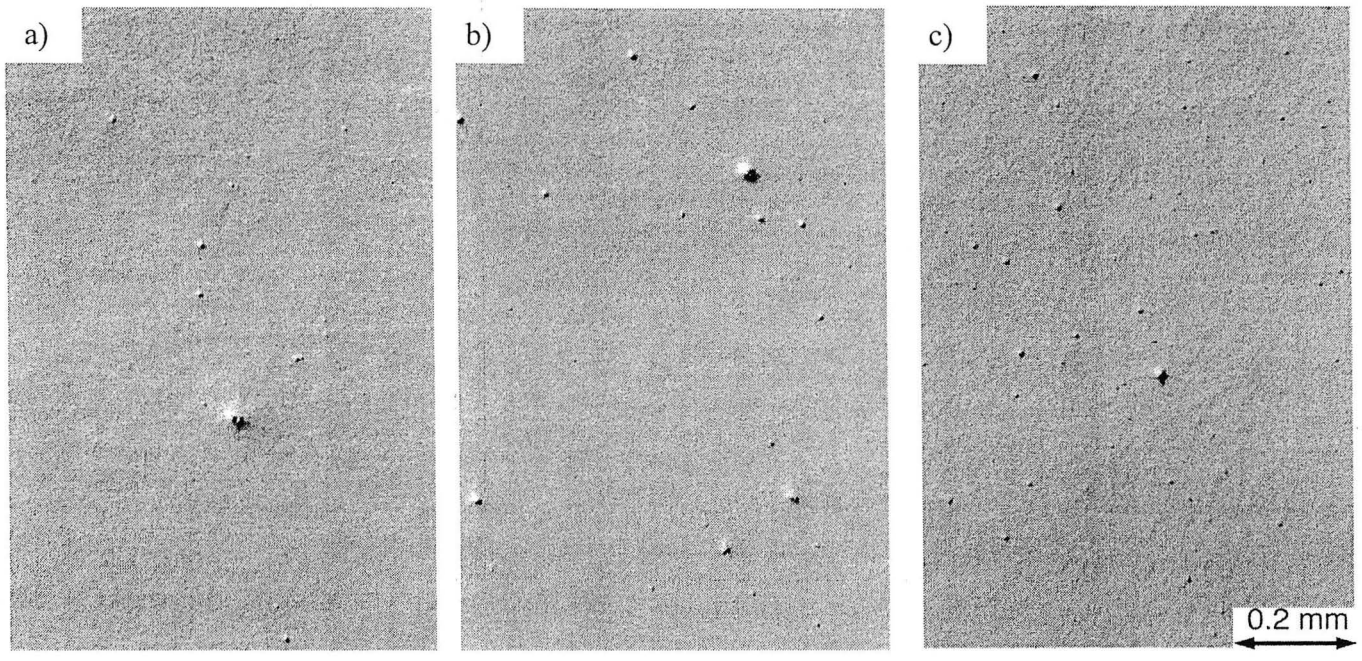

Figure 2.9 Optical micrographs of three heats of AerMet 100 as polished condition. a) Heat #1 (High K_{IC}), b) Heat #3 (Medium K_{IC}), and c) Heat #2 (Low K_{IC}).

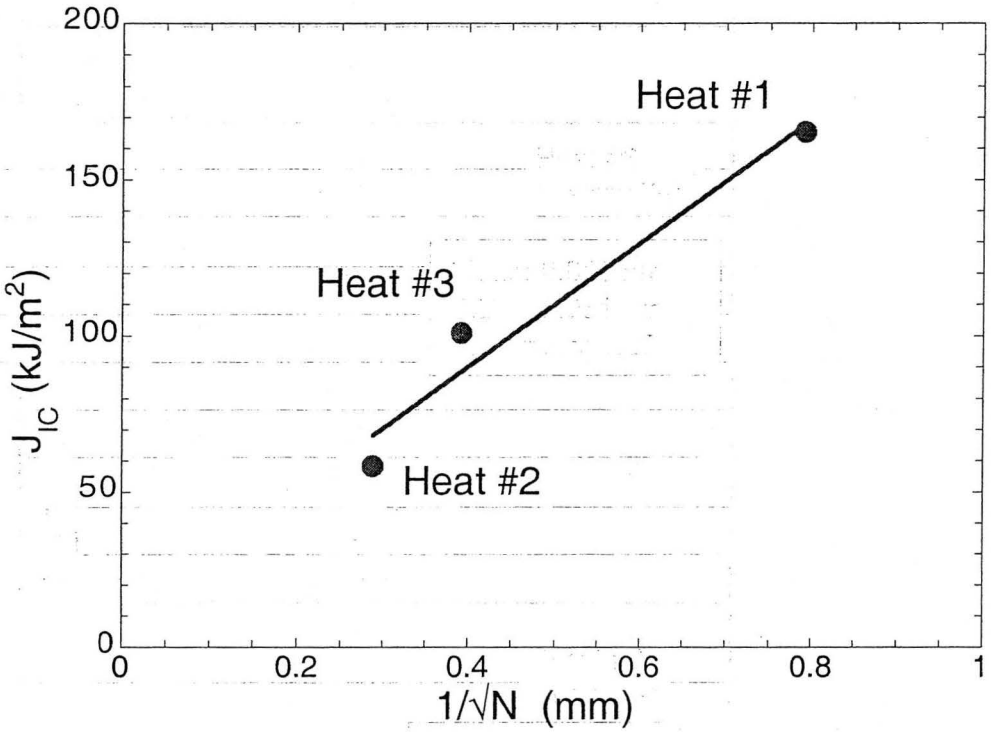

Figure 2.10 Effect of areal inclusion spacing on the fracture toughness. Minimum resolvable particle diameter ≈ 2μm.

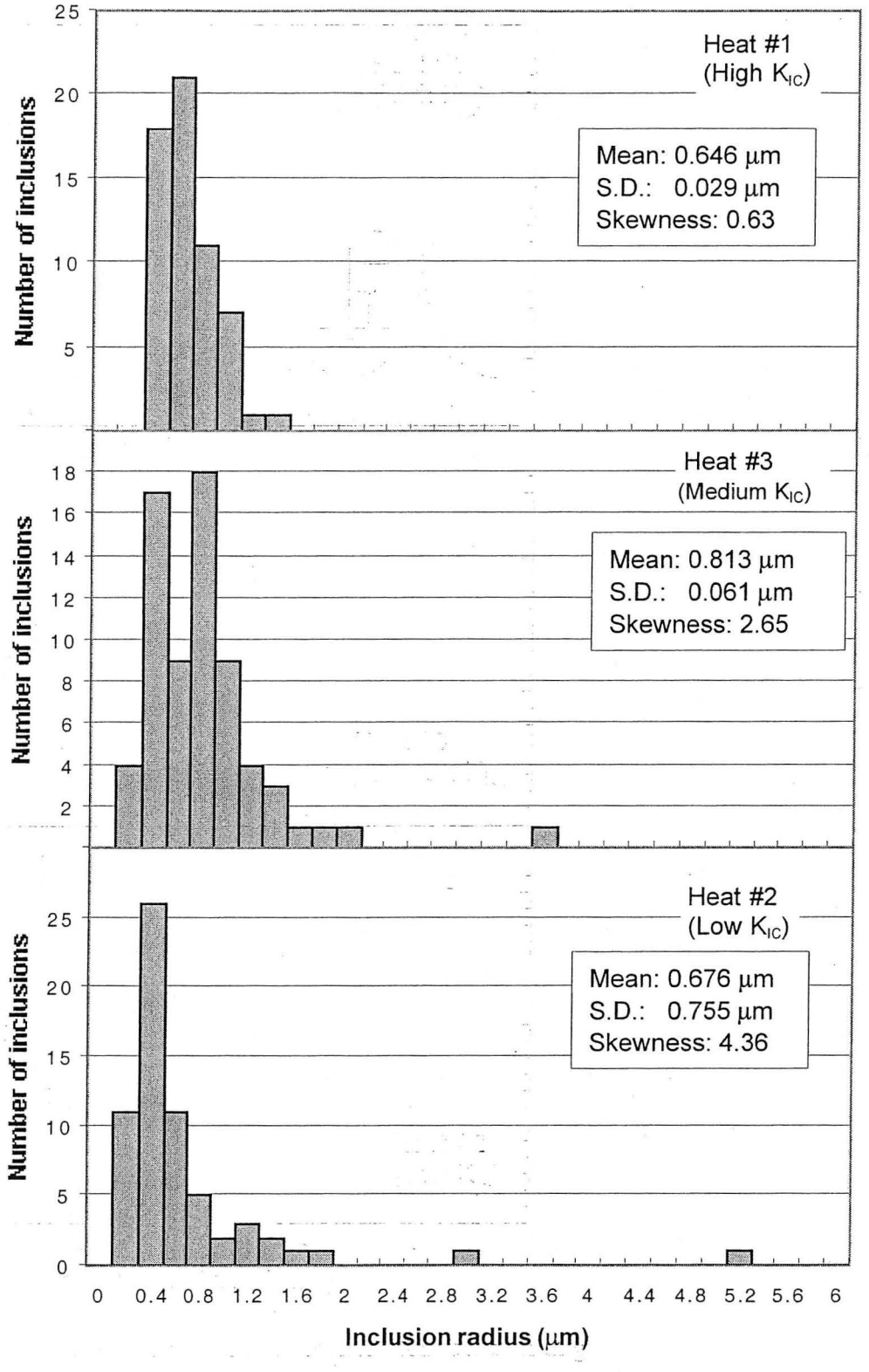

Figure 2.11 The size distributions of the inclusions observed on the fracture surfaces of the compact tension specimens.

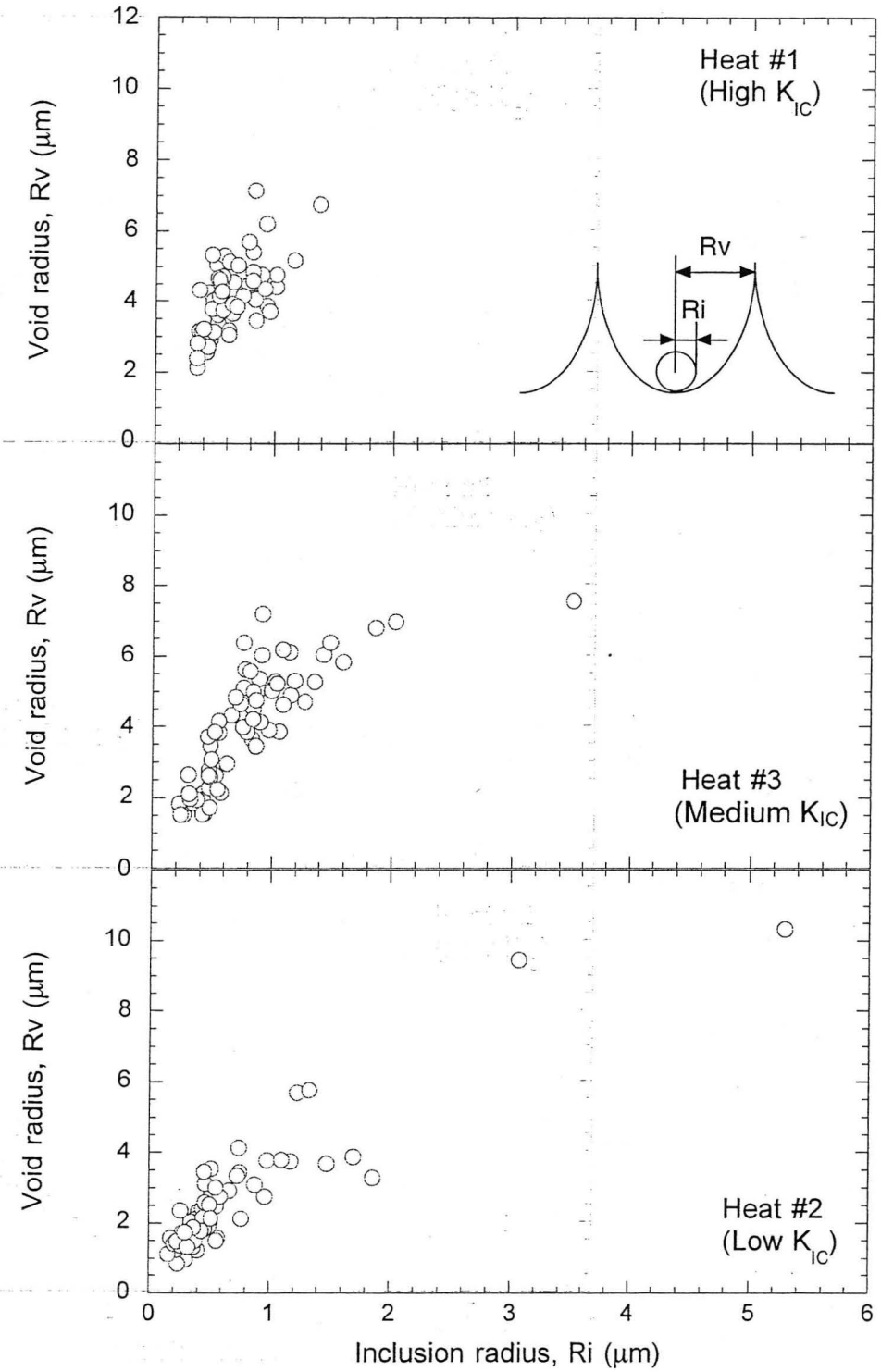

Figure 2.12 Relationship between the void radius and the inclusion radius sitting in the void

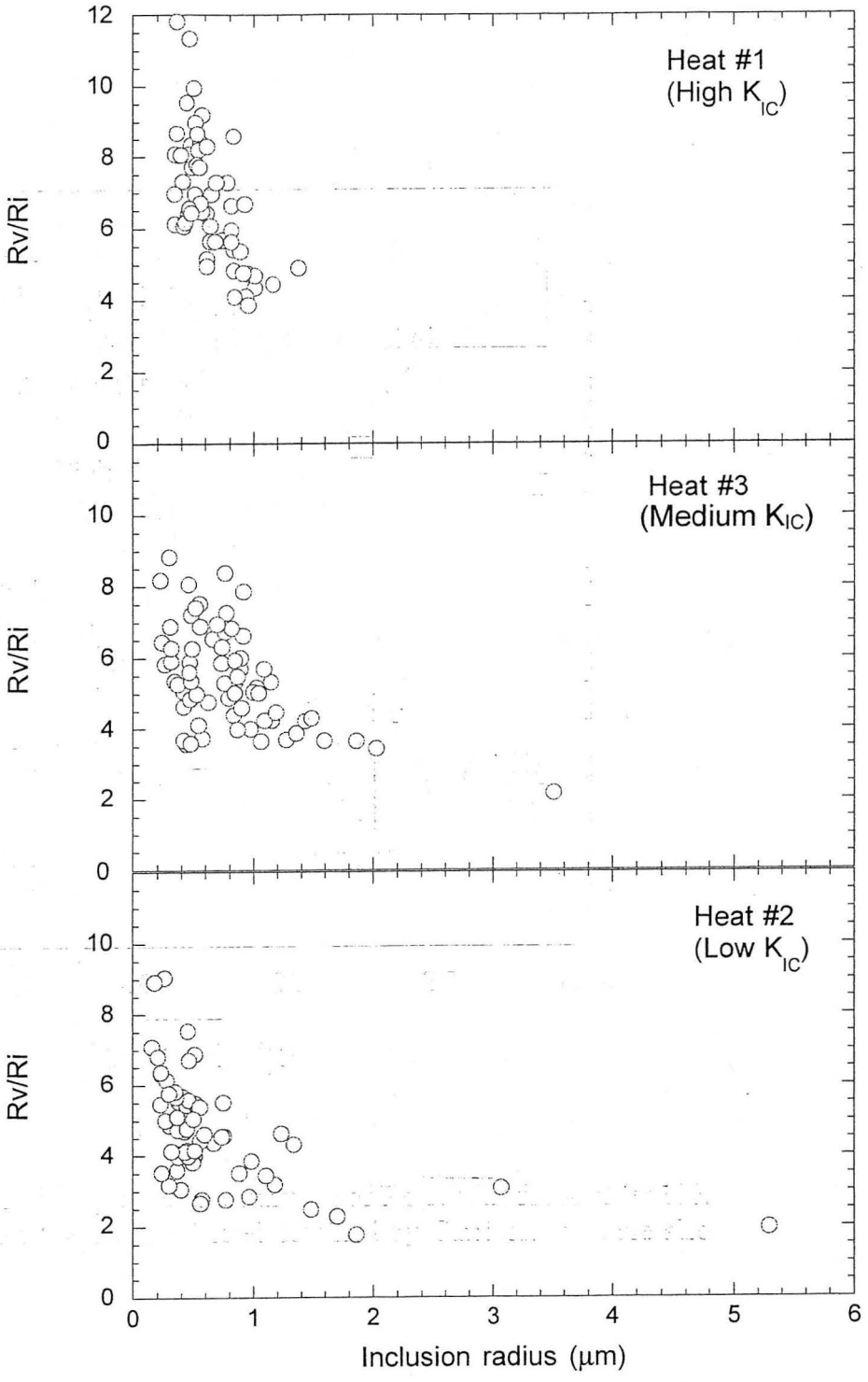

Figure2.13 Plots of the void growth factor (Rv/Ri) as a function of inclusion radius (Ri)

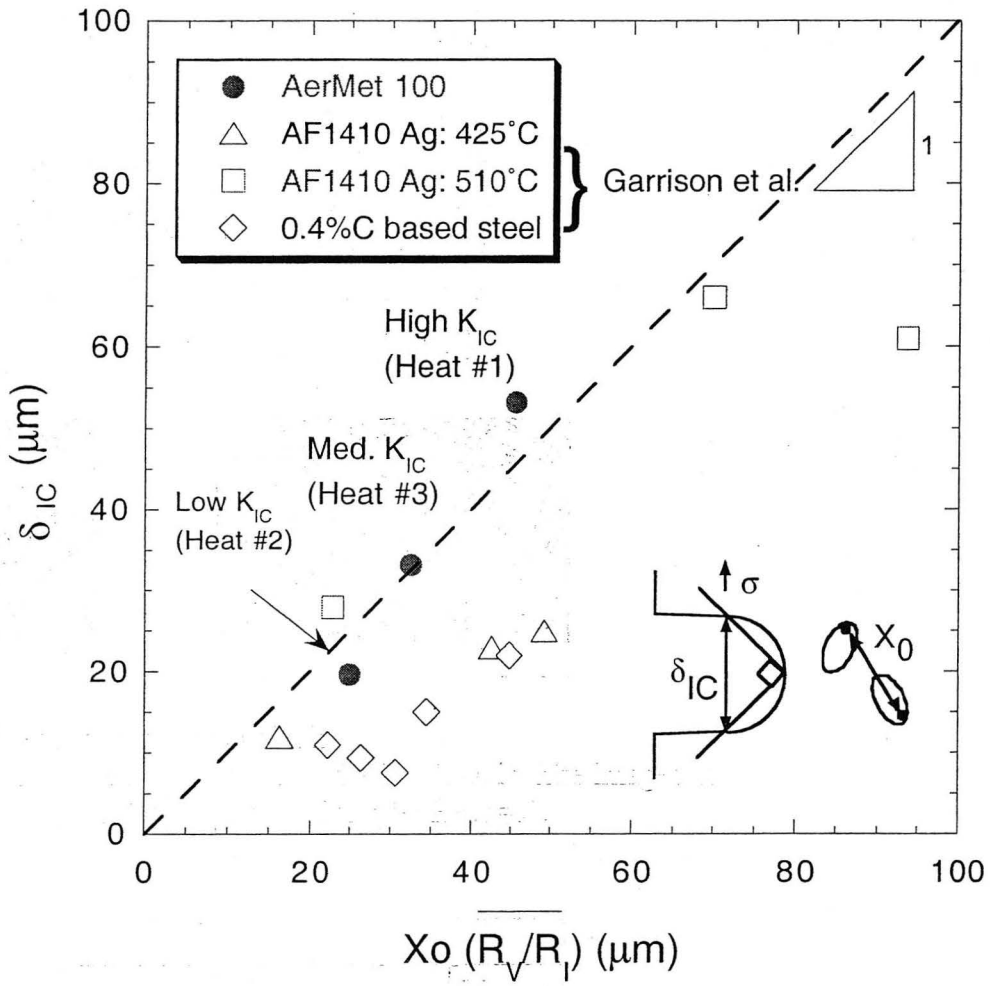

Figure 2.14 Calculated values of δ_{IC} plotted as a function of $\overline{Xo(Rv/Ri)}$ for AerMet 100. The results of AF1410 and 0.4%C based steel obtained by Garrison *et al.* are also plotted in comparison.

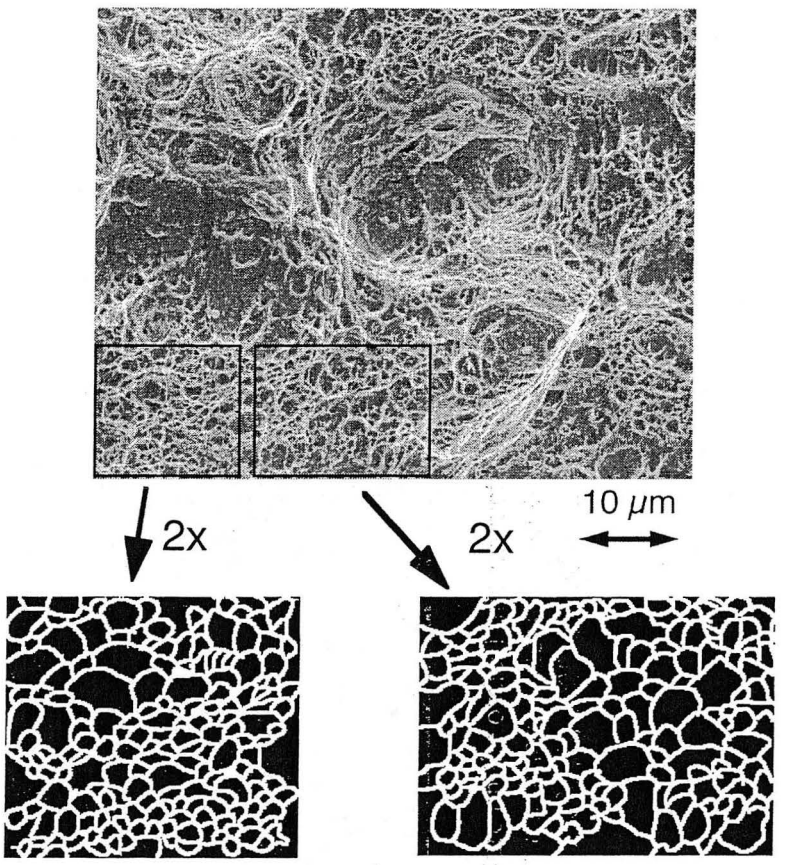

Figure 2.15 An example of secondary voids analysis.
Secondary void spacings are calculated from the black and white images of the secondary void sheet coalescence area (Sample: Heat #1).

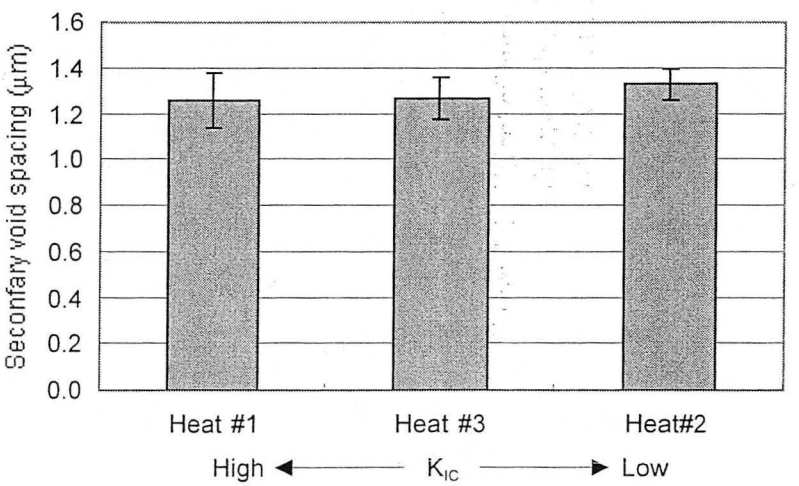

Figure 2.16 Secondary void spacings

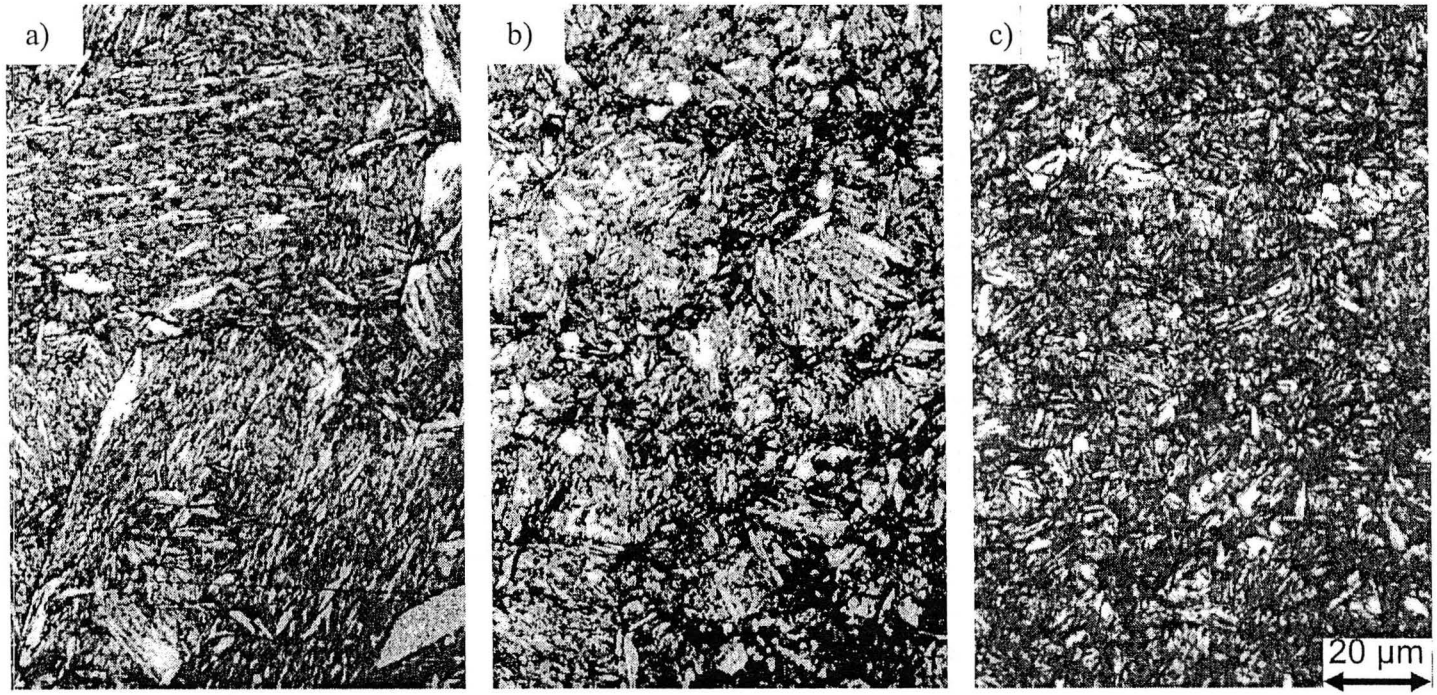

Figure 3.1 Effect of austenitizing temperature on the optical microstructure of AerMet 100. Sample: Heat #1, heat treatment condition: austenitization + the deep freeze + aging. Austenitizing temperatures: a) 1100°C, b) 1000°C, and c) 885°C(standard).

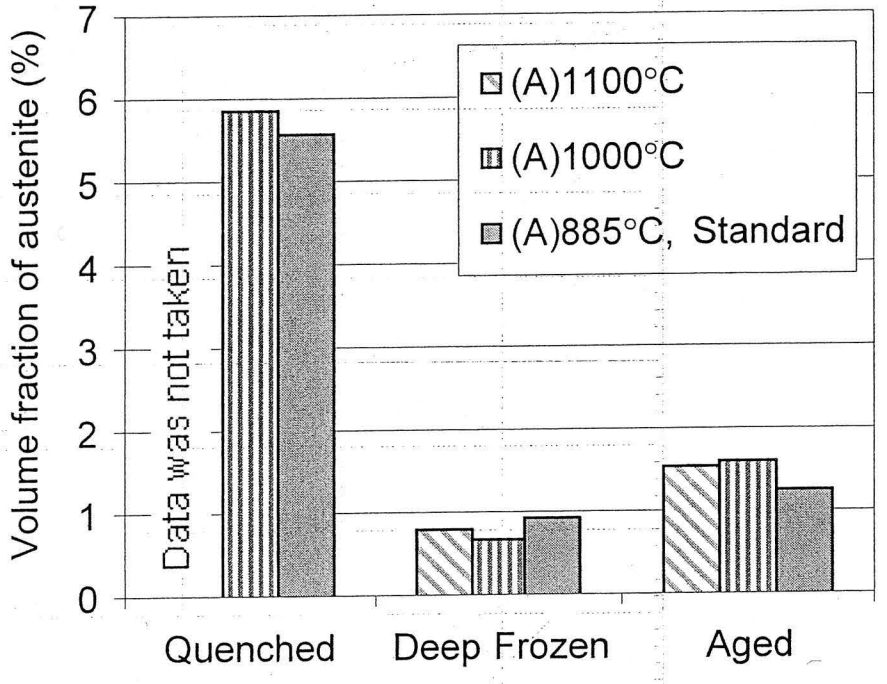

Figure 3.2 Effect of austenitization temperature on the fraction of austenite.

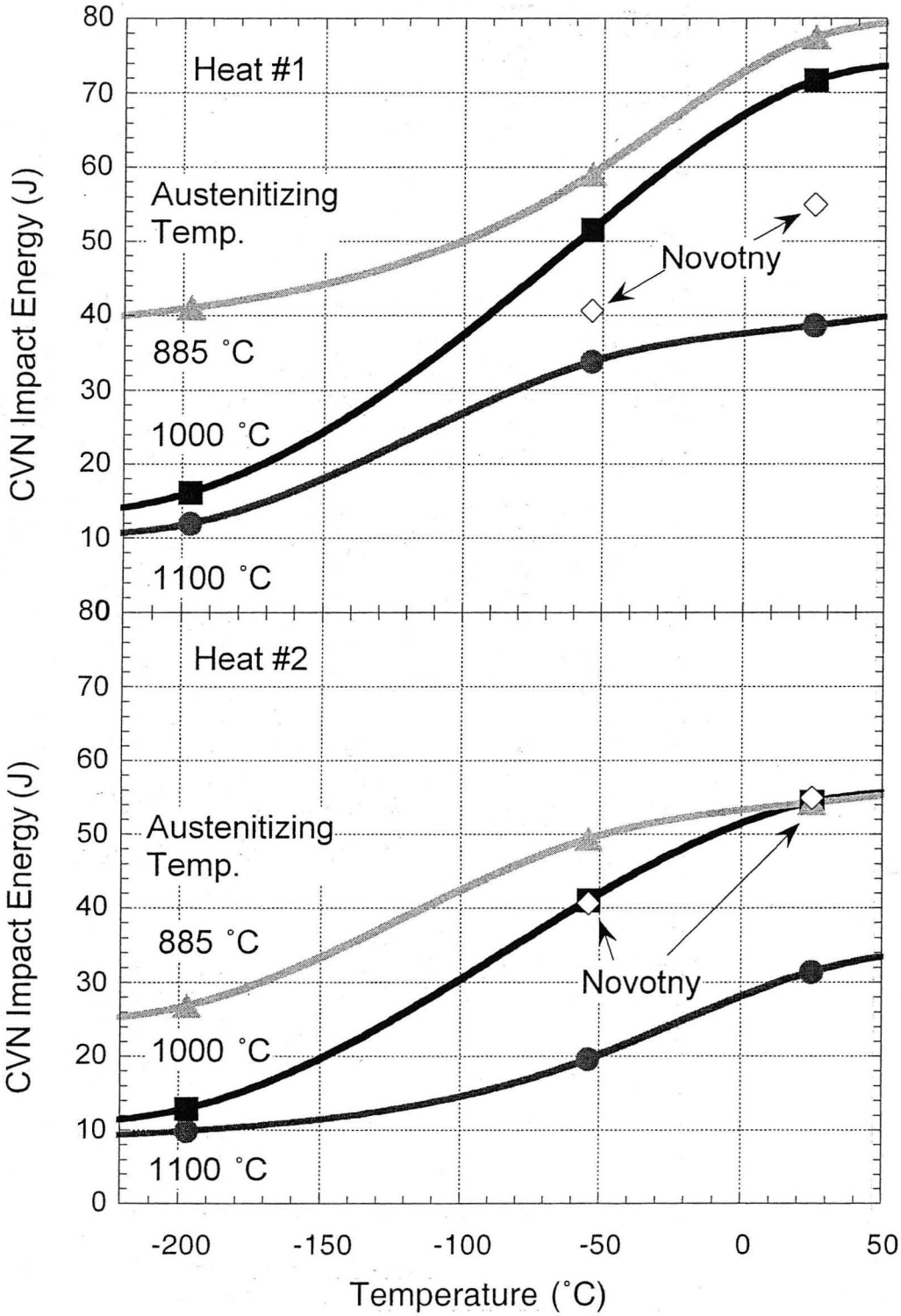

Figure 3.3 Effect of austenitizing temperature on the temperature dependence of the CVN impact energy.

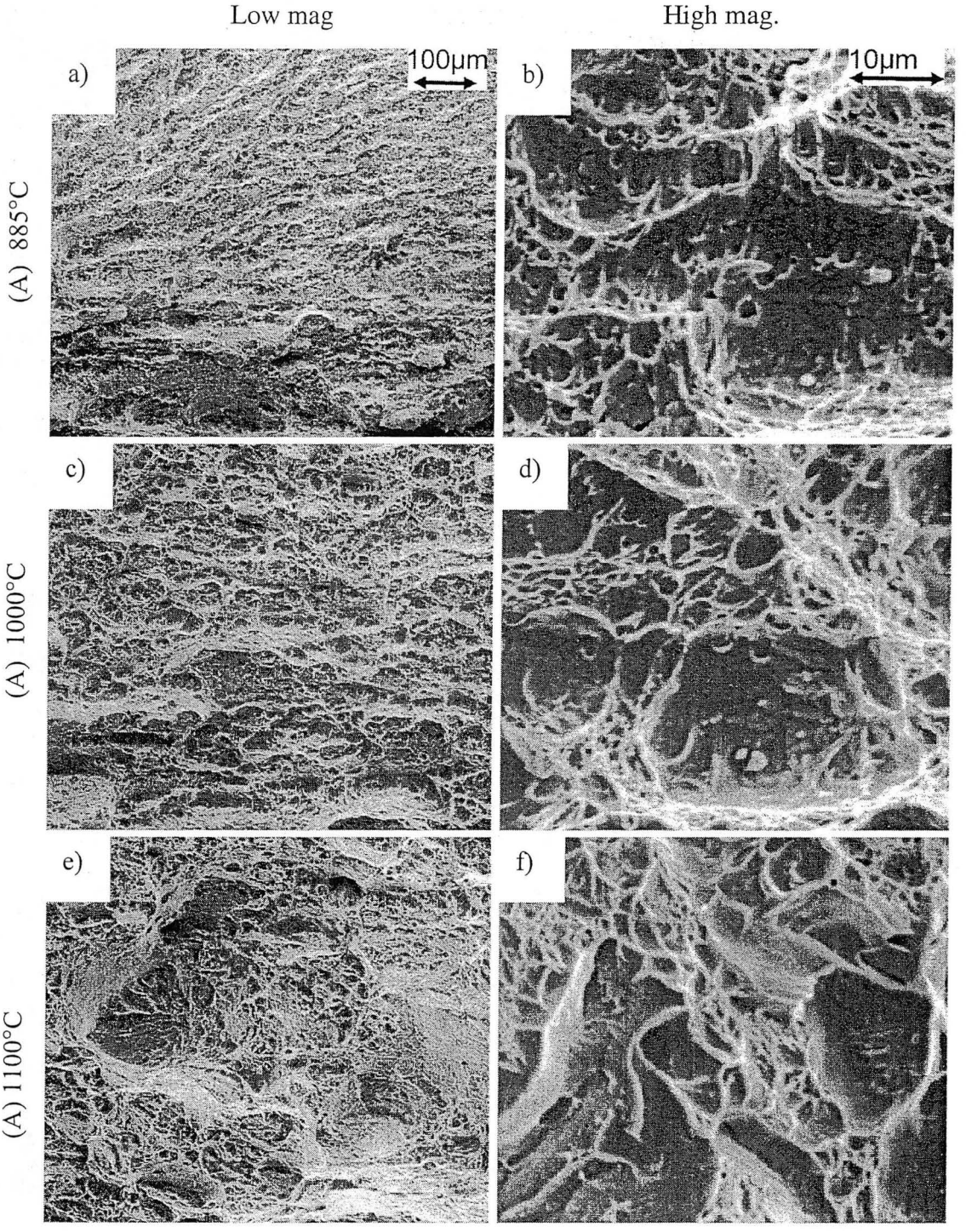

Figure 3.4 SEM fractographs of the CVN specimens of Heat #1
Test temperature: RT. Cracks propagate from the bottom to the top of the images.
a), b) (A) 885°C / 77.5 J, c), d) (A) 1000°C / 71.7J, and e), f) (A) 1100°C / 38.6J.

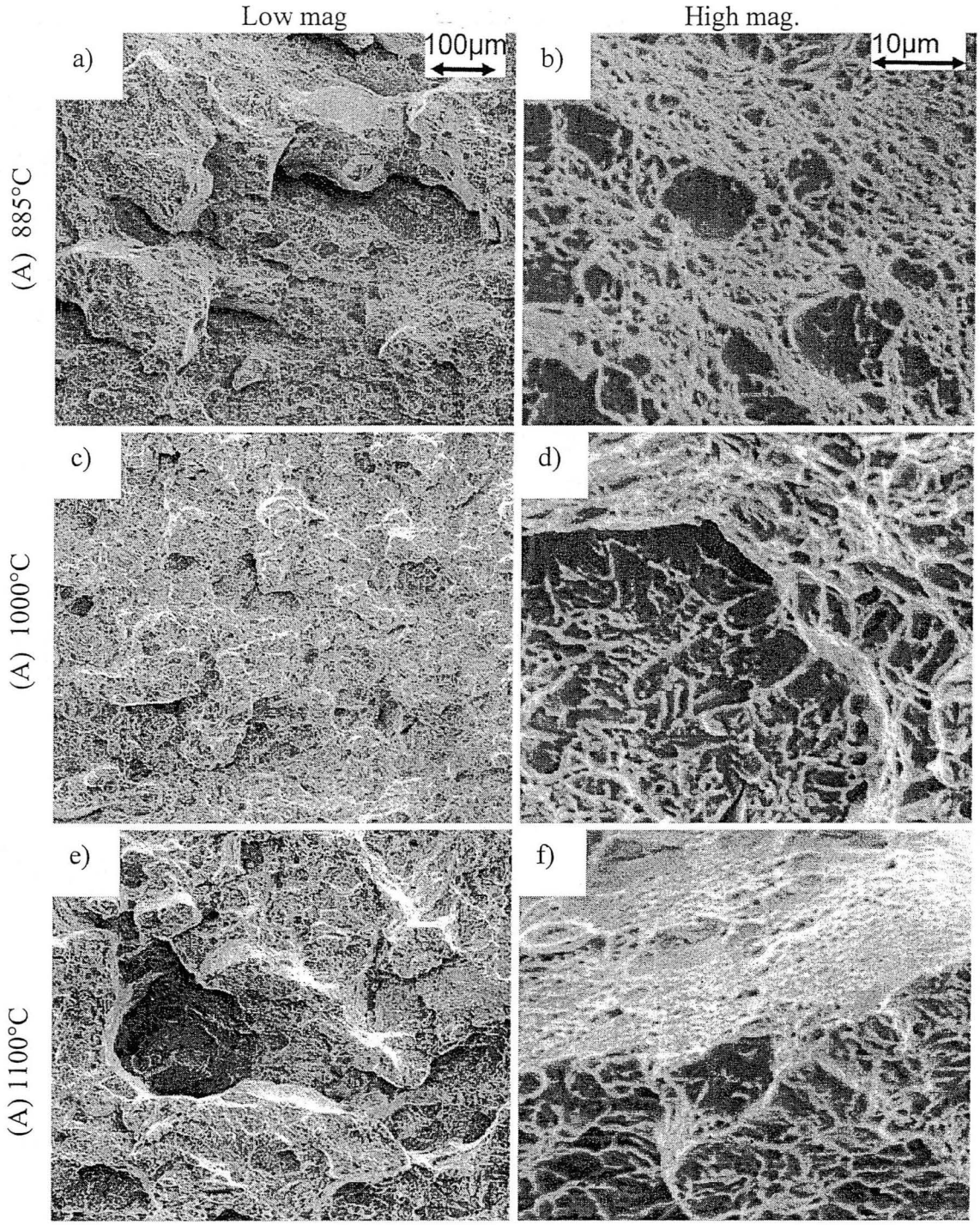

Figure 3.5 SEM fractographs of the CVN specimens of Heat #1
Test temperature: -197°C. Cracks propagate from the bottom to the top of the images.
a), b) (A) 885°C / 41.0J, c), d) (A) 1000°C / 16.1J, and e), f) (A) 1100°C / 11.9J.

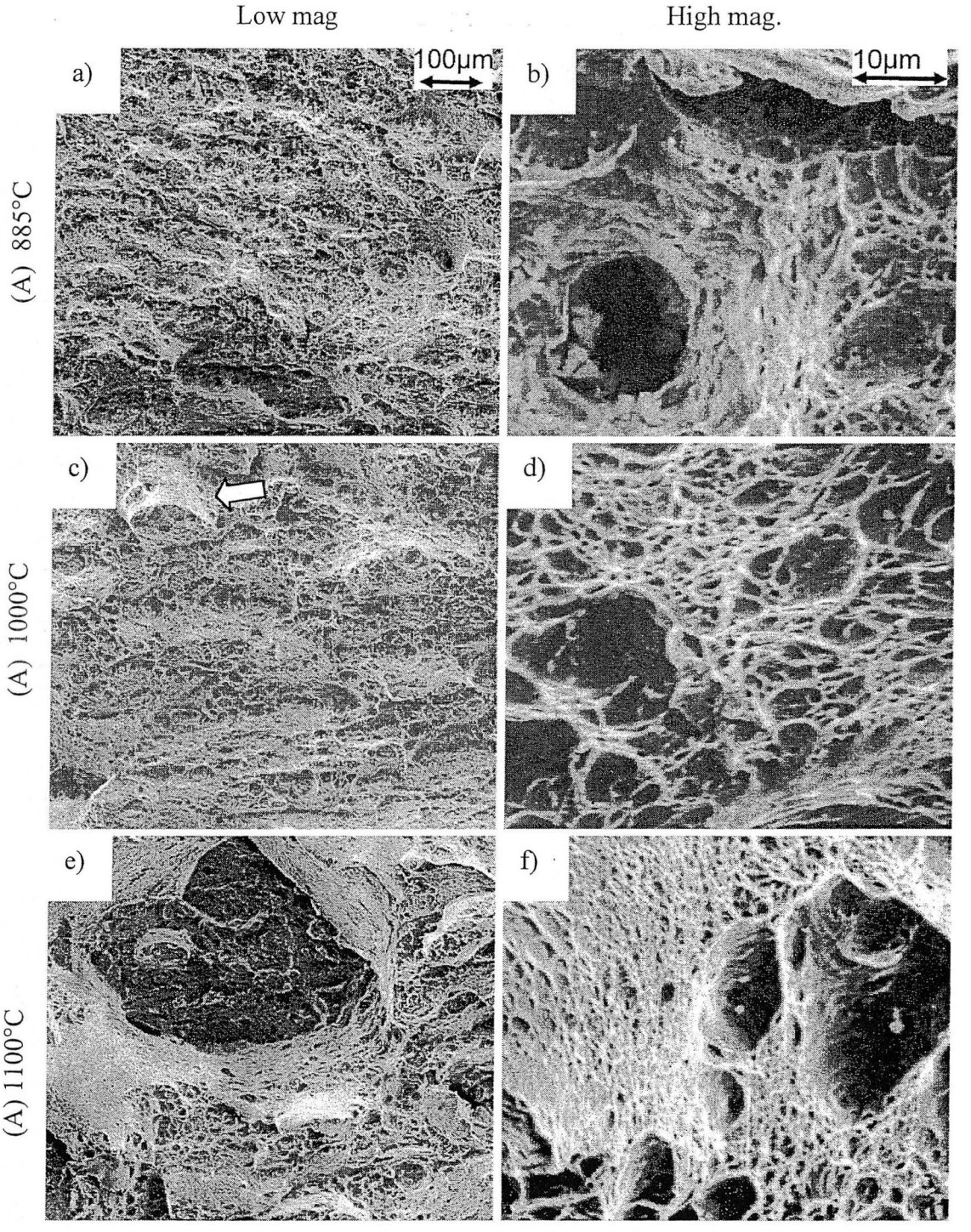

Figure 3.6 SEM fractographs of the CVN specimens of Heat #2
Test temperature: RT. Cracks propagate from the bottom to the top of the images.
a), b) (A) 885°C / 54.2 J, c), d) (A) 1000°C / 54.4 J, and e), f) (A) 1100°C / 31.3 J.
* An example of the plateau is marked by the arrow in c).

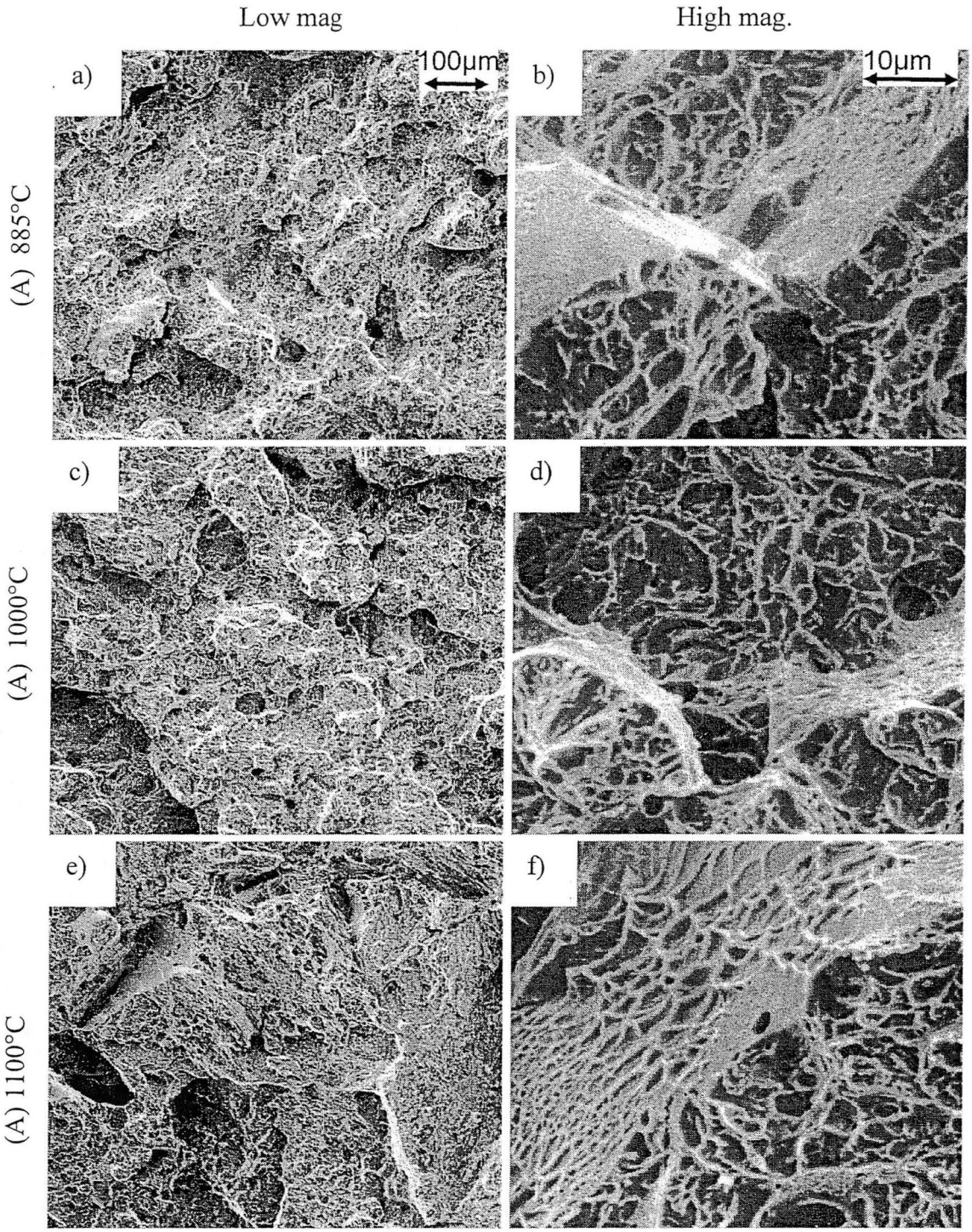

Figure 3.7 SEM fractographs of the CVN specimens of Heat #2
Test temperature: -197°C. Cracks propagate from the bottom to the top of the images.
a), b) (A) 885°C / 26.8 J, c), d) (A) 1000°C / 12.9 J, and e), f) (A) 1100°C / 9.9J.

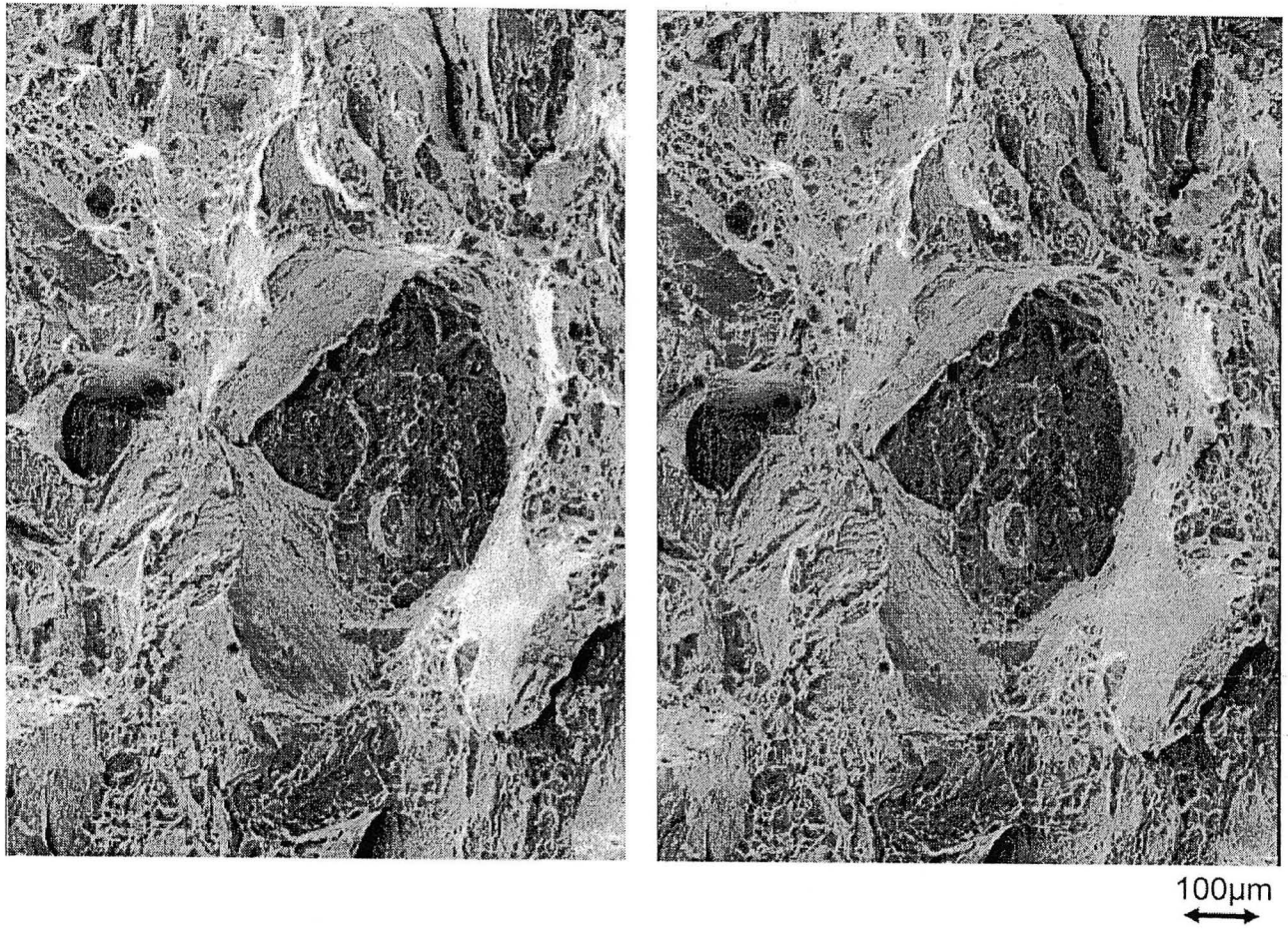

Figure 3.8 A stereo pair of SEM fractographs.
Sample: Heat #2, (A) 1100°C, Test temperature: 25°C, CVN impact energy: 9.9J.

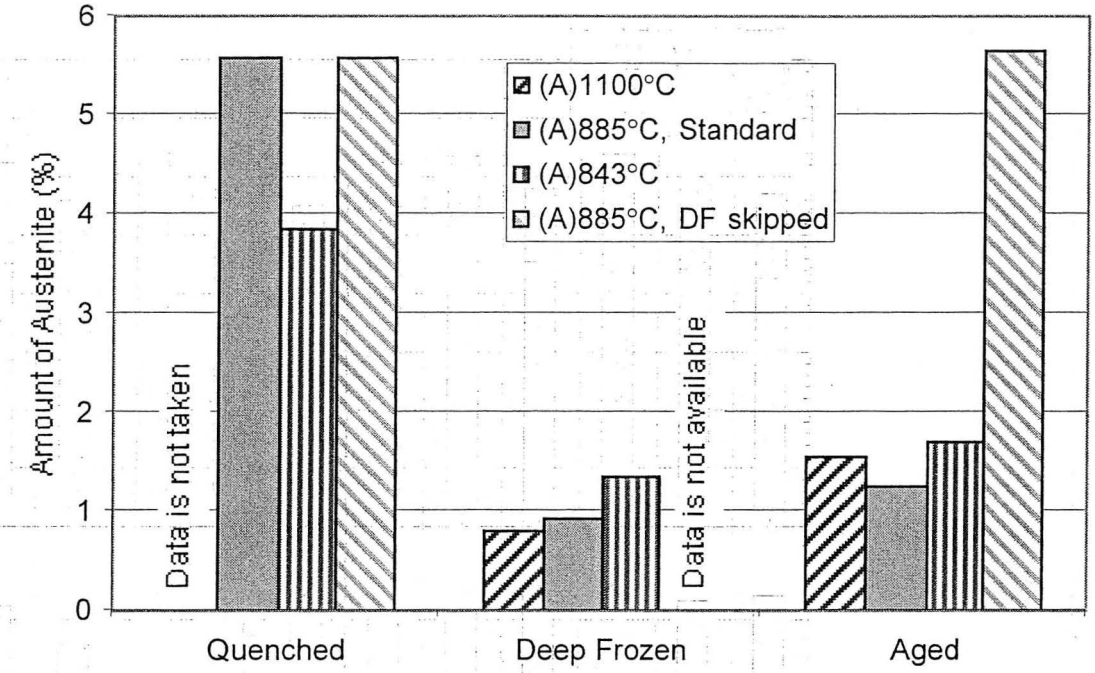

Figure 4.1 Effect of austenitizing temperature and the deep freeze on the fraction of austenite.

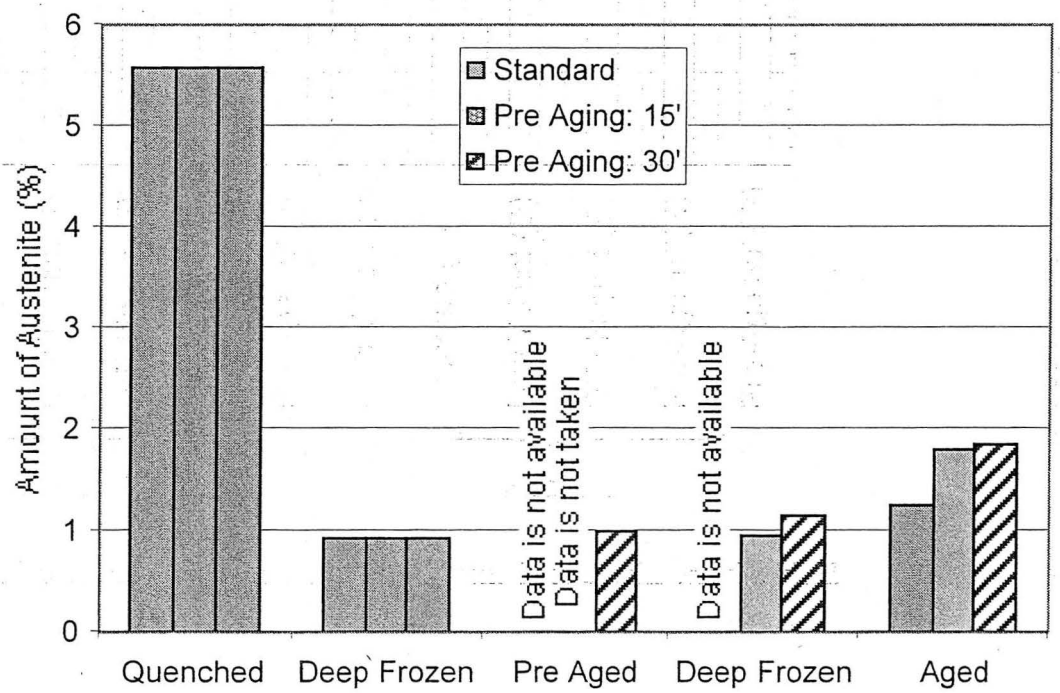

Figure 4.2 Effect of pre-aging on the fraction of austenite.

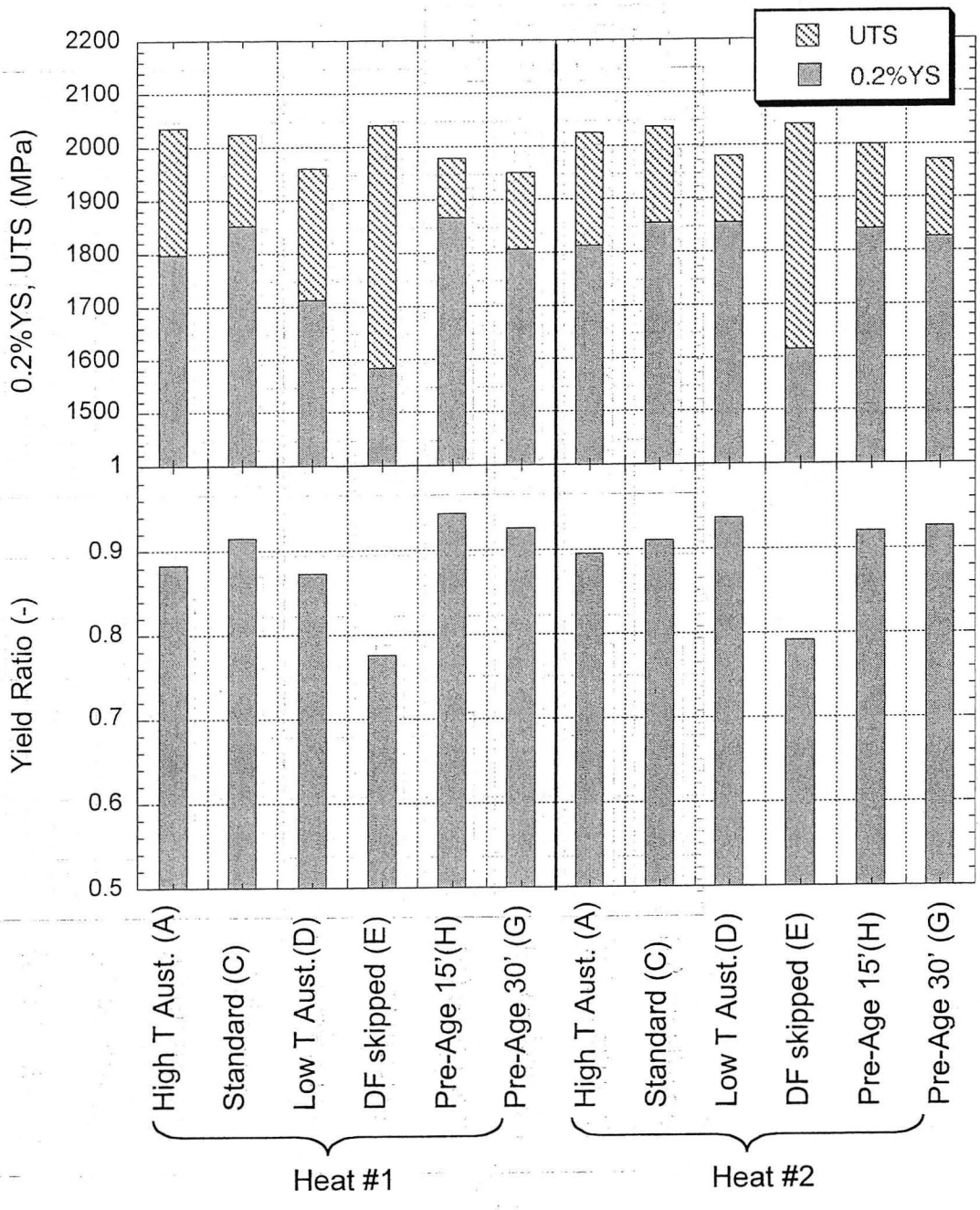

Figure 4.3 Effect of heat treatment conditions on the tensile strengths and the yield ratios.

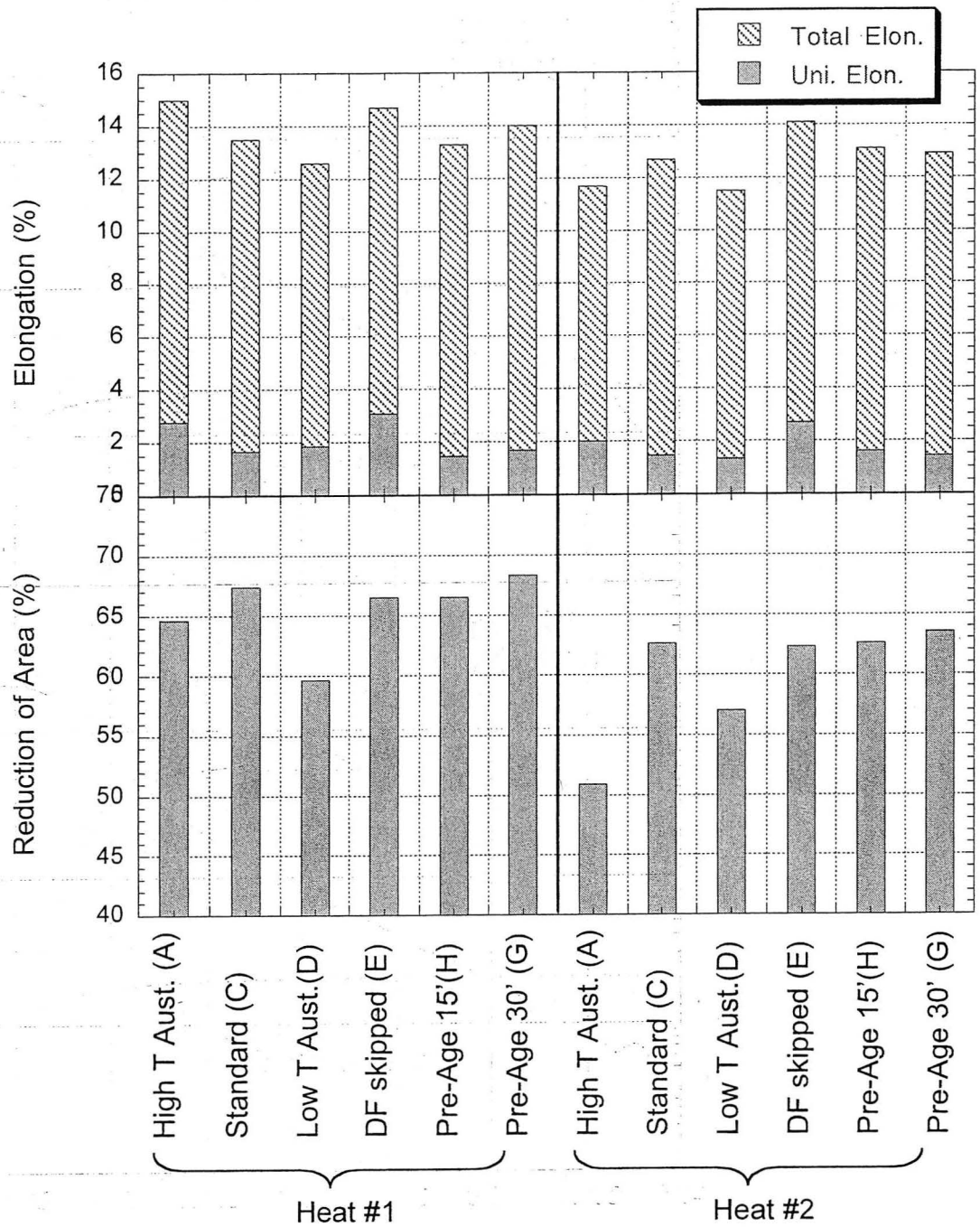

Figure 4.4 Effect of heat treatment conditions on the eleongations and the reduction of area.

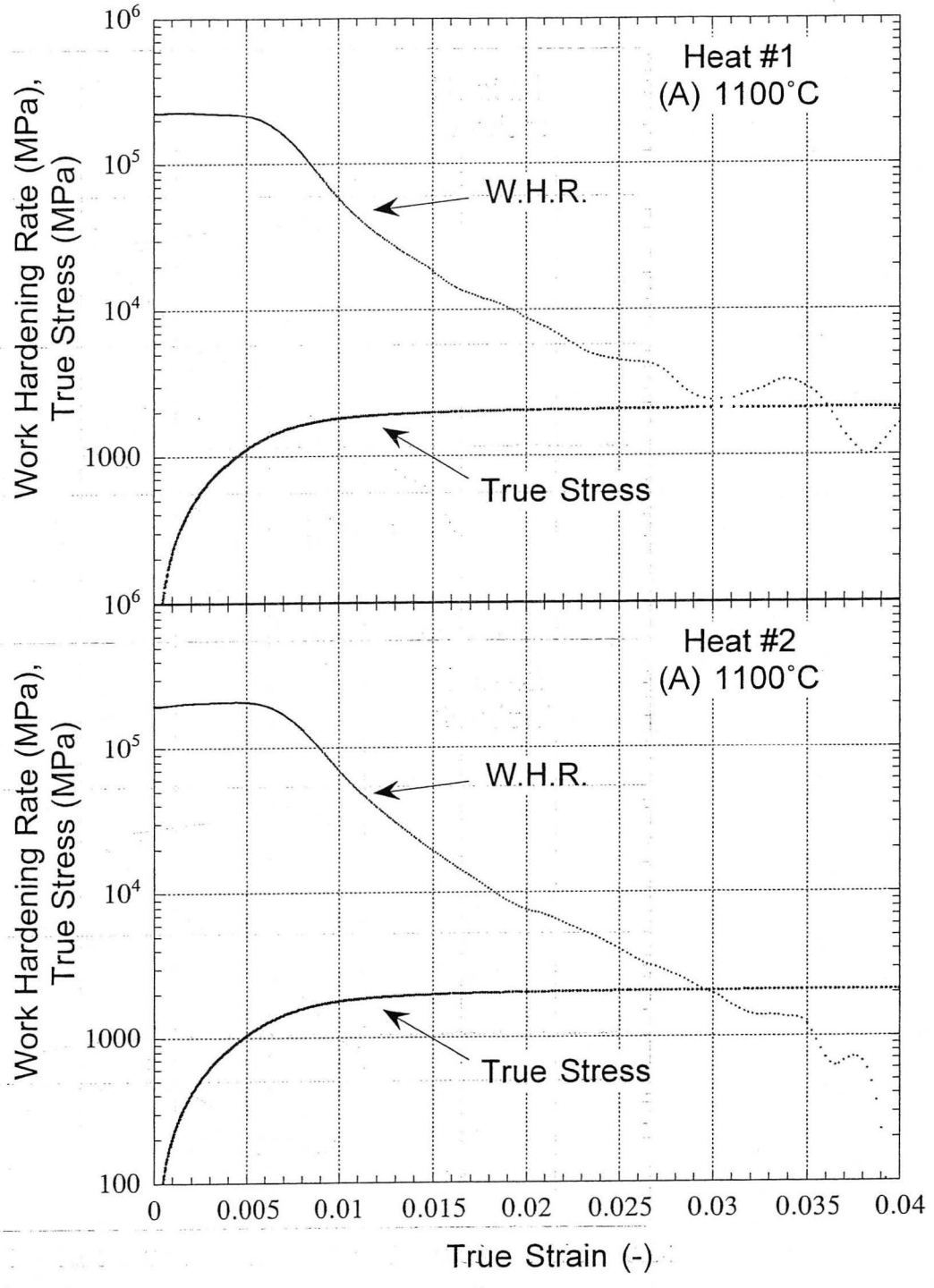

Figure 4.5 Effect of high temperature austenitization on the work hardening rate – true strain curve.
Heat treatment: (A) 1100°C x 1hr, OQ +(DF)-197°C x 1h + (Ag) 482°C x 5h, OQ

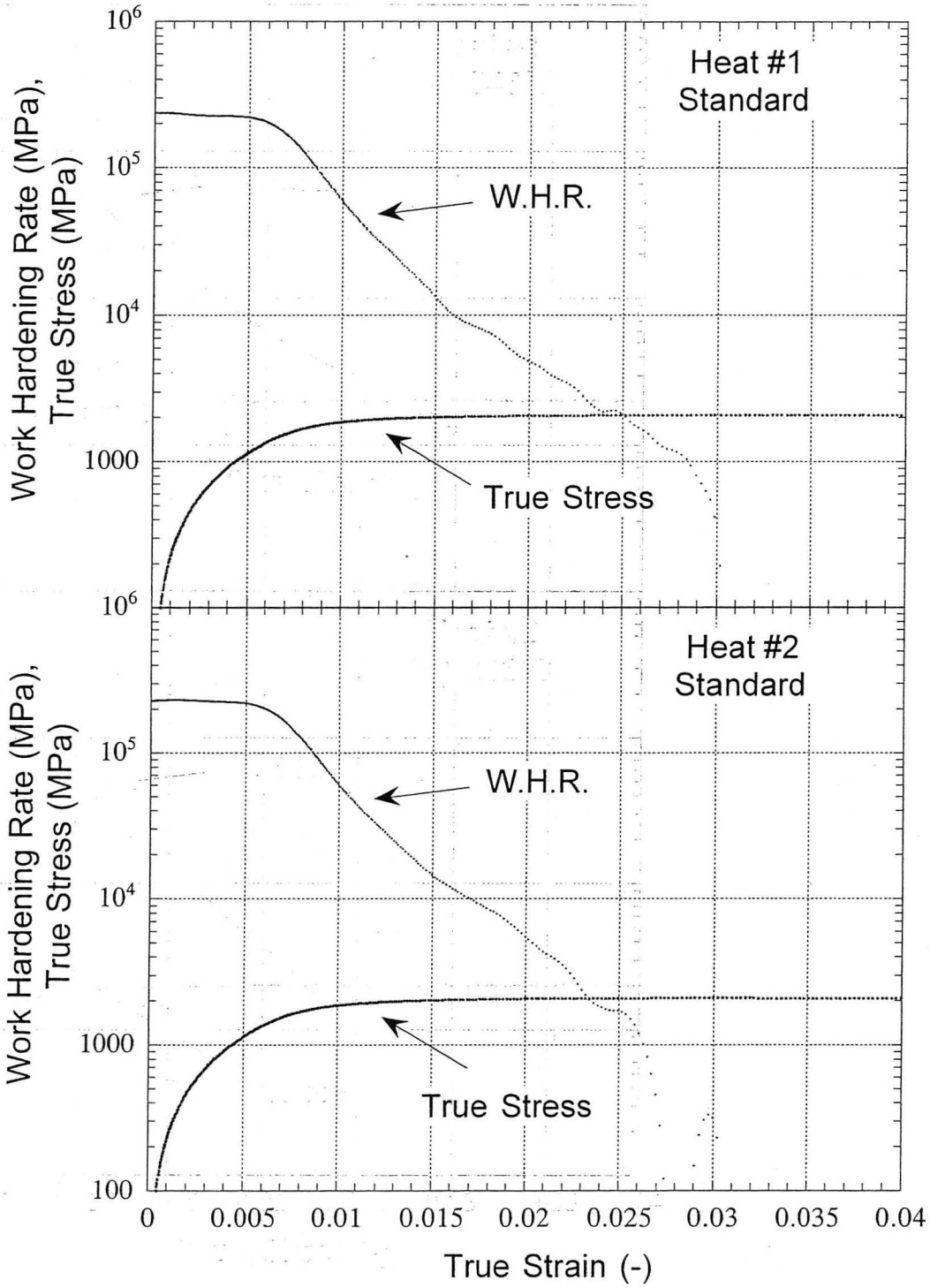

Figure 4.6 Work hardening rate – true strain curve.
Standard heat treatment:
(A) 885°C x 1hr, OQ +(DF)-197°C x 1h + (Ag) 482°C x 5h, OQ

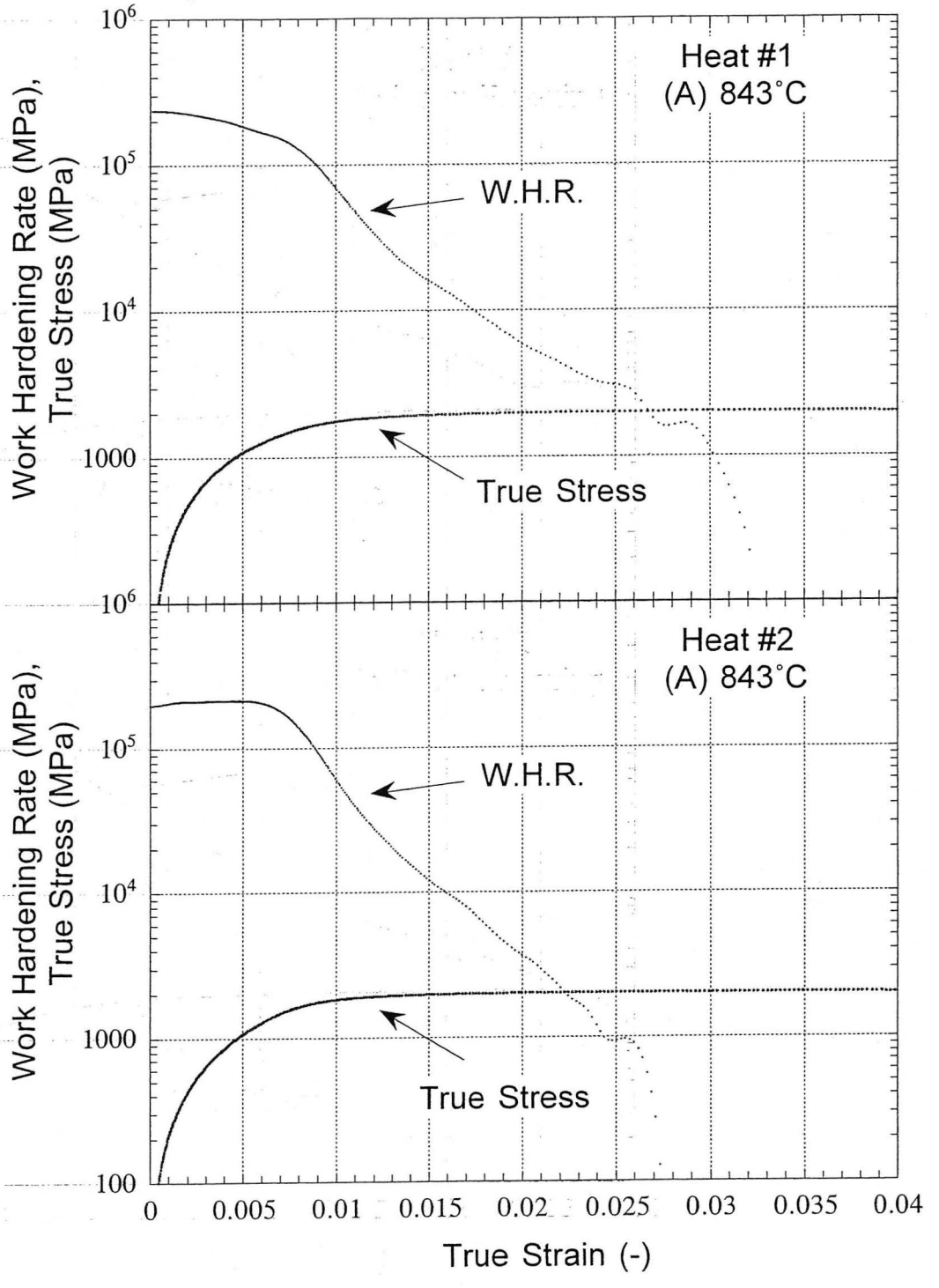

Figure 4.7 Effect of low temperature austenitization on the work hardening rate - true strain curve.
Heat treatment: (A) 843°C x 1hr, OQ +(DF)-197°C x 1h + (Ag) 482°C x 5h, OQ

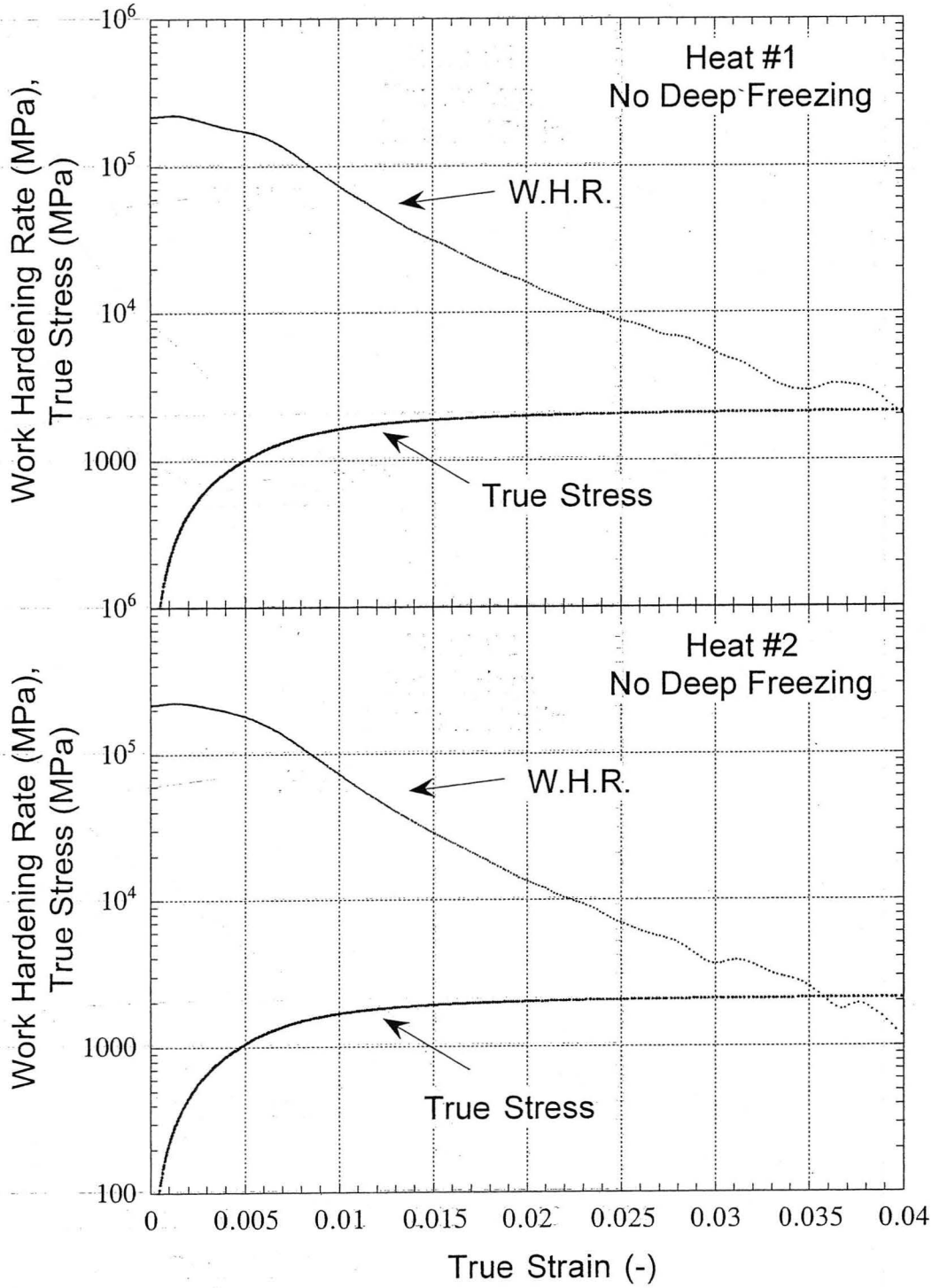

Figure 4.8 Effect of skipping the deep freeze on the work hardening rate – true strain curve. Heat treatment : (A) 885°C x 1hr, OQ + (Ag) 482°C x 5h, OQ

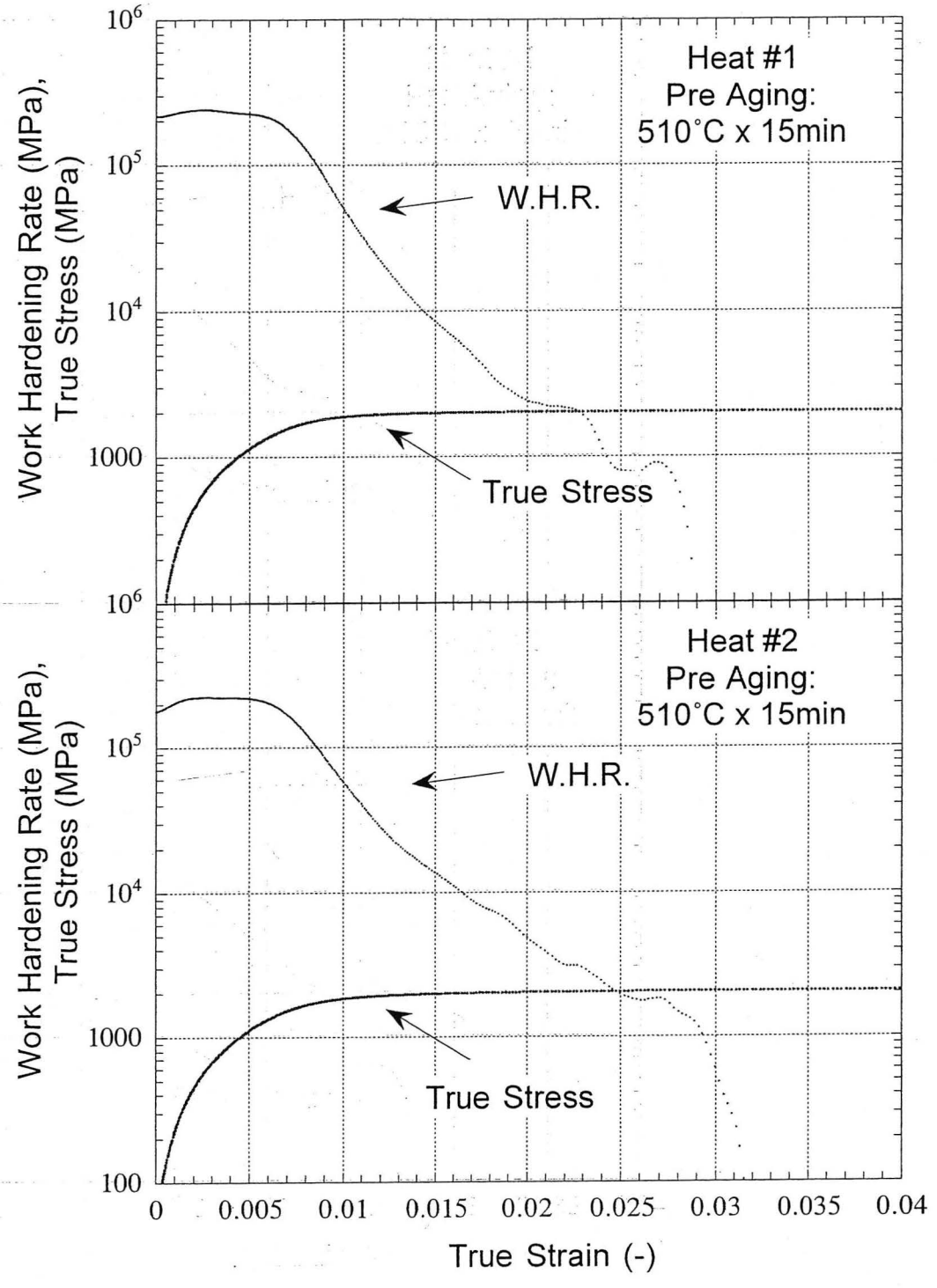

Figure 4.9 Effect of pre-aging on the work hardening rate – true strain curve.
Heat treatment: (A)885°C x 1h, OQ + (DF)-197°C x 1h +
(PreAg)510°C x 15min, OQ + (DF)-197°C x 1h + (Ag) 482°C x 5h, OQ

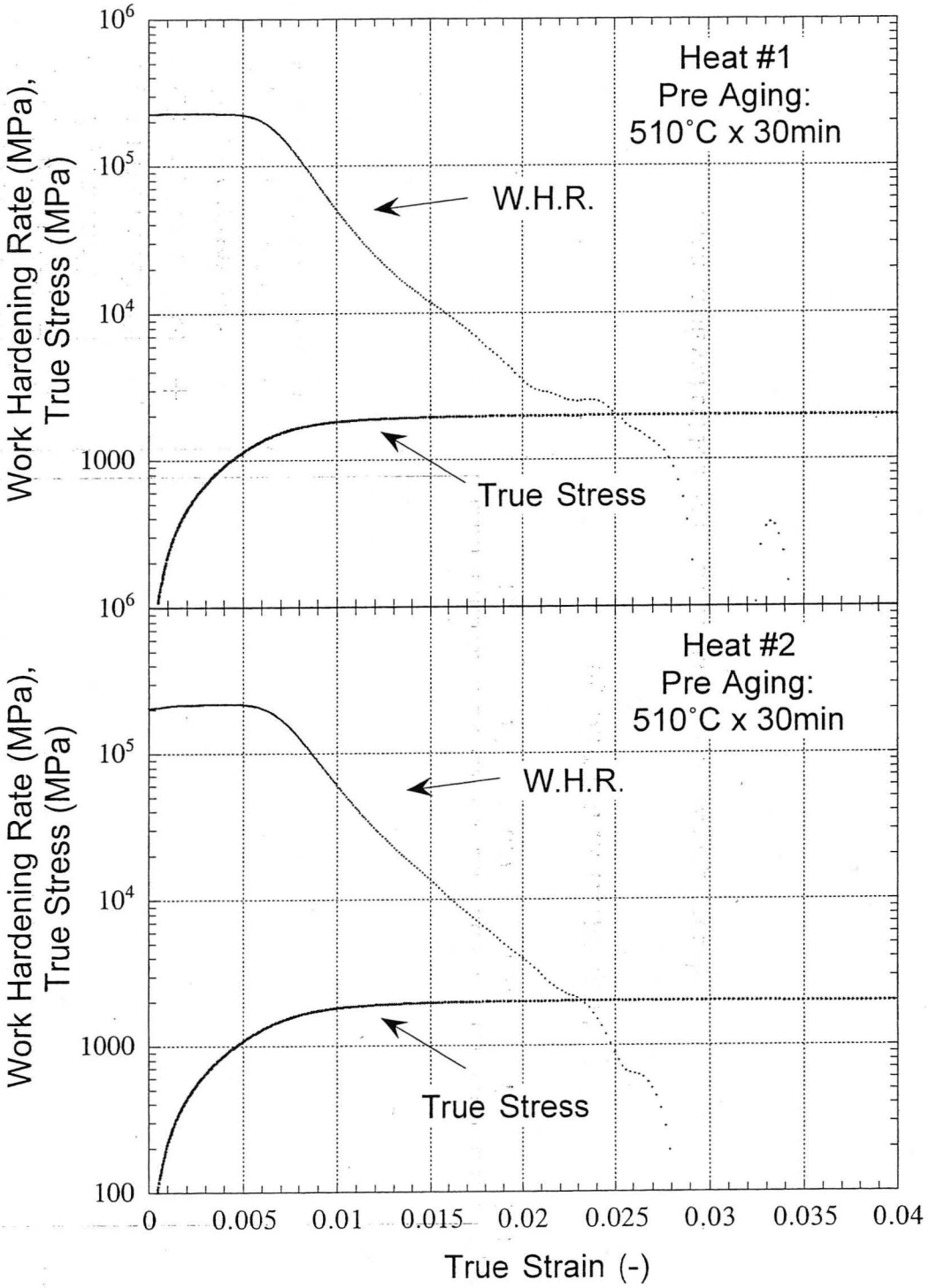

Figure 4.10 Effect of pre-aging on the work hardening rate – true strain curve.
Heat treatment: : (A)885°C x 1h, OQ + (DF)-197°C x 1h +
(PreAg)510°C x 30min, OQ + (DF)-197°C x 1h + (Ag) 482°C x 5h, OQ

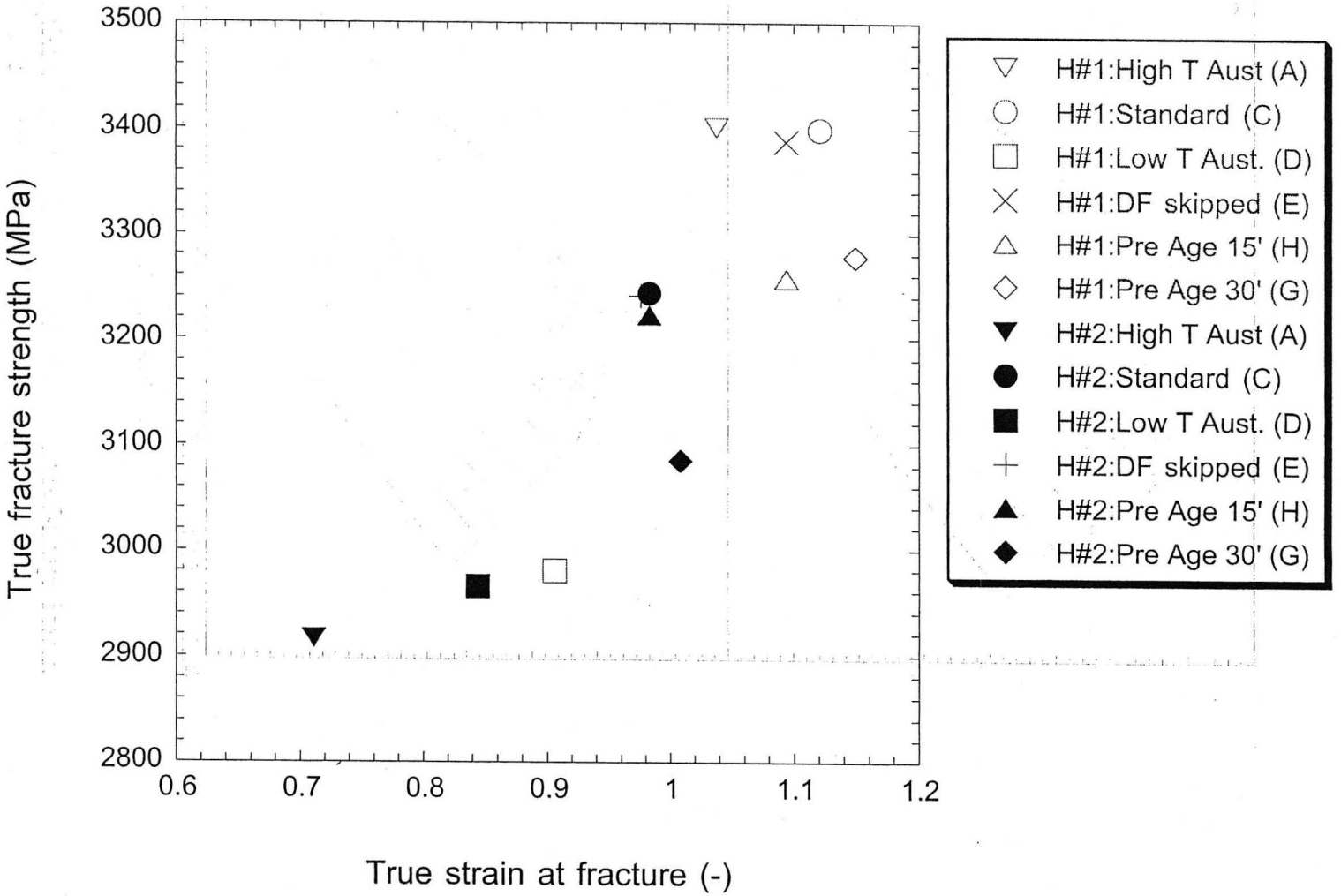

Figure 4.11 Relationship between true strain and true stress at the tensile fracture.

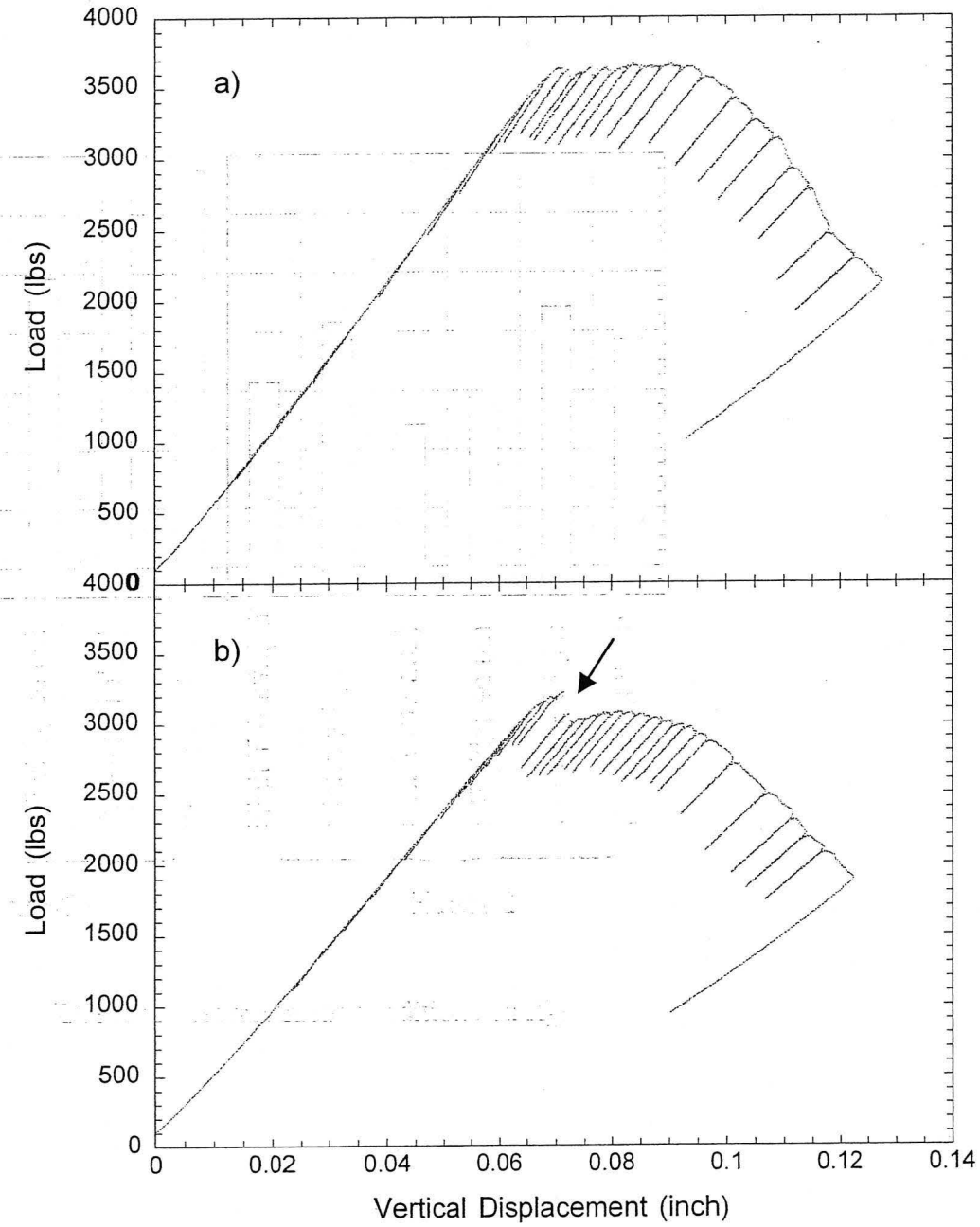

Figure 4.12 Examples of the load-displacement curves of the J-integral tests:
a) slow stable crack propagation, and
b) fast unstable crack propagation (marked by the arrow).

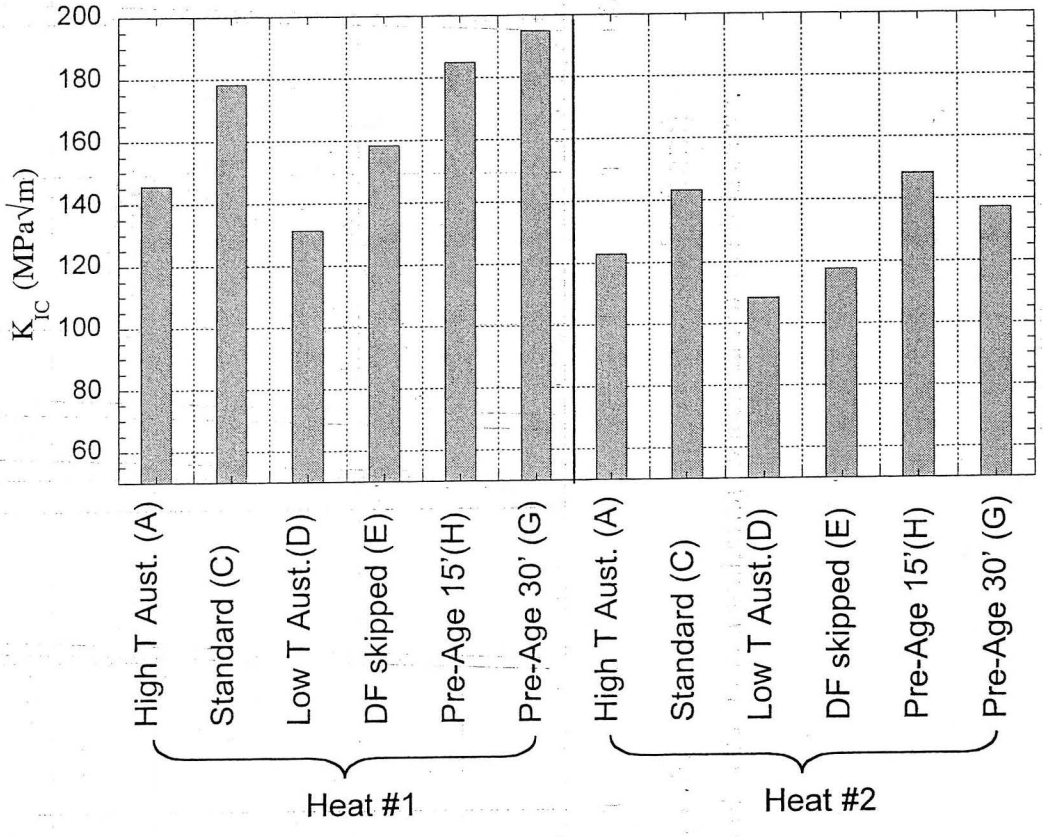

Figure 4.13 Effect of heat treatment conditions on K_{Ic}.

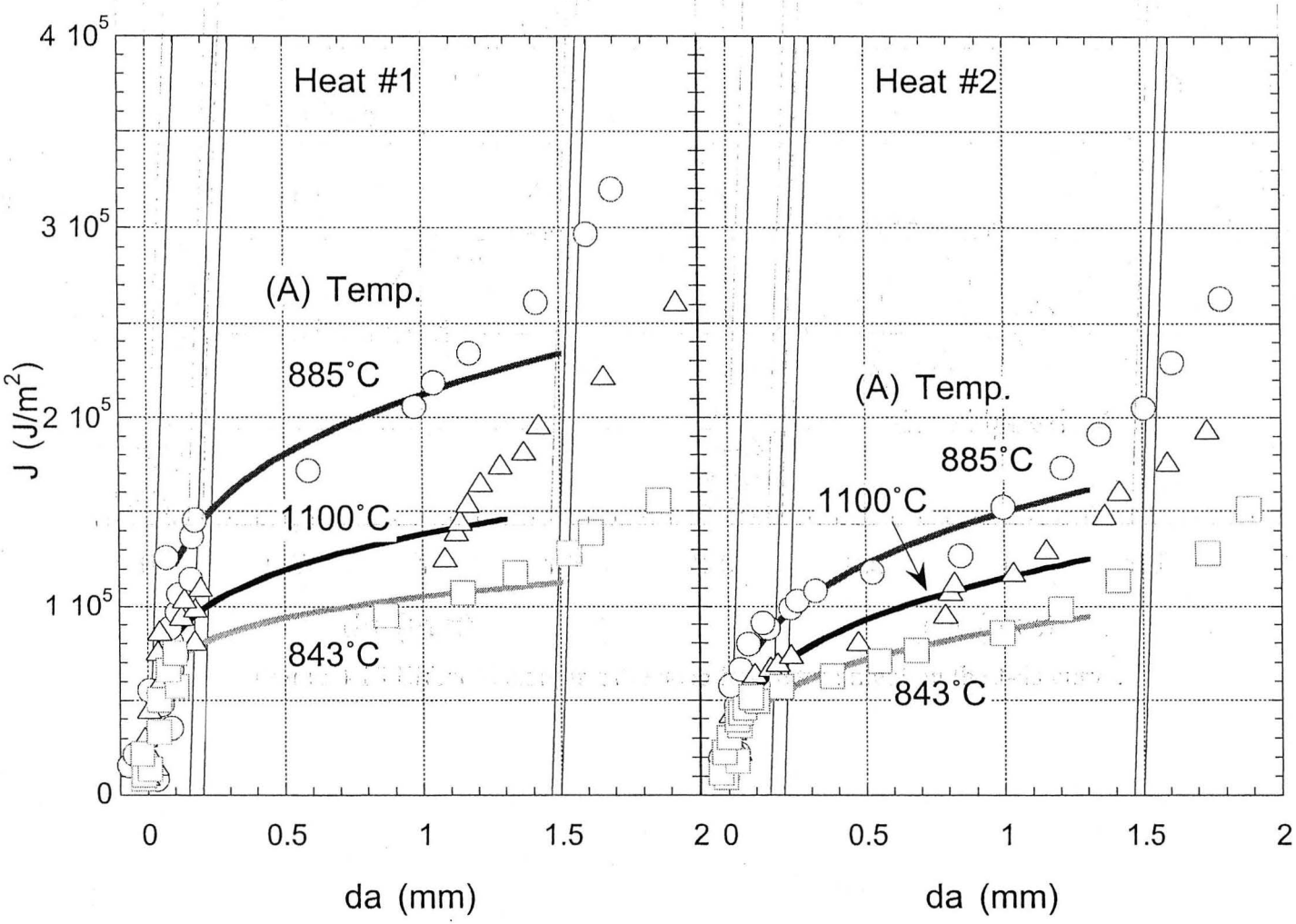

Figure 4.14 Effect of austenitizing temperature on the J-da curve.

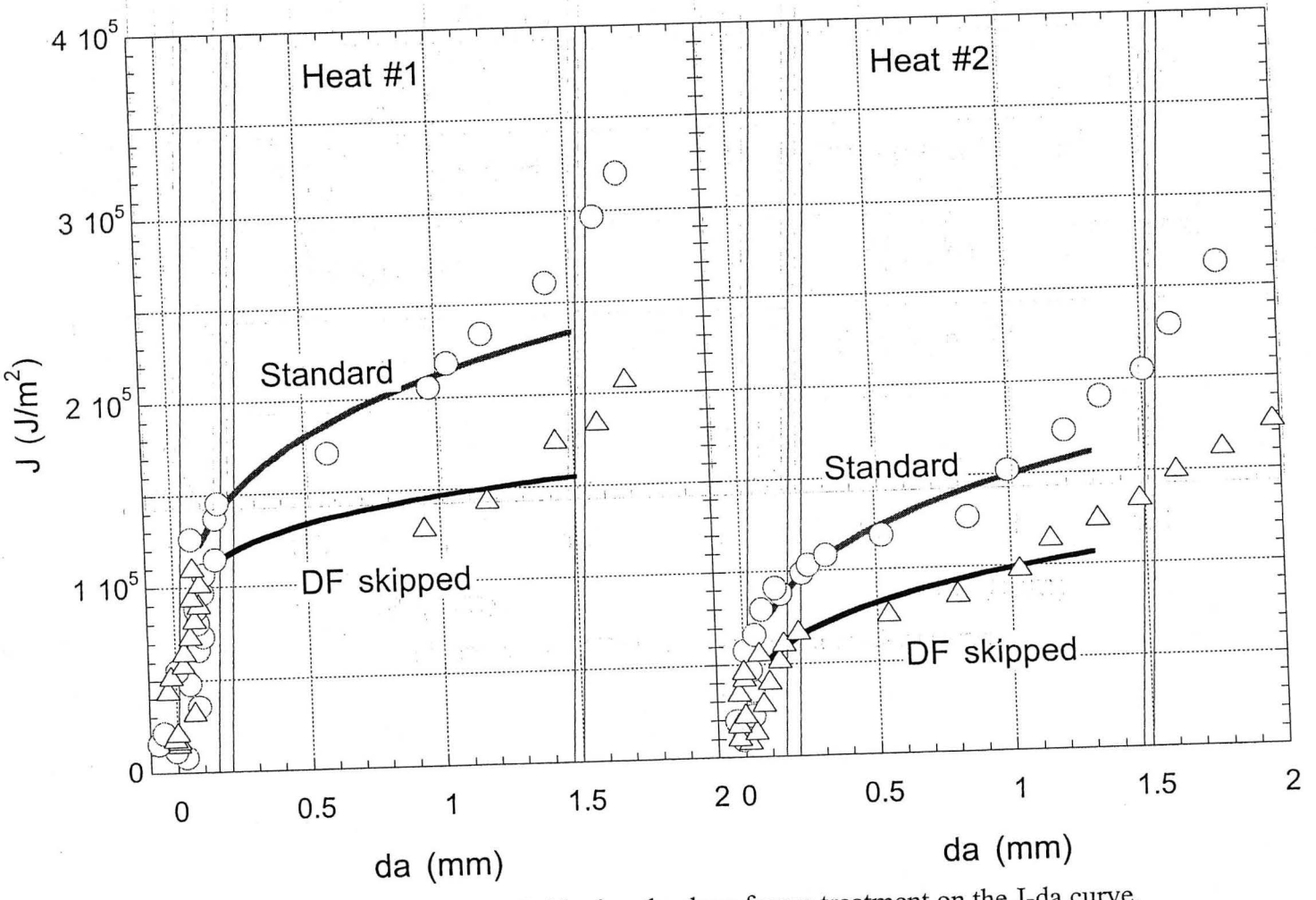

Figure 4.15 Effect of skipping the deep freeze treatment on the J-da curve.

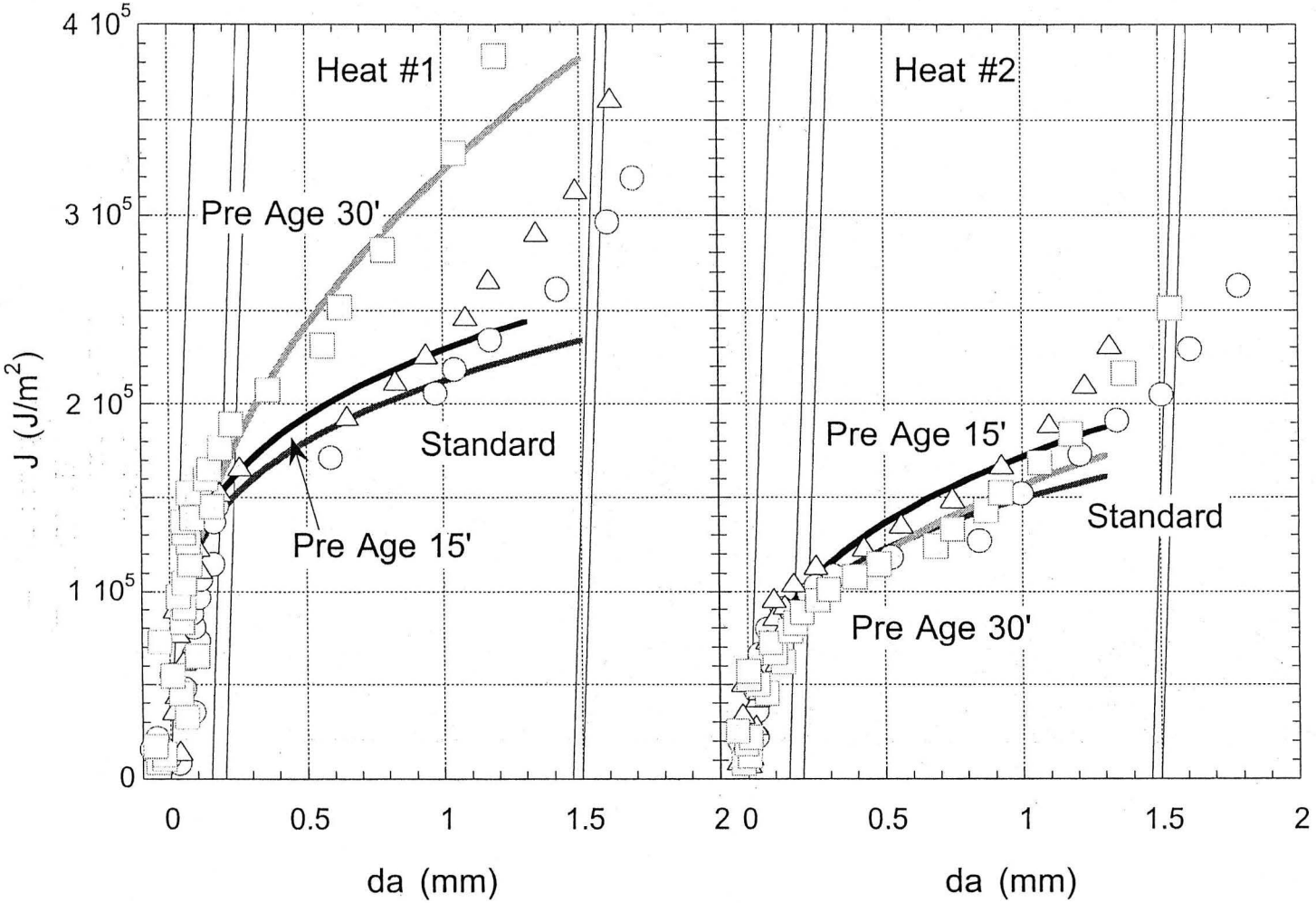

Figure 4.16 Effect of pre-aging on the J-da curve.

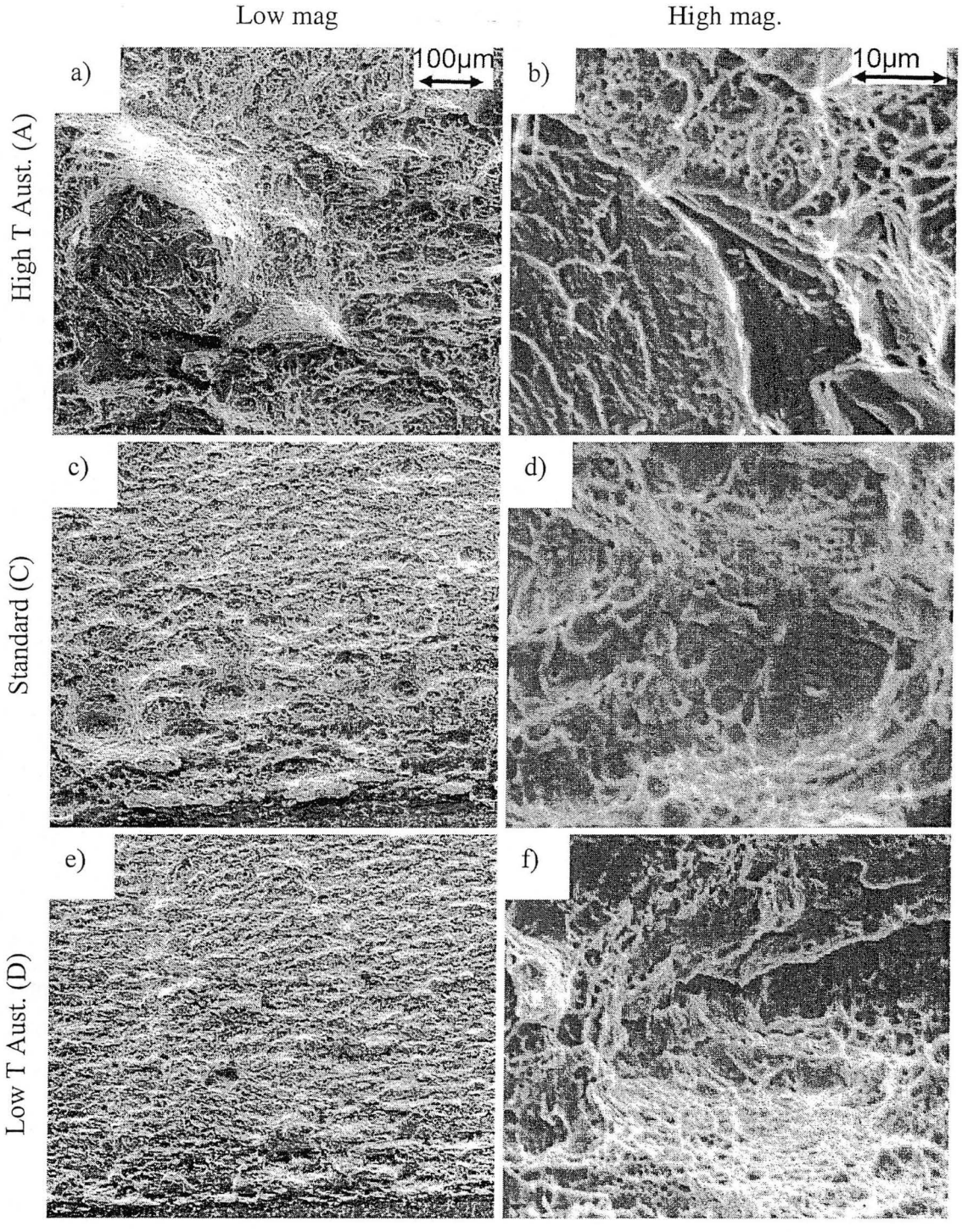

Figure 4.17 SEM fractographs of the J-integral specimens of Heat #1.
Cracks propagate from the bottom to the top of the images.
a), b) High T Aust. (A) /145.8MPa$\sqrt{m}$, c), d), Standard (C) /178.2MPa$\sqrt{m}$,
e), f) Low T Aust. (D) /131.3MPa$\sqrt{m}$, continued to the next page →

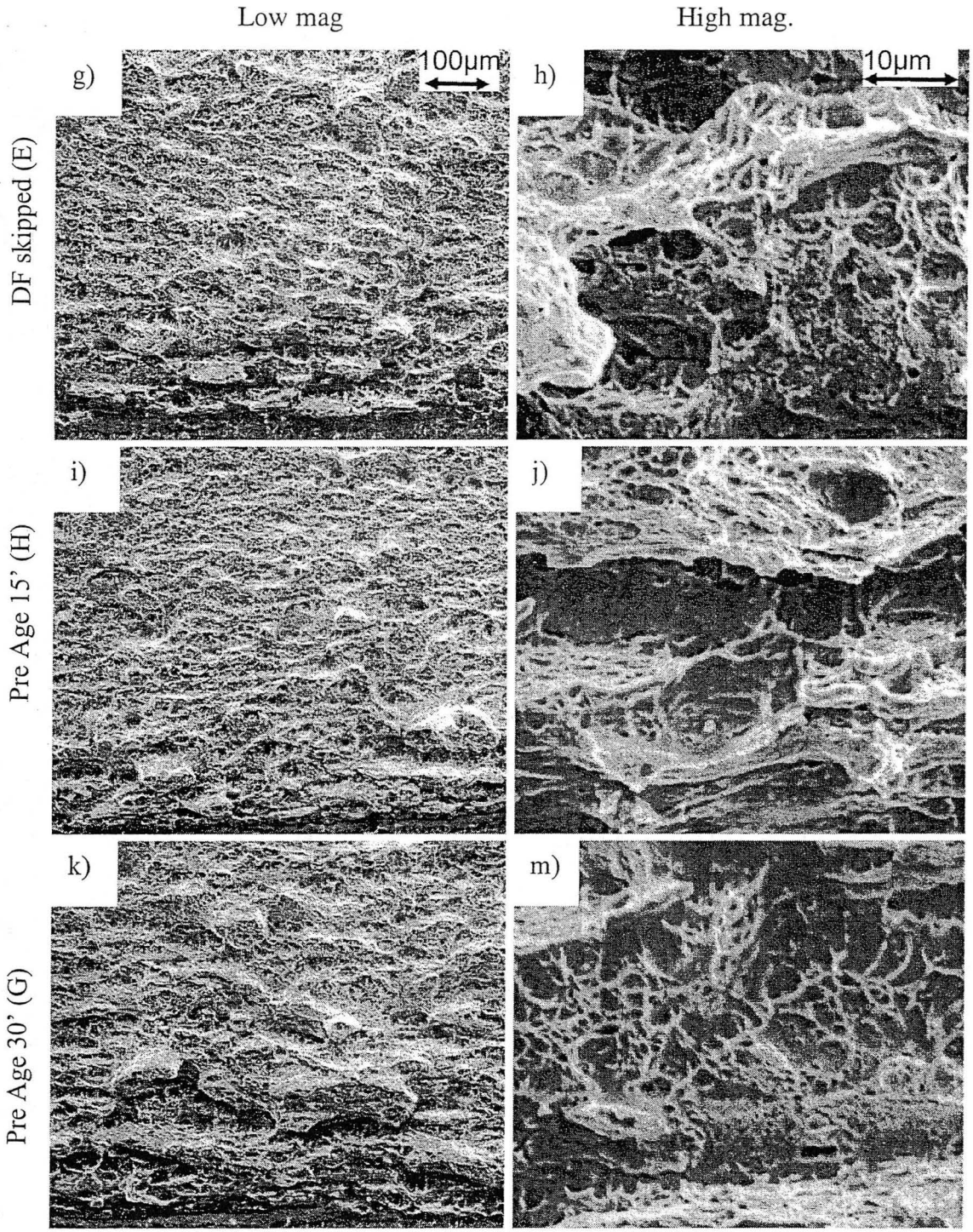

Figure 4.17 SEM fractographs of the J-integral specimens of Heat #1.
Cracks propagate from the bottom to the top of the images.
g), h) DF skipped (E) /158.5MPa√m, i), j), Pre Age 15' (H) /184.8MPa√m, and
k), m) Pre Age 30' (G) /194.9MPa√m. ←continued from the previous page

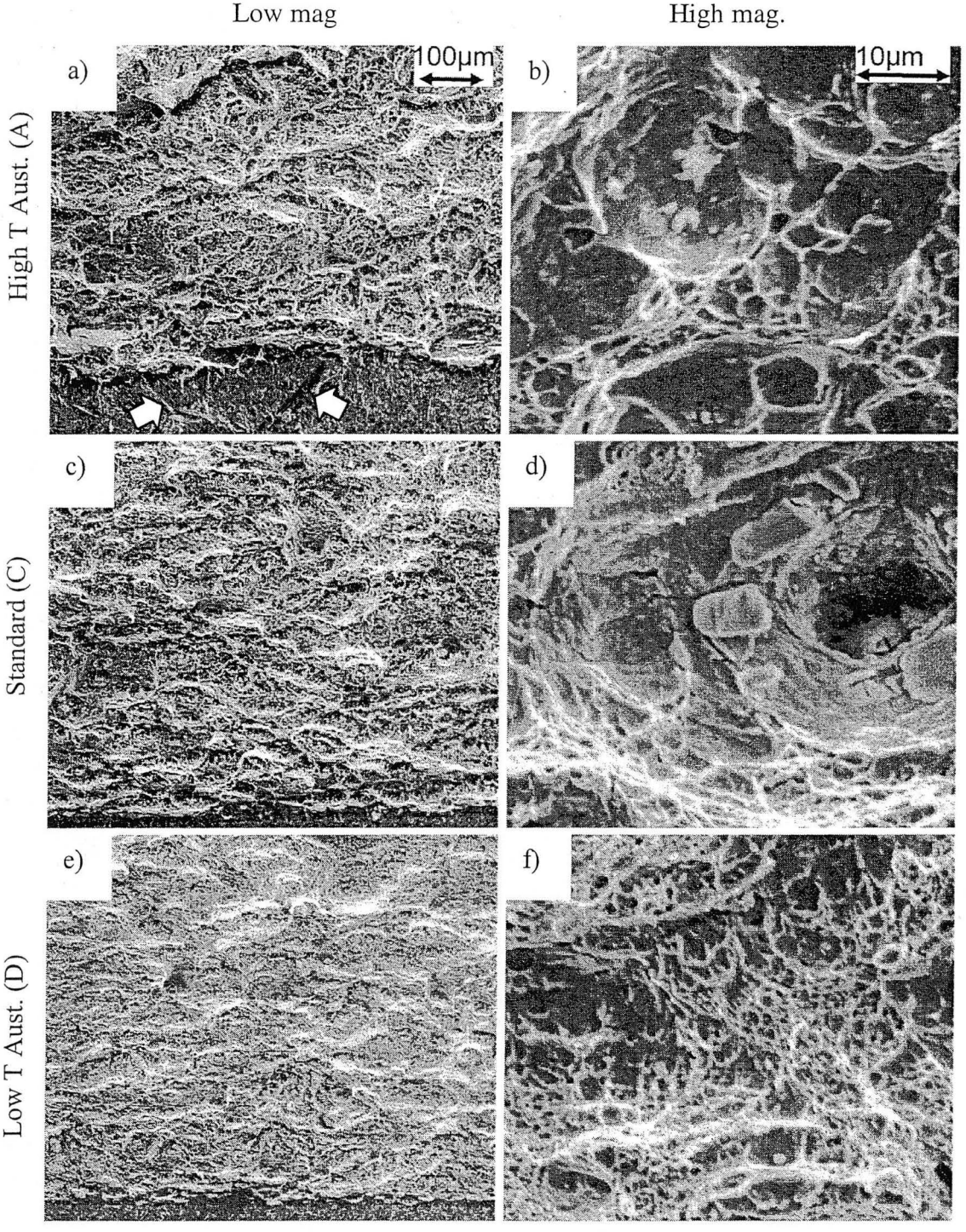

Figure 4.18 SEM fractographs of the J-integral specimens of Heat #2.
Cracks propagate from the bottom to the top of the images.
a), b) High T Aust. (A) / 122.8MPa√m, c), d), Standard (C) / 143.3MPa√m,
e), f) Low T Aust. (D) / 108.4MPa√m, continued to the next page →

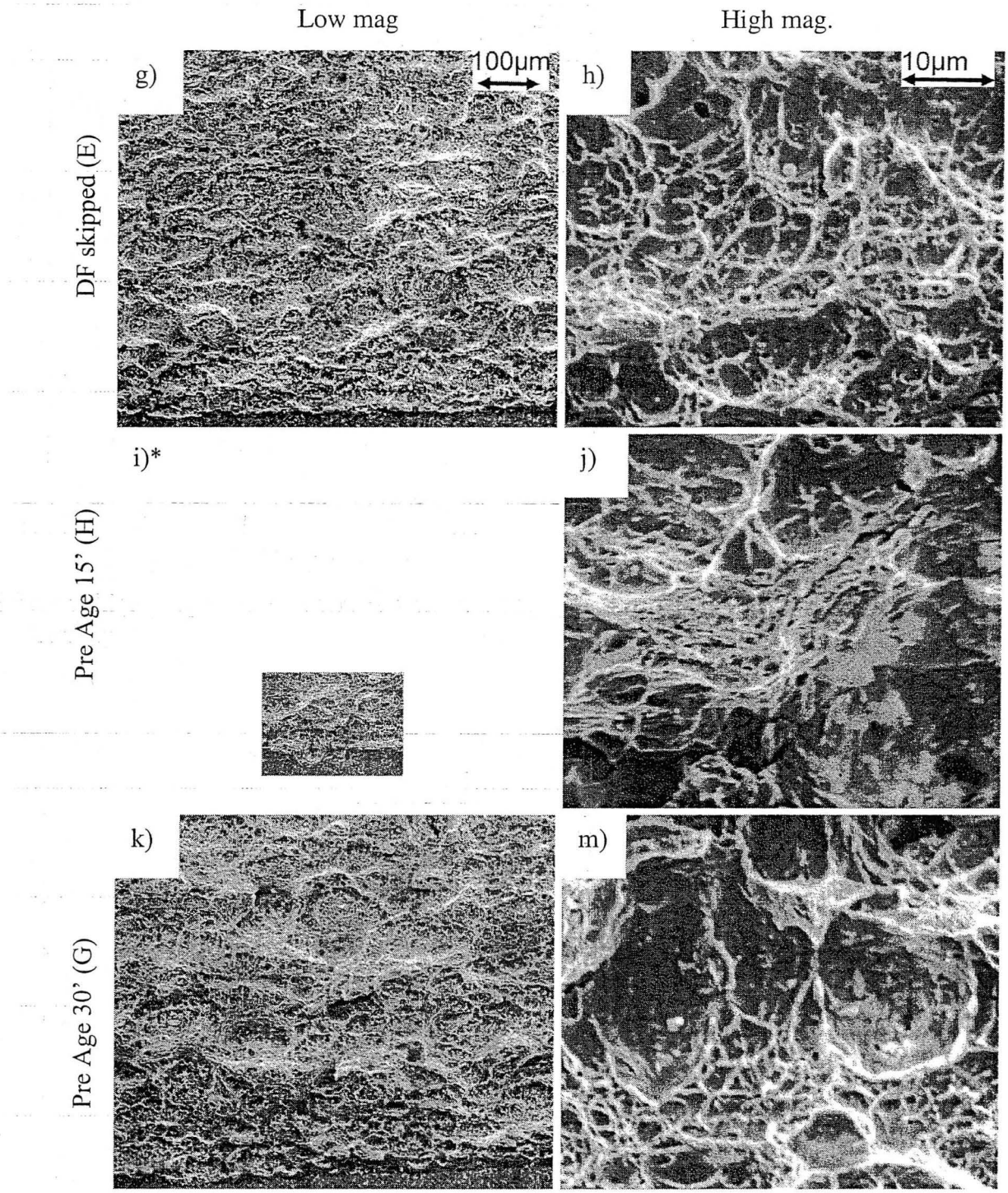

Figure 4.18 SEM fractographs of the J-integral specimens of Heat #2
Cracks propagate from the bottom to the top of the images.
g), h) DF skipped (E) /117.6MPa√m, i), j), Pre Age 15' (H) /148.4MPa√m, and
k), m) Pre Age 30' (G) /137.1MPa√m. ←continued from the previous page
* Unfortunately, low mag. picture of sample (H) was not taken, but part of the low mag. picture is substituted by shrinking the size of medium mag. picture.

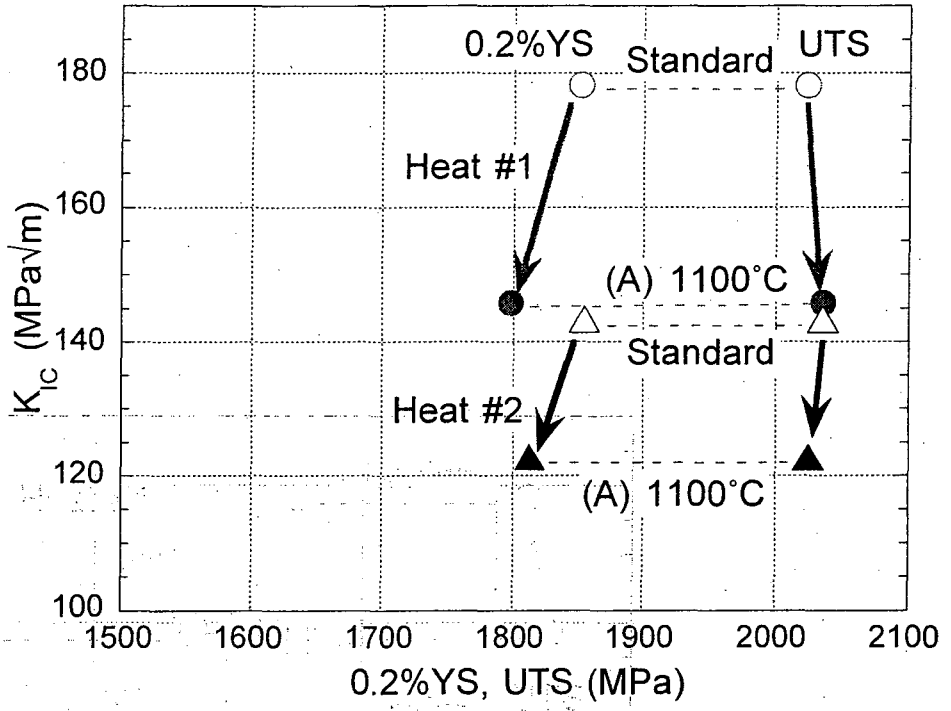

Figure 4.19 Effect of high temperature austenitization on the toughness-strength relationship.

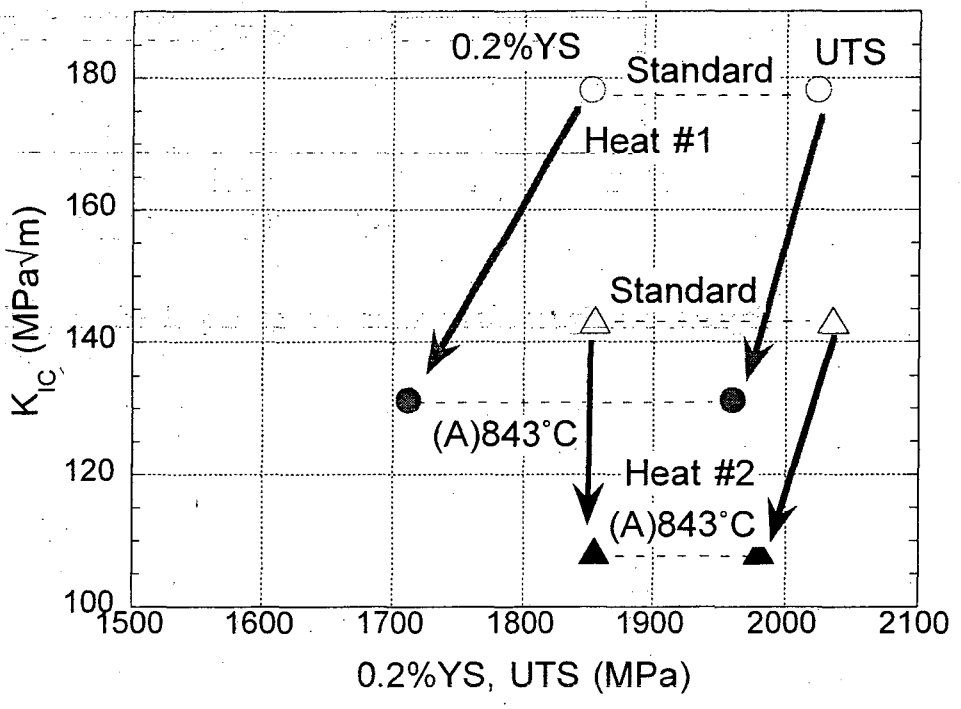

Figure 4.20 Effect of low temperature austenitization on the toughness-strength relationship.

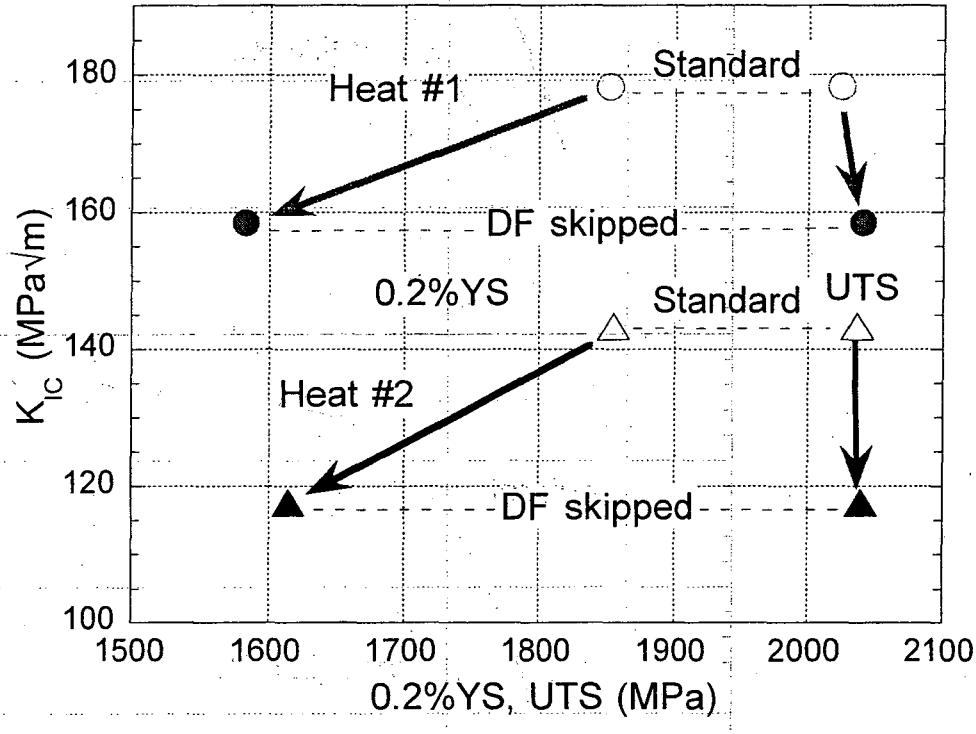

Figure 4.21 Effect of skipping the deep freeze treatment on the toughness-strength relationship.

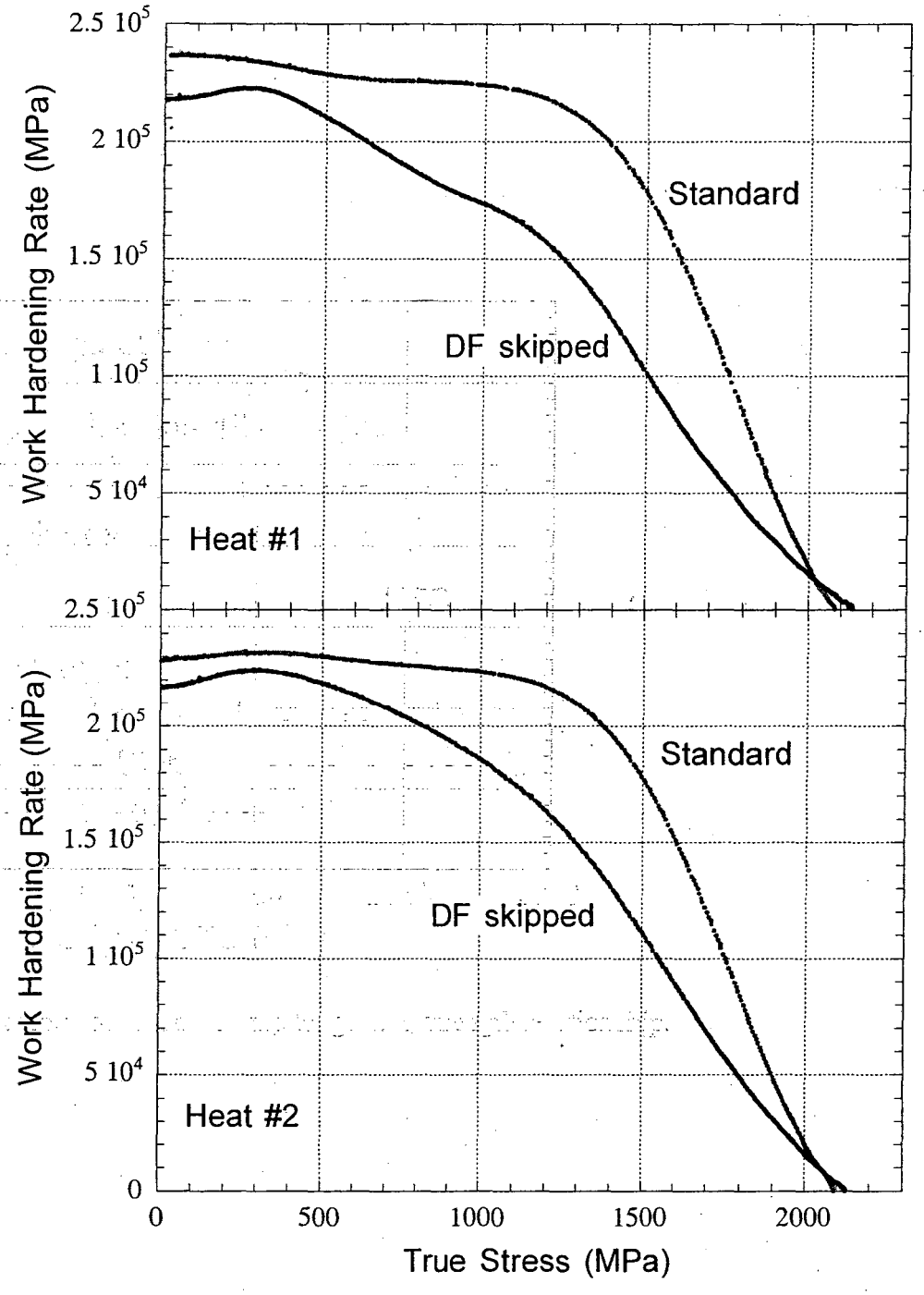

Figure 4.22 Effect of skipping the deep freeze on the work hardening rate – true stress curve.

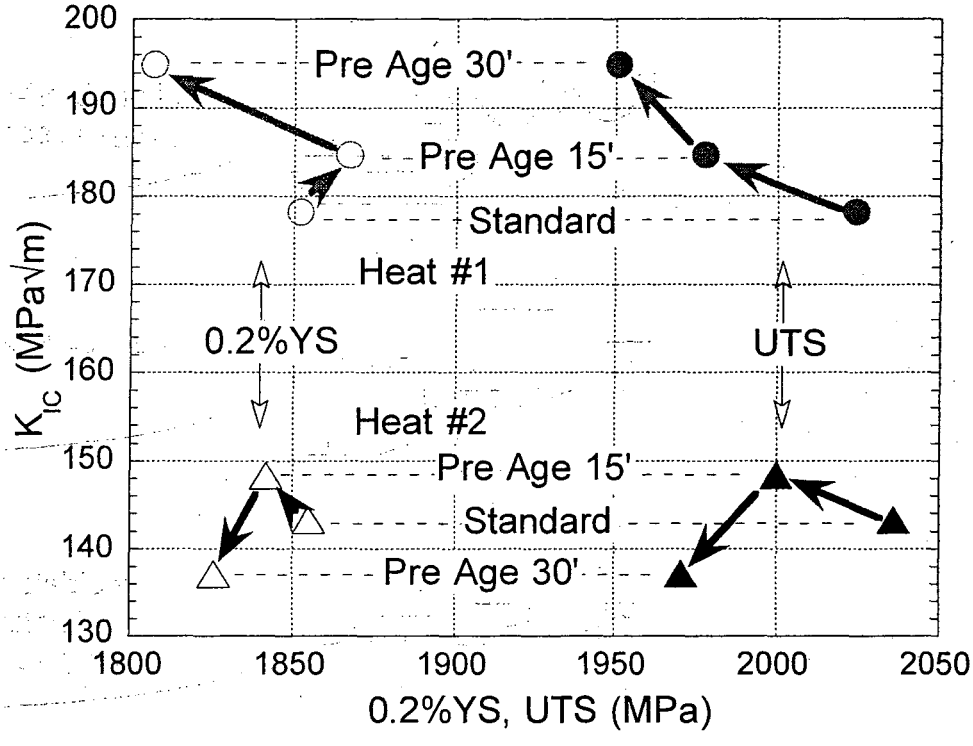

Figure 4.23 Effect of pre-aging conditions on the toughness-strength relationship.

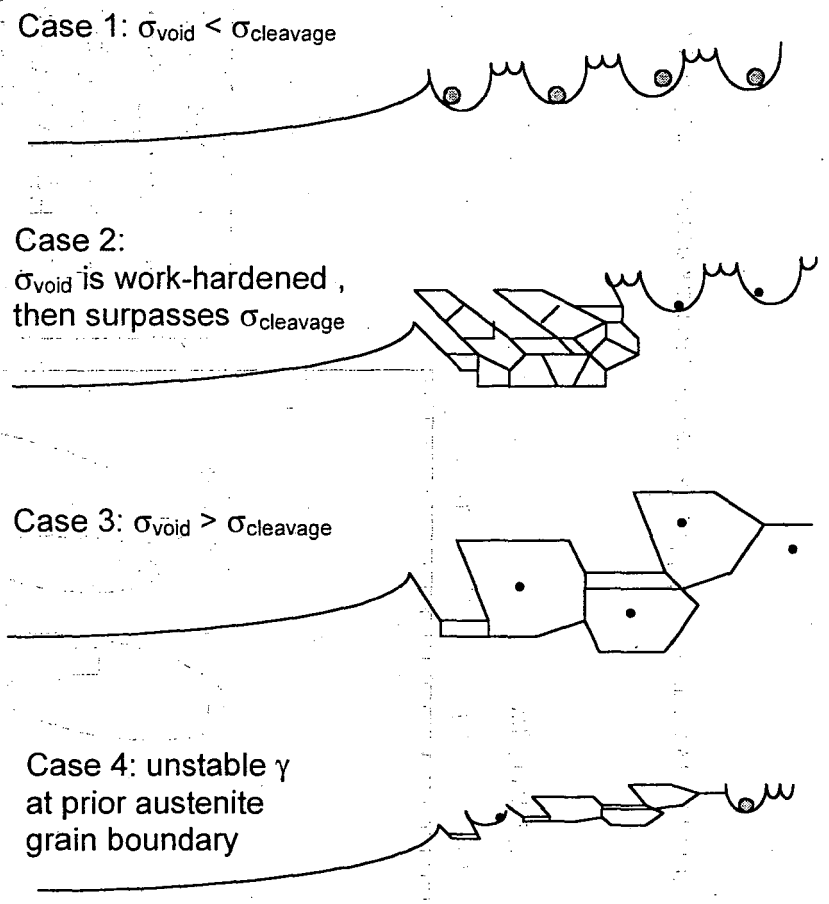

Figure 4.24 Schematic images of the fracture patterns.

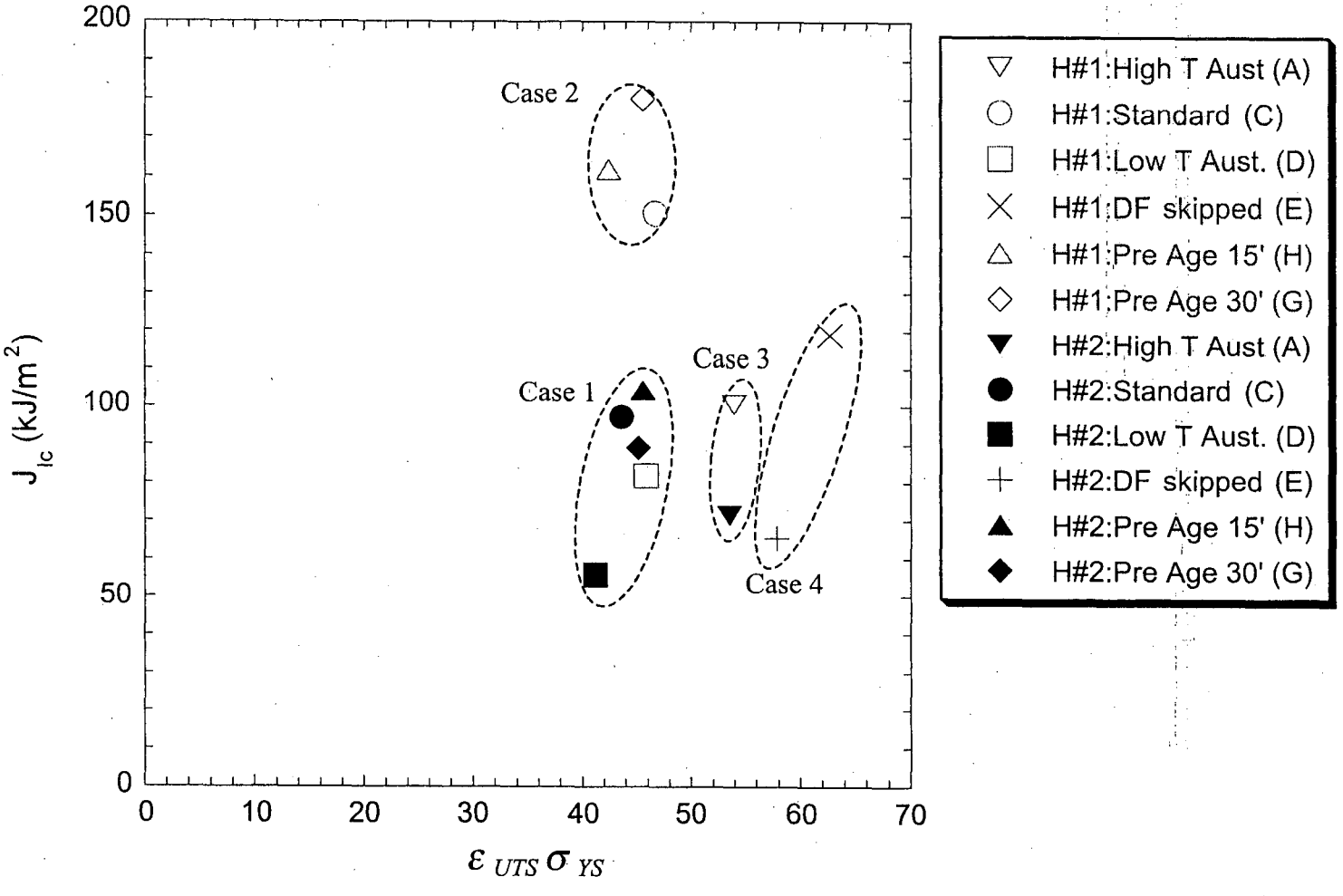

Figure 4.25 Relationship between J_{Ic} and $\varepsilon_{UTS}\,\sigma_{YS}$: strain at UTS and 0.2%YS are substituted for ε_f and σ_0, respectively.

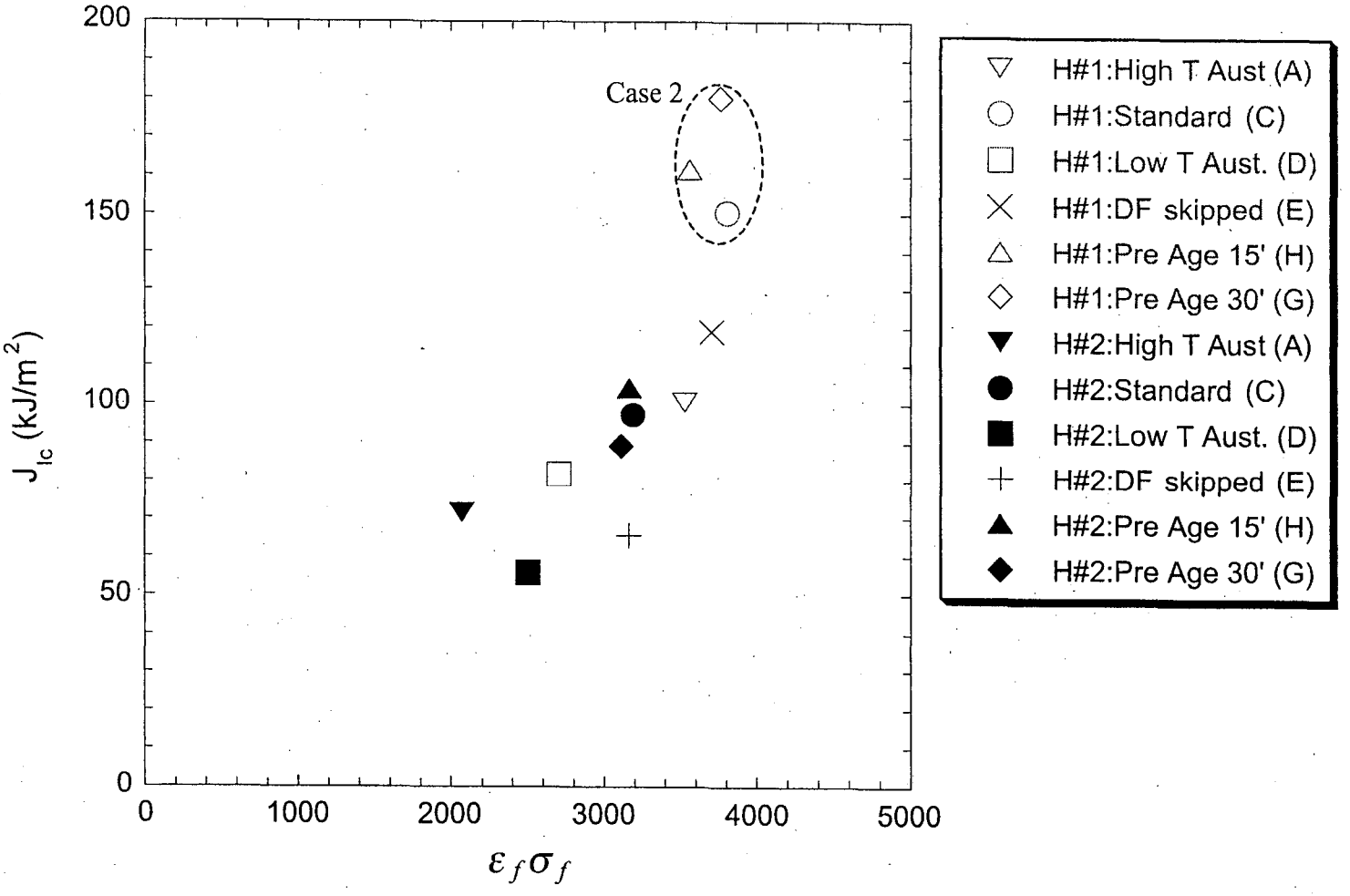

Figure 4.26 Relationship between J_{IC} and $\varepsilon_f \sigma_f$: strain and stress at the tensile fracture are substituted for ε_f and σ_0, respectively.

APPENDIX

The engineering stress-engineering strain curves and the true stress – work hardening rate curves of chapter 4 are shown in Figures A1 to A12.

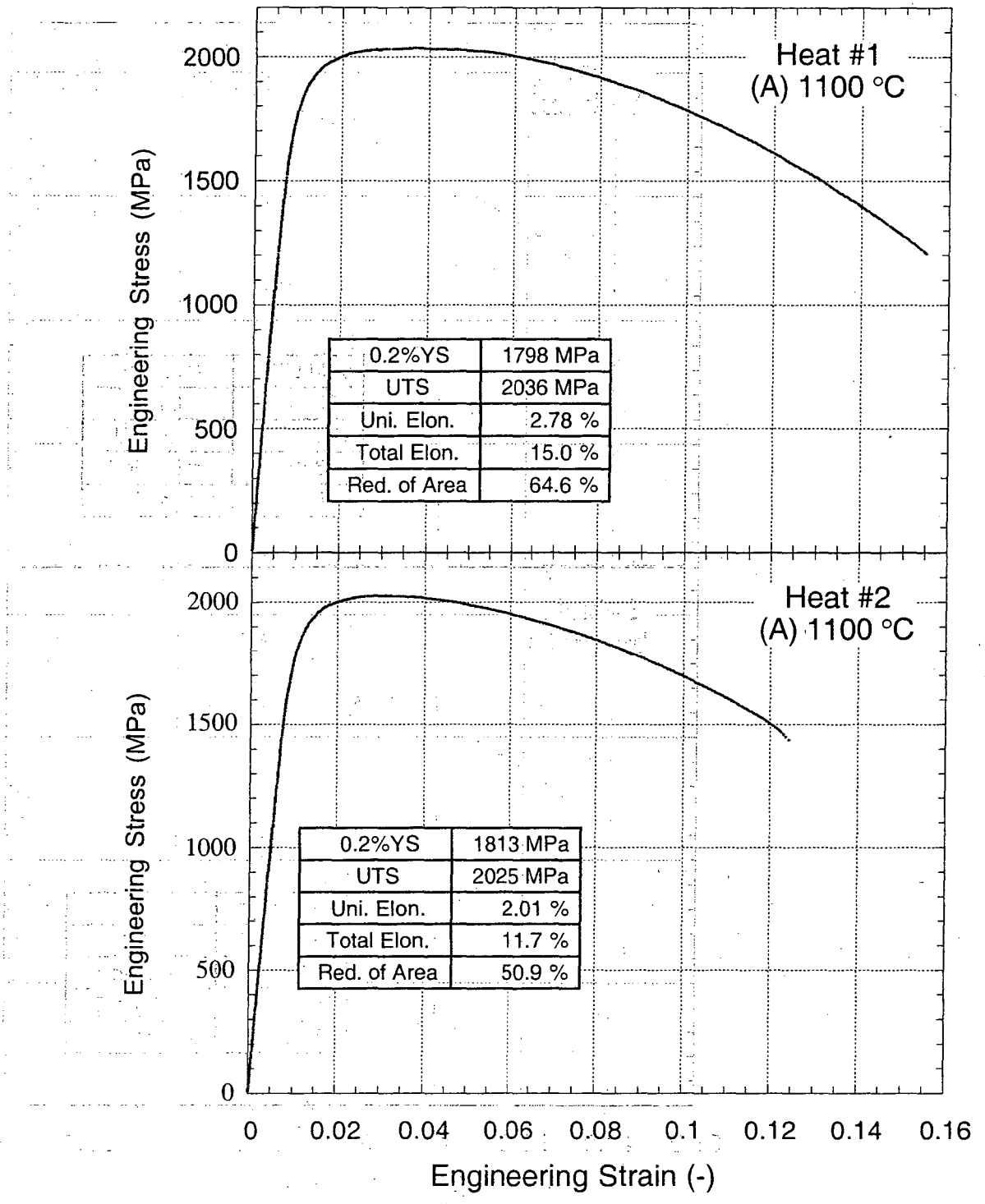

Figure A1 Effect of high temperature austenitization on the engineering stress – engineering strain curve
Heat treatment: (A) 1100°C x 1hr, OQ +(DF)-197°C x 1h + (Ag) 482°C x 5h, OQ

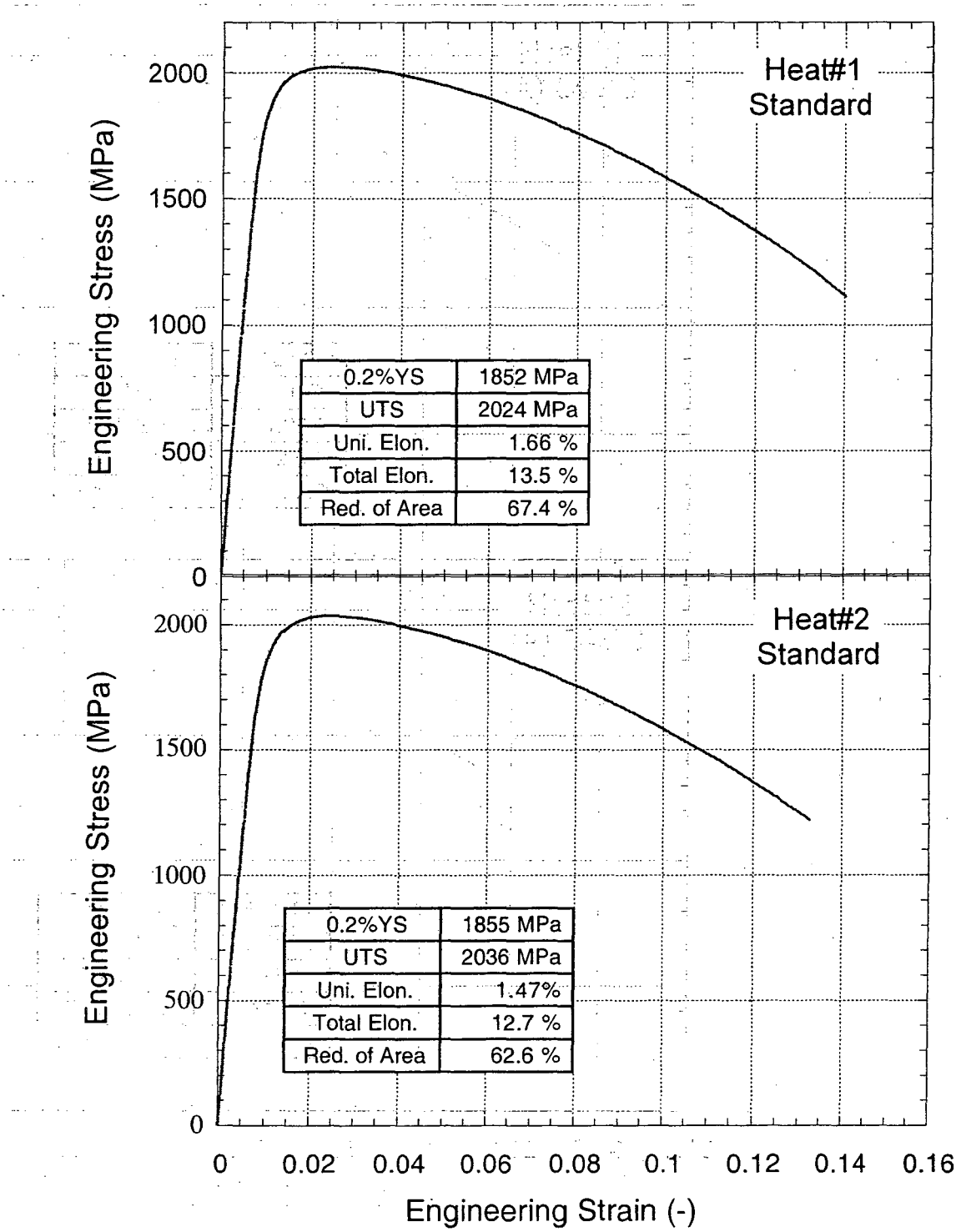

Figure A2 Engineering stress – engineering strain curve..
Standard heat treatment:
(A) 885°C x 1hr, OQ +(DF)-197°C x 1h + (Ag) 482°C x 5h, OQ

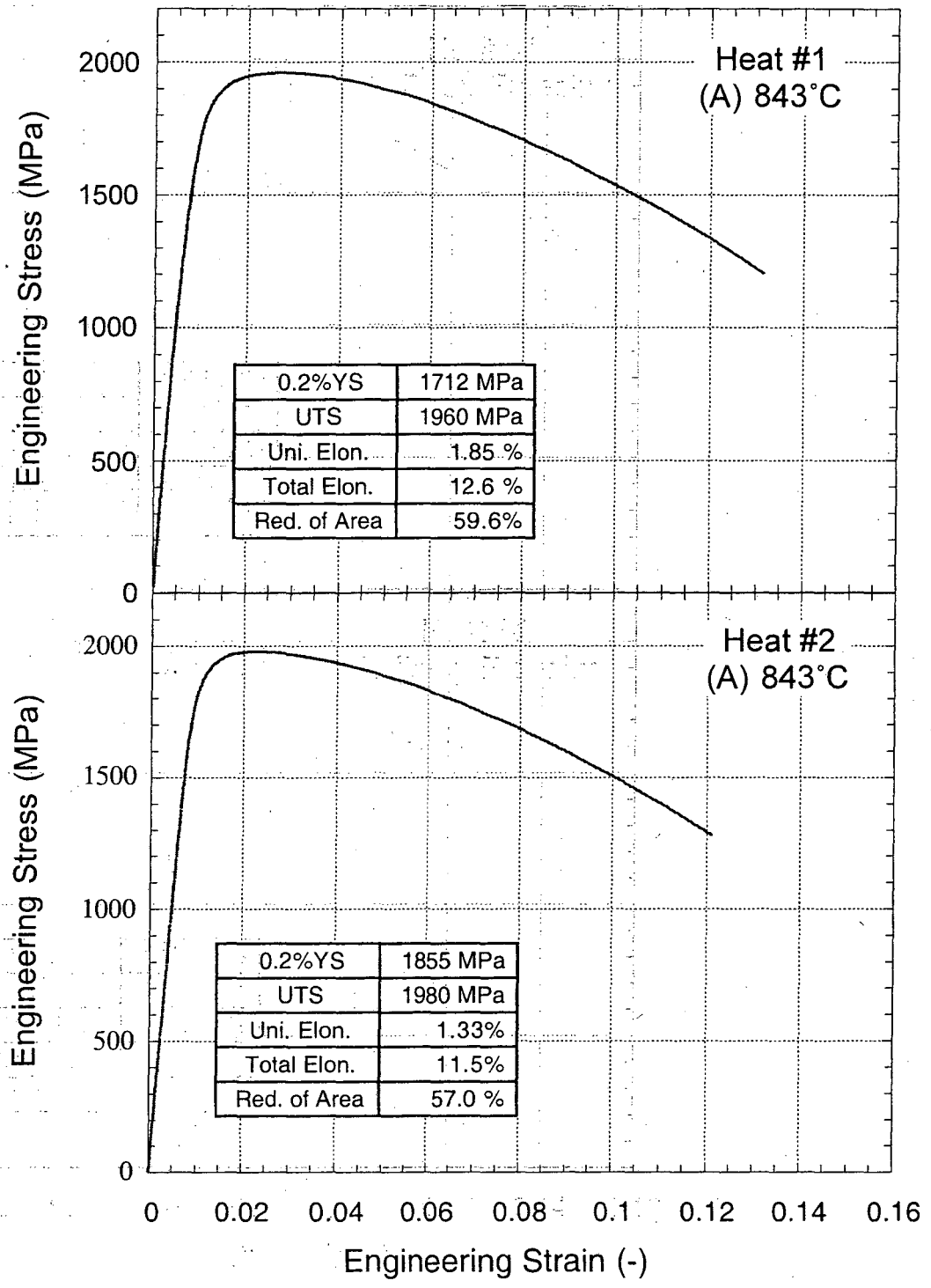

Figure A3 . Effect of low temperature austenitization on the engineering stress – engineering strain curve.
Heat treatment: (A) 843°C x 1hr, OQ +(DF)-197°C x 1h + (Ag) 482°C x 5h, OQ

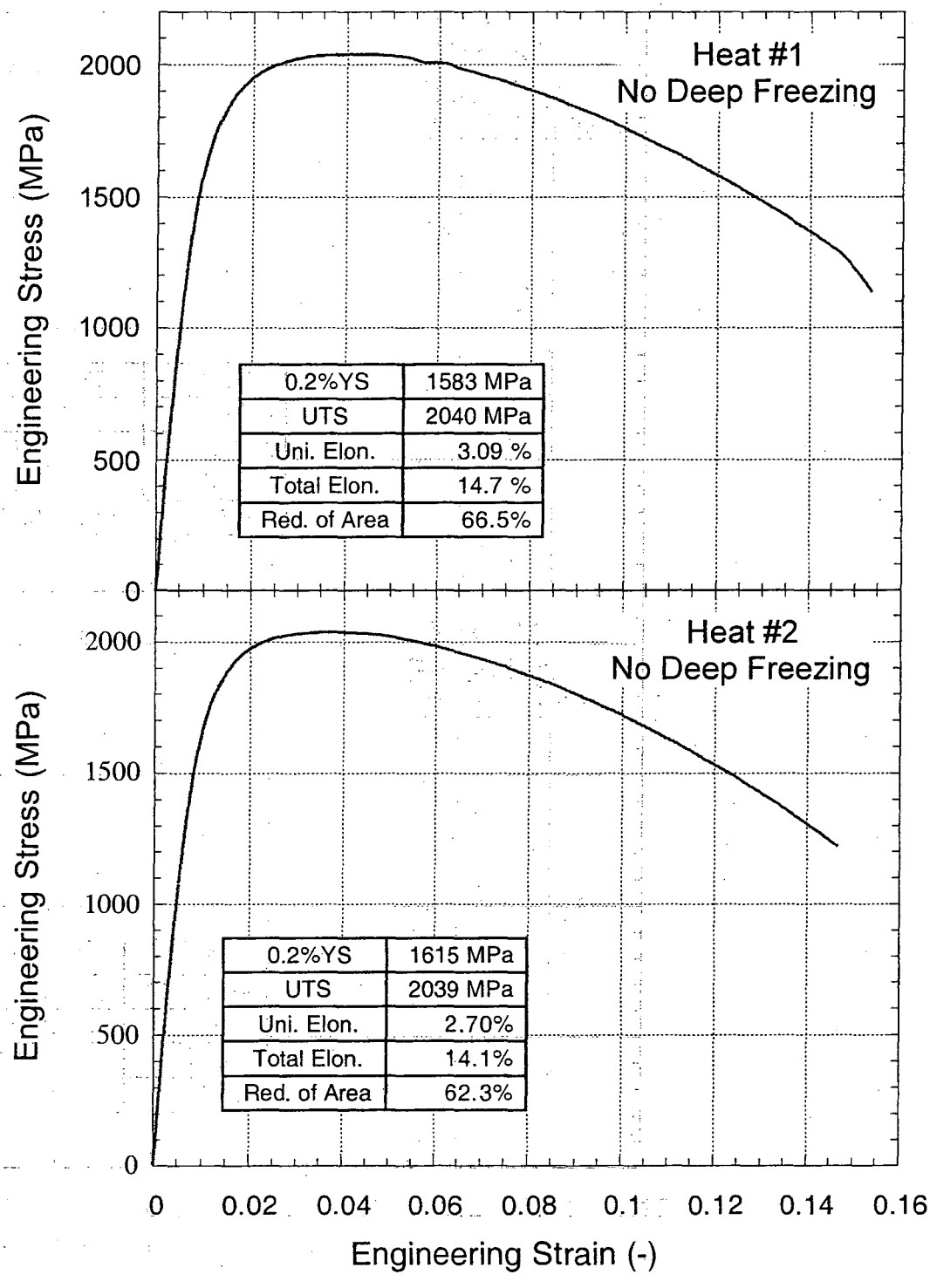

Figure A4 Effect of deep freezing on the engineering stress – engineering strain curve.
Heat treatment: (A) 885°C x 1hr, OQ + (Ag) 482°C x 5h, OQ

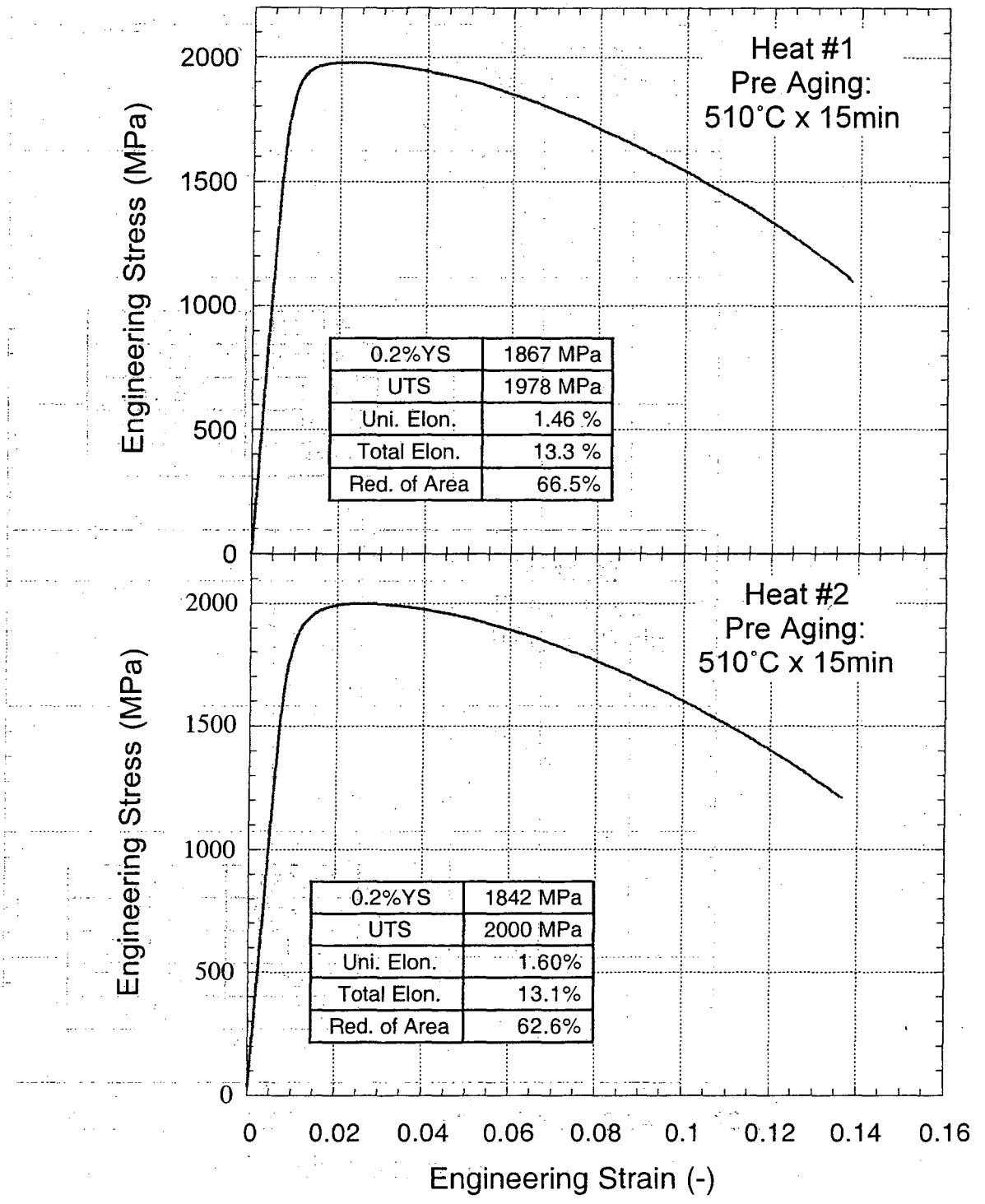

Figure A5 Effect of pre-aging on the engineering stress – engineering strain curve
Heat treatment: (A) 885°C x 1hr, OQ +(DF)-197°C x 1h +
(PreAg) 510°C x 15min, OQ + (DF)-197°C x 1h + (Ag) 482°C x 5h, OQ

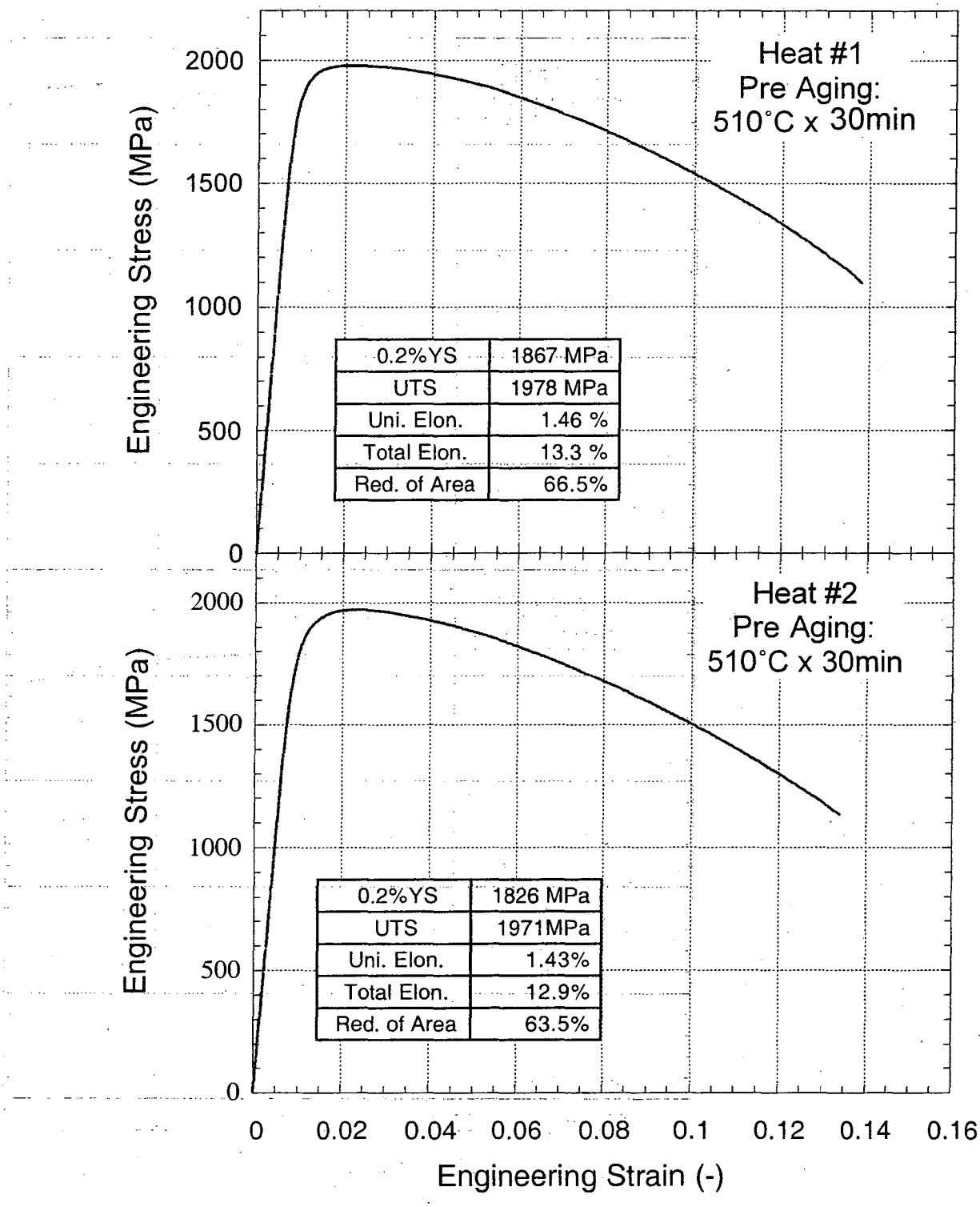

Figure A6 Effect of pre-aging on the engineering stress – engineering strain curve.
Heat treatment: (A) 885°C x 1hr, OQ +(DF)-197°C x 1h +
(PreAg) 510°C x 30min, OQ +(DF)-197°C x 1h + (Ag) 482°C x 5h, OQ

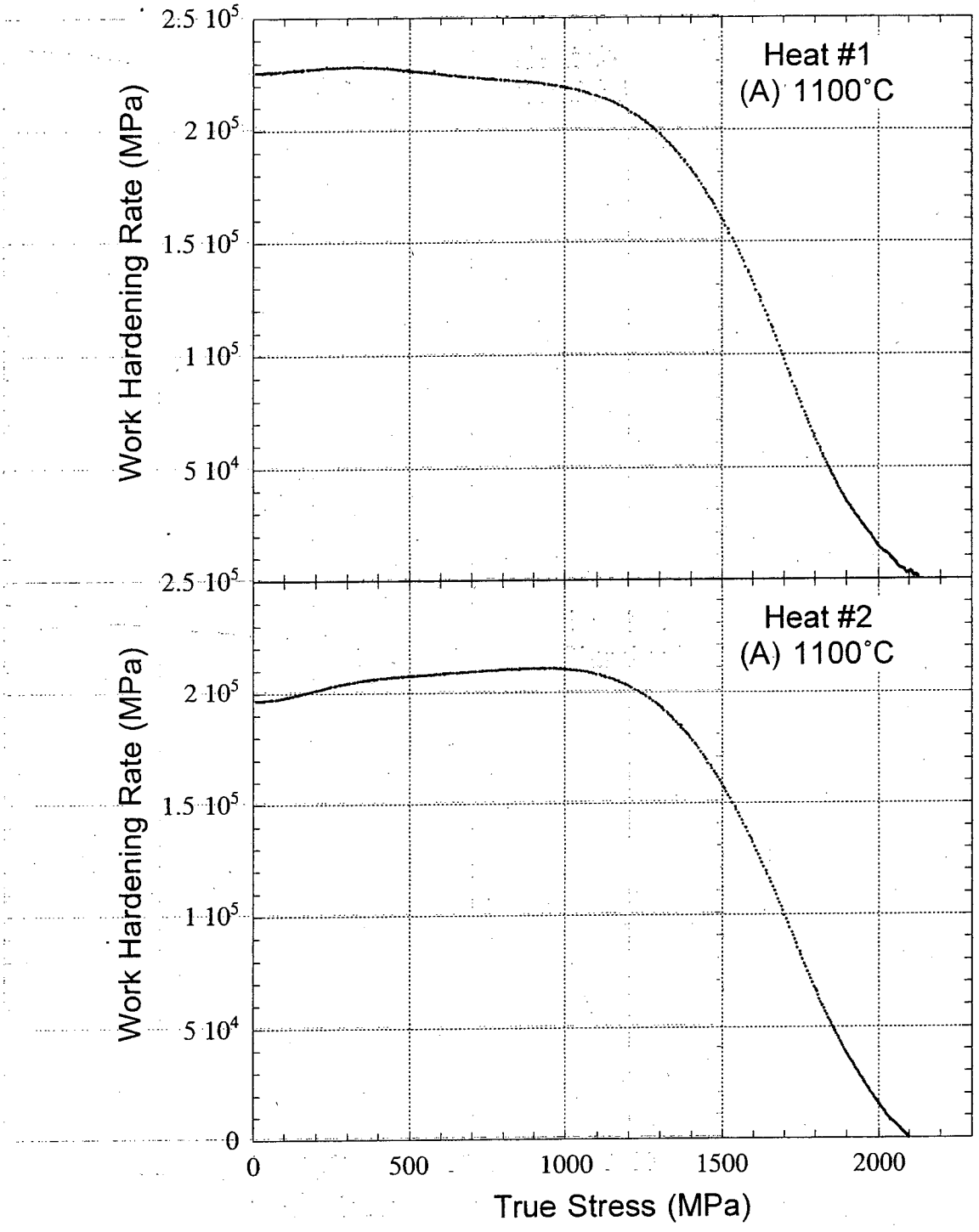

Figure A7 Effect of high temperature austenitization on the work hardening rate – true stress curve.
Heat treatment: (A) 1100°C x 1hr, OQ +(DF)-197°C x 1h + (Ag) 482°C x 5h, OQ

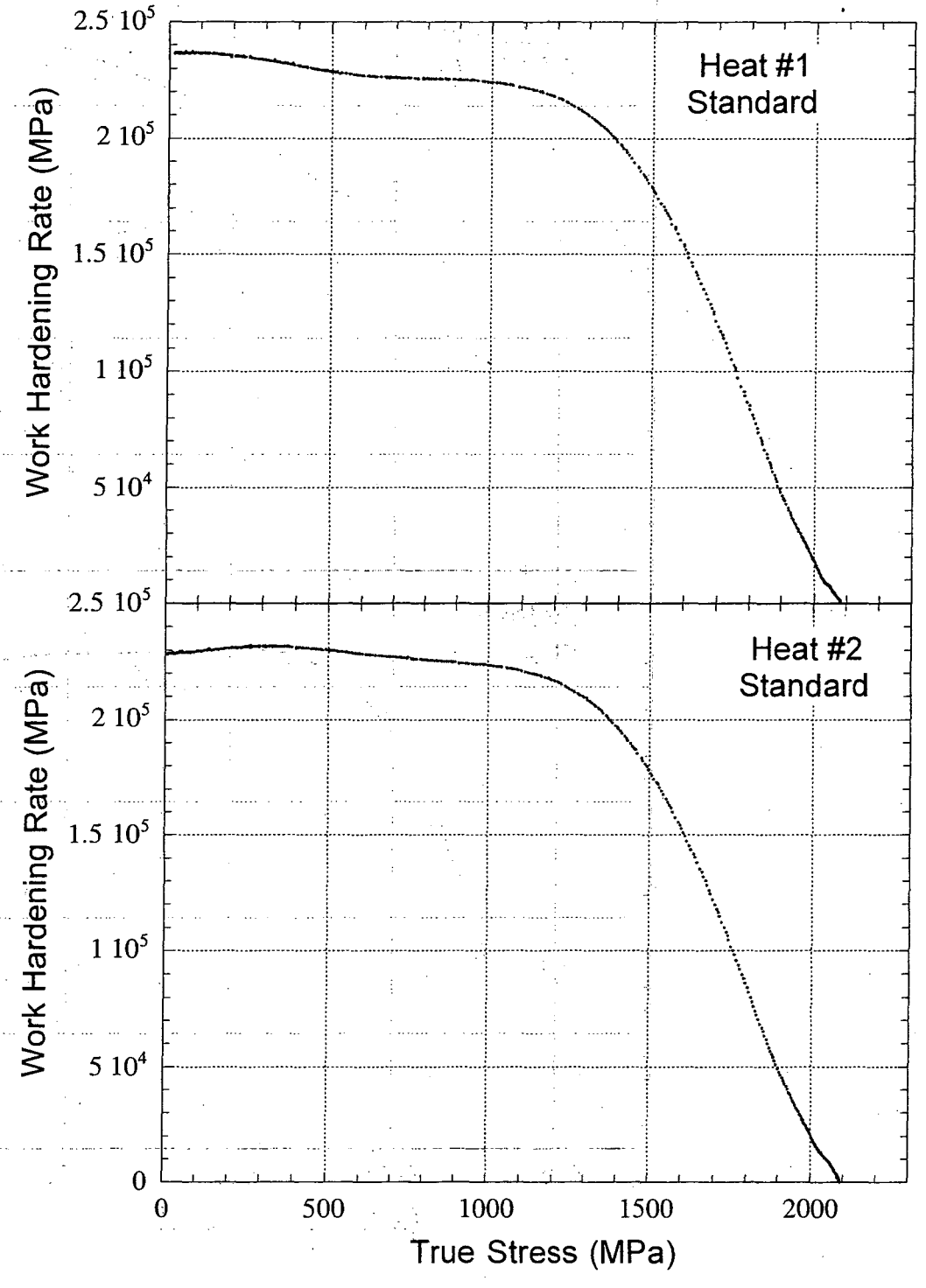

Figure A8 Work hardening rate – true stress curve.
Standard heat treatment:
(A) 885°C x 1hr, OQ +(DF)-197°C x 1h + (Ag) 482°C x 5h, OQ

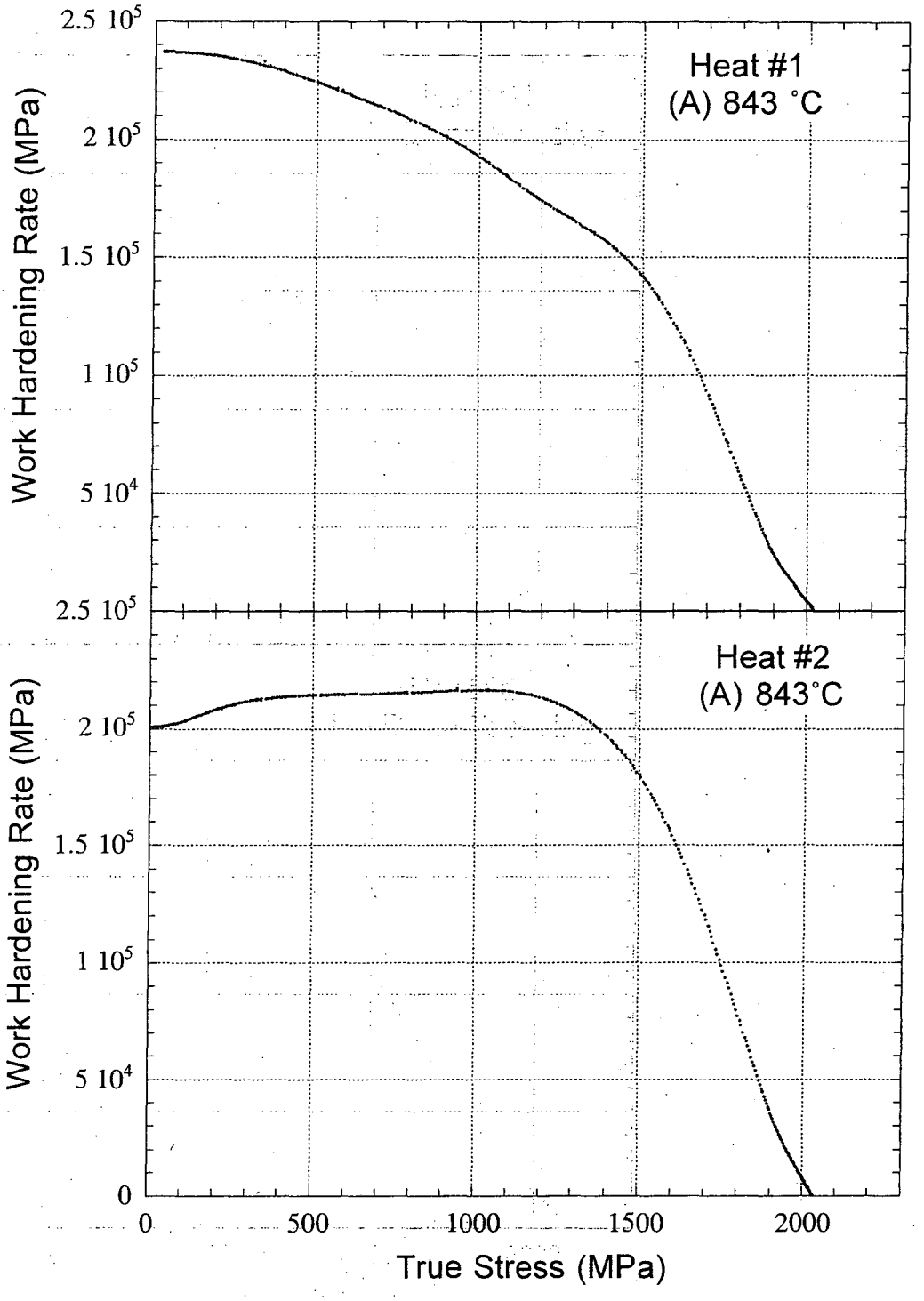

Figure A9 Effect of low temperature austenitization on the work hardening rate – true stress curve

Heat treatment: (A) 843°C x 1hr, OQ +(DF)-197°C x 1h + (Ag) 482°C x 5h, OQ

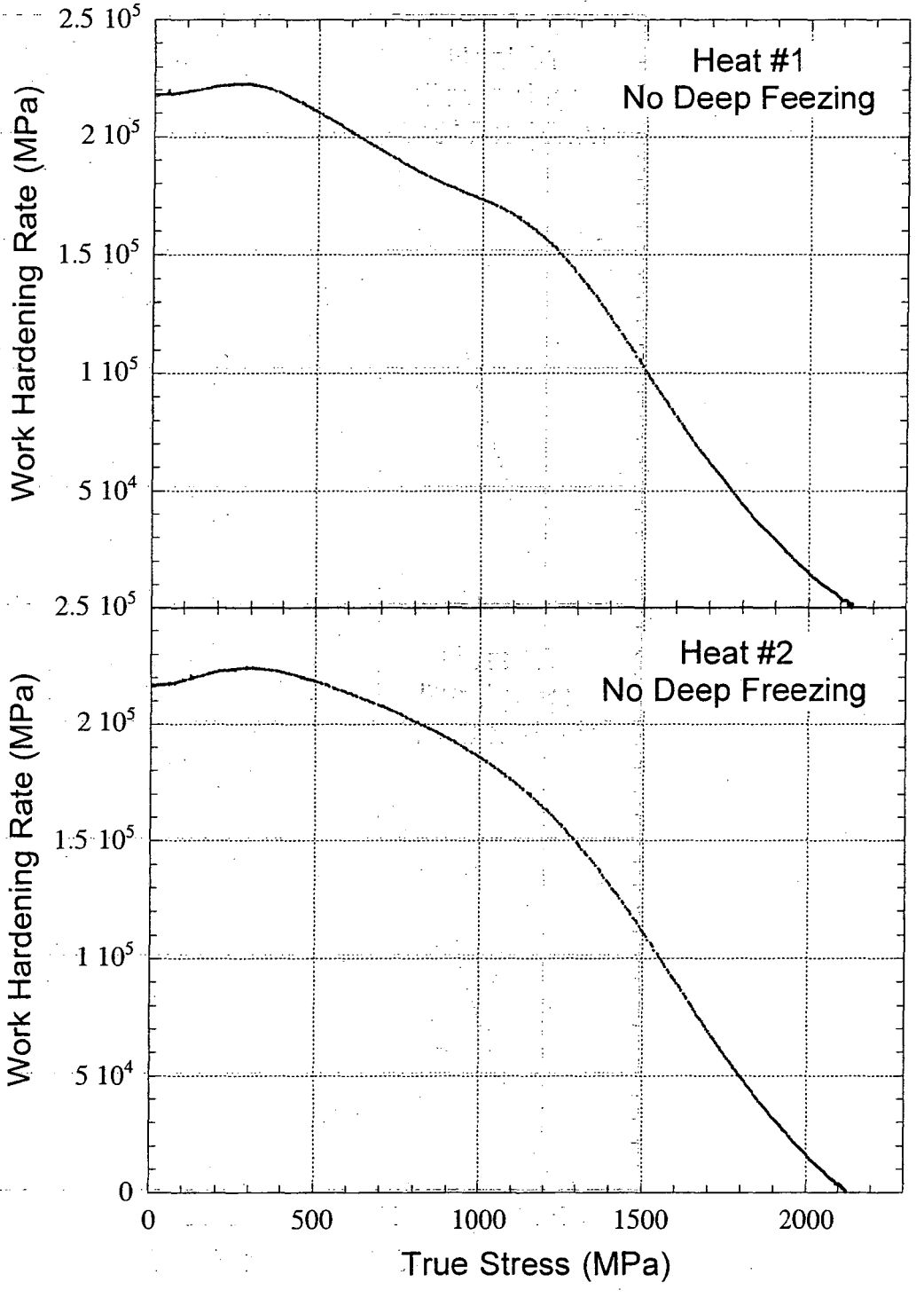

Figure A10 Effect of skipping the deep freeze on the work hardening rate – true stress curve
Heat Treatment: (A) 885°C x 1hr, OQ + (Ag) 482°C x 5h, OQ

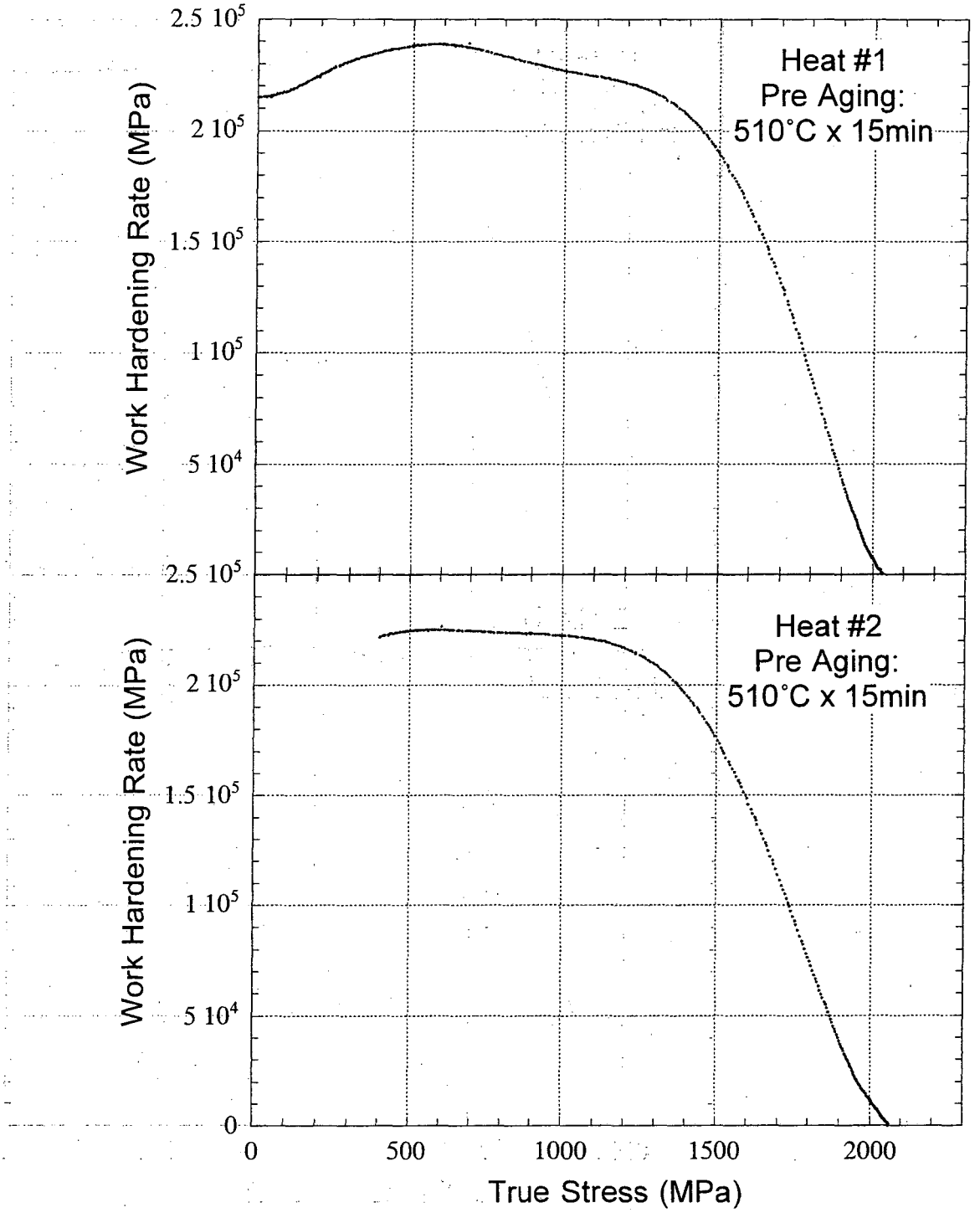

Figure A11 Effect of pre-aging on the work hardening rate – true stress curve.
Heat treatment: (A) 885°C x 1hr, OQ +(DF)-197°C x 1h +
(PreAg) 510°C x 15min, OQ + (DF)-197°C x 1h + (Ag) 482°C x 5h, OQ

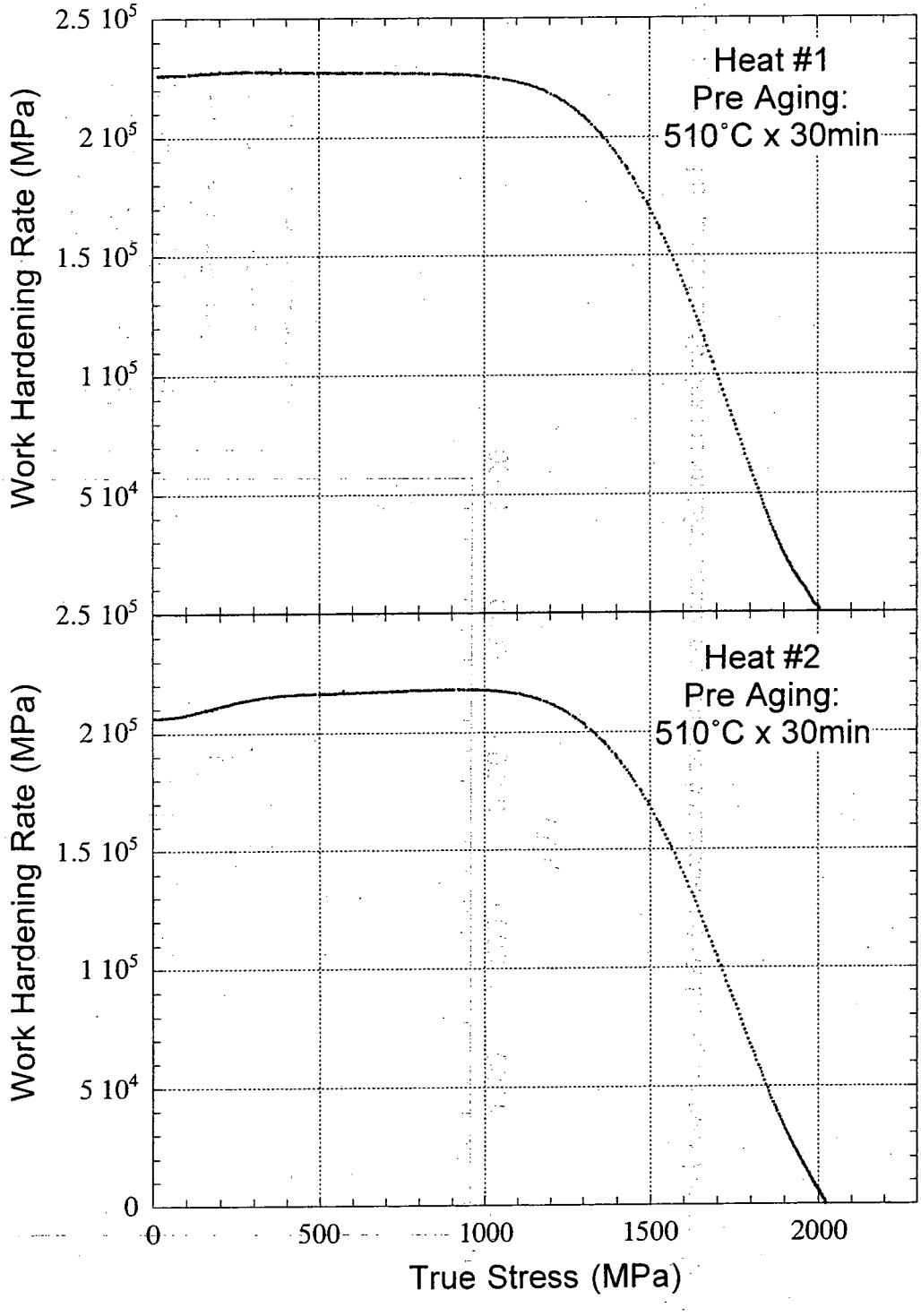

Figure A12 Effect of pre-aging on the work hardening rate – true stress curve.
Heat treatment: (A) 885°C x 1hr, OQ +(DF)-197°C x 1h +
(PreAg) 510°C x 15min, OQ + (DF)-197°C x 1h + (Ag) 482°C x 5h, OQ

Ernest Orlando Lawrence Berkeley National Laboratory
One Cyclotron Road | Berkeley, California 94720

Prepared for the U.S. Department of Energy under Contract No. DE-AC03-76SF00098